AN ADVANCED ION GUIDE FOR BEAM COOLING AND BUNCHING FOR COLLINEAR LASER SPECTROSCOPY OF RARE ISOTOPES

By

Bradley Ryan Barquest

A DISSERTATION

Submitted to
Michigan State University
in partial fulfillment of the requirements
for the degree of

Physics - Doctor of Philosophy

2014

ABSTRACT

AN ADVANCED ION GUIDE FOR BEAM COOLING AND BUNCHING FOR COLLINEAR LASER SPECTROSCOPY OF RARE ISOTOPES

By

Bradley Ryan Barquest

A next generation beam cooler and buncher has been developed and commissioned at NSCL to provide bunched, low energy spread ion beams for collinear laser spectroscopy of rare isotopes. Low energy spread beams reduce the Doppler broadening observed in the fluorescence spectrum, thus improving the resolution achievable in a measurement. Bunched beams permit the reduction of background in fluorescence spectra, thus dramatically improving the signal to noise ratio of the measurement. The beam cooler and buncher features a novel electrode design intended to simplify construction and maintenance, as well as permit the use of large radiofrequency (RF) amplitudes for more efficient beam cooling, especially in the case of high beam currents. A series of ion optical simulations were carried out to determine the design parameters and anticipated bunched beam characteristics. Additional studies using a prototype electrode structure and ion guide system were undertaken to test the performance of the proposed design. The ion guide also serves as a component of the NSCL gas stopping facility. Based on the results of simulation, prototype and ion guide test results, the BECOLA beam cooler and buncher was developed and commissioned. Buncher efficiency, bunched beam energy spread, time width, and transverse emittance were measured using a stable ion source. In addition, the BECOLA collinear laser spectroscopy facility and the beam cooler and buncher were commissioned using a beam of the rare isotope ^{37}K. The results of ion optical simulations, prototype tests, ion guide studies, and BECOLA cooler and buncher characterization measurements are presented and discussed. The results indicate a

successful commissioning of the beam cooler and buncher, along with the rest of the BECOLA facility, with a rare isotope beam, and the systematic studies indicate efficient delivery of low emittance, low energy spread bunched beams well suited for collinear laser spectroscopy.

ACKNOWLEDGMENTS

This PhD project required the involvement of a large cross section of professors, staff scientists, post-docs and support staff. I would like to acknowledge and express my gratitude to them here, not only for their support in finishing the project, but for their role in my education as an experimental physicist.

I would like to thank my dissertation advisor Prof. Georg Bollen for providing me with the opportunity to work on such an interesting project, and for his guidance and insight throughout. I would also like to extend an expression of gratitude to Ryan Ringle and Stefan Schwarz for their invaluable assistance, bringing dedication and technical expertise to bear in realizing the completion of not only the BECOLA beam cooler and buncher, but the gas cell ion guides and prototype tests as well. Ryan, in particular, deserves special recognition as the manager of the BECOLA beam cooler and buncher project, providing extensive guidance and support in overcoming technical and logistical obstacles throughout the duration of the project. It is no exaggeration to say that the completion of the cooler and buncher would not have been possible without their involvement.

I would next like to thank Prof. Dave Morrissey, Chandana Sumithrarachchi, Maxime Brodeur, Alberto Rodriguez, Kortney Cooper, Jeff Kwarsick, and David Skutt for their assistance in the development and commissioning of the ion guide system. Chandana was especially instrumental in the success of the ion guide commissioning studies, and I would be remiss to not thank Max for his assistance with the development of the RF impedance matching circuit.

I would also like to acknowledge the contributions of the BECOLA group, consisting of Prof. Paul Mantica, Kei Minamisono, Dominic Rossi, and Caleb Ryder. Ongoing communication

with Paul and Kei proved very useful during the design and development phase of the project, and the participation of Kei, Dominic, and Caleb was vital to the commissioning of the cooler and buncher using the collinear laser spectroscopy system. I would also like to thank Michael Hammen for his assistance with cooler and buncher assembly, and I would like to thank Paul for his role as a member of my guidance committee.

I'd also like to acknowledge the remaining members of my guidance committee, Prof. Daniela Leitner, Prof. Kirsten Tollefson, and Prof. Morten Hjorth-Jensen, and former committee members Prof. Oliver Kester and Prof. B. Alex Brown.

The list of support staff who helped me along the way is quite long, so I'll briefly mention those to whom I owe a debt of gratitude: Patrick Glennon, Ben Arend, and Jack Ottarson in the NSCL mechanical design department as well as former NSCL engineer Chisom Wilson, the machinists from both the NSCL and PA machine shops, especially Jim Wagner, Jay Pline and Sue LeCureux from NSCL and Tom Palazzolo from PA, RF specialists John Brandon and Dan Morris, electronics group members Jeff Casteel, Patrick Shinaver, Kent Holland, Tom Russo,Ghulam Mujtaba, and Kurt Kranz, electricians Chuck Gaus and Kim Gwinn, the plumber Brad Powell, Andy Thulin and Mike Welton in cryovac, John Priller and Edmund and Charisse Supangco for setting up the control systems, Kyle Elliott and the SRF group, Dan Pendell and Shelly Jones for the cryogen line work, Scott Young, Dave Sanderson and Scott Hitchcock. My sincere apologies to anyone I've left out.

I'd also like to recognize the late Prof. Bob Moore, whose notes and references provided valuable insight for the design of the cooler and buncher.

Finally I must gratefully acknowledge the love and support of friends and family which enabled me to carry on through the often unanticipated difficulties of graduate school. I particularly want to recognize my parents, Cheryl and (Dr.) James Barquest, as well as my

step-parents Linda Slaughter and Jack Robinson, for their support, and for the example set by Dad which was highly instrumental in my choice to pursue a PhD. I love you guys.

Among the many friends and fellow graduate students who've helped to support me, I especially want to thank Dan Coupland and Mike Youngs for having been two of the best officemates a guy could ask for.

I also want to thank Liz and Henry Benatti, for being so supportive of their daughter as well as their future son-in-law.

Last but certainly not least, I want to thank my wonderful fiancee Carla Benatti for being there when I really needed it, and for carrying on right alongside me. I'm incredibly proud of us.

TABLE OF CONTENTS

LIST OF TABLES . . . . . **ix**

LIST OF FIGURES . . . . . **x**

Chapter 1 Introduction **1**
1.1 Collinear Laser Spectroscopy of Rare Isotopes 2
1.2 Gas Stopping 4
1.3 Beam Cooling and Bunching 4
1.4 Beam Production and Delivery to the BEam COoling for LAser Spectroscopy (BECOLA) Facility at NSCL 6
1.5 Dissertation Overview 8

Chapter 2 Physics of Ion Beam Coolers **9**
2.1 Basic Concepts 9
2.2 Radiofrequency Quadrupole Equations of Motion 9
2.2.1 Pseudopotential 10
2.2.2 Mathieu Stability Parameter 12
2.2.3 Longitudinal Confinement 14
2.2.4 Space-Charge Imposed Limits on Ion Storage 15
2.3 Buffer Gas Cooling 16
2.4 Acceptance and Emittance 18

Chapter 3 Advanced Beam Cooler Concept **21**
3.1 Desired Performance Characteristics 21
3.2 High Efficiency - Large Acceptance and Minimized Transport Losses 21
3.3 Low Emittance and Energy Spread 23
3.4 Simplicity of Construction and Maintenance 25

Chapter 4 Simulations for the BECOLA Beam Cooler and Buncher . . . **28**
4.1 Simulated Characteristics of Interest 28
4.2 Acceptance Studies 29
4.3 Simulations of Cooling Region 38
4.4 Bunching and Ejection Simulations 42
4.4.1 Simulated Beam Properties versus Pseudopotential 45
4.4.2 Simulated Beam Properties versus Stability Parameter 48
4.4.3 Simulated Beam Properties versus Slew Time 50
4.4.4 Simulated Beam Properties versus Longitudinal Trap Depth 53
4.4.5 Simulated Beam Properties versus Extraction Field 56
4.4.6 Buncher and Ejection Simulation Results Summary 58
4.5 Differential Pumping Simulations 58

Chapter 5 Development of Electrode Structure and Ion Guide 63
5.1 Discharge Tests 63
5.2 Ion Guide as Cooler and Buncher Prototype: Commissioning Studies 68

Chapter 6 The Beam Cooler and Buncher for Collinear Laser Spectroscopy 76
6.1 BECOLA Overview 76
6.2 Beam Cooler and Buncher Overview 77
6.2.1 Mechanical Systems 81
6.2.2 Electrical Systems 84
6.3 Commissioning Measurements 89
6.3.1 Efficiency Measurements 89
6.3.1.1 Efficiency versus Buffer Gas Pressure 90
6.3.1.2 Efficiency versus Cooling Time and Ion Count 92
6.3.1.3 Efficiency versus Longitudinal Trap Depth 93
6.3.1.4 Efficiency versus Extraction Field 94
6.3.2 Buncher Performance Studies by Collinear Laser Spectroscopy 95
6.3.2.1 Sensitivity Improvement by Beam Bunching 98
6.3.2.2 Measured Time and Energy Widths versus Ion Count per Bunch 98
6.3.2.3 Measured Time and Energy Widths versus Extraction Field 104
6.3.2.4 Measured Time and Energy Widths versus Longitudinal Trap Depth 105
6.3.3 Transverse Emittance Measurements 107
6.3.3.1 Transverse Emittance versus Longitudinal Trap Depth . . . 109
6.3.3.2 Transverse Emittance versus Ion Count per Bunch 110
6.3.3.3 Transverse Emittance versus Cooling Time 111
6.3.3.4 Transverse Emittance versus Buncher Pressure 112
6.3.3.5 Transverse Emittance versus Pseudopotential Depth 113
6.3.3.6 Transverse Emittance versus Stability Parameter 114
6.3.4 Beam Cooler and Buncher Commissioning Measurement Summary . . 117
6.3.5 Online Commissioning Measurement: Hyperfine Spectrum of Rare Isotope ^{37}K 120

Chapter 7 Conclusions 122

APPENDICES 124
Appendix A Radiofrequency Circuit and Bias Channels 125
Appendix B Transverse Emittance Measurements 132
Appendix C Beam Cooler and Buncher Design and Maintenance 135

BIBLIOGRAPHY 142

LIST OF TABLES

Table 4.1 Parameters used for simulation of injection of incident beam into the cooler and buncher, unless otherwise indicated in results figures. All biases are with respect to the high voltage bias. 37

Table 4.2 Parameters used for simulation of ejection of bunched beam, unless otherwise indicated in results figures. All biases are with respect to the high voltage bias. Electrode labels refer to those found in Figure 4.11. 44

Table 5.1 Optimized parameters for ion guide operation based on ion guide characterization studies. 75

Table 6.1 Response of buncher effficiency and extracted beam qualities to increases in buncher parameters. 117

Table 6.2 Optimized parameters for BECOLA beam cooler and buncher operation with a singly charged, mass 39 beam. All biases are with respect to the high voltage bias. Electrode labels refer to those found in Figure 4.11. 118

Table A.1 Electrode, cable number, and control system channel names. The two values for DG refer to the trapping and ejecting voltages. The physical locations inside the cooler and buncher are given in Figure A.3. All control channel names are preceded by DBEC_BCB. 131

LIST OF FIGURES

Figure 1.1 Chart of the nuclides illustrating which isotopes have been studied via collinear laser spectroscopy [9]. Black squares indicate stable nuclei; gray squares represent known unstable nuclides. Nuclei which have been studied in collinear laser spectroscopy experiments have been colored in red. 2

Figure 1.2 Layout of the Coupled Cyclotron Facility at NSCL. 6

Figure 2.1 Sketch of linear radiofrequency quadrupole (RFQ) structure. 10

Figure 2.2 SIMION [26] simulation of an ion trajectory inside a radiofrequency quadrupole. x represents the transverse motion coordinate, while z refers to the coordinate along the beam axis. 10

Figure 2.3 An oscillating or rotating saddle-point potential, such as that produced by a radiofrequency quadrupole. 10

Figure 2.4 An illustration of a set of segmented RFQ rods. 14

Figure 2.5 Simulation of ion trajectory in an RFQ in the presence of buffer gas. As in Figure 2.2, x is the transverse coordinate, z is the longitudinal coordinate. 16

Figure 3.1 Illustration of injection electrodes for the BECOLA beam cooler and buncher. 22

Figure 3.2 A comparison between using fine segmentation and using a diagonal crosscut to create a drag potential in a beam cooler. 26

Figure 3.3 An illustration of the RF backbone coupling scheme. 26

Figure 3.4 Top: A schematic of the overall structure of the BECOLA beam cooler and buncher. Bottom: A sketch of the static potential with a sample ion trajectory in grey. The dashed line on the right side of the potential indicates the potential when the ion bunch is released. . . 27

Figure 4.1 Sketch of emittance or acceptance ellipses at different RF phases. The SHM (simple harmonic motion) curve refers to the motion in the pseudopotential for all RF phases. The shaded grey area illustrates the RF independent region for the given phases. Adapted from [38, 39]. 30

Figure 4.2 Example of a simulated acceptance. Points are individual ion phase space coordinates, while the curve represents the calculated phase space ellipse. This particular example gives an acceptance $4\epsilon_{RMS}$ of about 100 π mm mrad. 32

Figure 4.3 Plot of simulated acceptances as a function of injection energy and opening angle of the 1st tapered segment of RFQ electrode for 7 cm length. 33

Figure 4.4 Plot of simulated acceptances as a function of injection energy and opening angle of the 1st tapered segment of RFQ electrode for 15 cm length. 34

Figure 4.5 Simulated acceptance as a function of the stability parameter q chosen such that the pseudopotential at the electrode surface is 75 V using a mass 20 beam. Both 95% and RF independent acceptances are plotted. 35

Figure 4.6 Simulated acceptance as a function of the pseudopotential depth chosen such that the stability parameter q is 0.3 using a mass 20 beam. Both 95% and RF independent acceptances are plotted. 36

Figure 4.7 Simulated RF independent acceptance as a function of the ion mass. 36

Figure 4.8 Characteristic simulated stopping distance versus buffer gas pressure for a mass 250 u beam. Stopping distances are the result of exponential fits of average ion energy versus distance in the presence of buffer gas. 38

Figure 4.9 Sketch of crosscut geometry looking along the beam axis. 40

Figure 4.10 On-axis drag potentials for different crosscut distances (see Figure 4.9). Curves are labeled by how far away from the central axis the crosscut sits at the edge of the electrode. r_0 refers to the distance from the electrode tip to the central beam axis. 41

Figure 4.11 Sketch of the buncher and extraction portion of the BECOLA beam cooler and buncher. 43

Figure 4.12 Plot of simulated extracted transverse emittance versus pseudopotential depth $V_{pseudo}(r_0)$ (see Equation 2.1). A fit of the data to a function of the from $f(V) = a + \frac{b}{\sqrt{V}}$ is shown in red. 45

Figure 4.13 Plot of the simulated full width at half-maximum (FWHM) of the extracted time of flight spectra as a function of pseudopotential depth. 46

Figure 4.14 Plot of simulated energy spread of extracted ion pulses versus pseudopotential depth. 47

Figure 4.15 Plot of simulated extracted transverse emittance versus stability parameter q (see Equation 2.7). RF voltage and frequency were varied in such a way as to keep the pseudopotential (see Equation 2.1) constant. 48

Figure 4.16 Plot of the simulated time spread of extracted pulses as a function of stability parameter. 49

Figure 4.17 Plot of the simulated energy spread of extracted pulses as a function of stability parameter. 49

Figure 4.18 Plot of simulated extracted transverse emittance versus extraction voltage slew time. 50

Figure 4.19 Plot of the simulated time spread of extracted pulses as a function of slew time. 51

Figure 4.20 Plot of the simulated time spread of extracted pulses as a function of slew time. 52

Figure 4.21 Plot of simulated extracted transverse emittance versus longitudinal trap depth. 53

Figure 4.22 Plot of simulated extracted time width versus longitudinal trap depth. 54

Figure 4.23 Plot of simulated extracted energy spread versus longitudinal trap depth. 55

Figure 4.24 Plot of simulated extracted transverse emittance versus extraction field at the trap center. 56

Figure 4.25 Plot of simulated extracted time width versus extraction field at the trap center. 57

Figure 4.26 Plot of simulated extracted energy spread versus extraction field at the trap center. 57

Figure 4.27 Sketch of differential pumping channel cross section. 59

Figure 4.28 Simulated conductance of differential pumping channel as a function of radius of open region (black central region of Figure 4.27), compared to the calculated value for a cylindrical tube. A channel length of 10 cm was used in simulation. 60

Figure 4.29 Illustration of a portion of the vacuum system involved in calculating the differential pumping channel conductance. A helium inlet feeds gas into the high pressure cooling region, while gas flow out of the cooler is restricted by the differential pumping channel. The buncher region of the vacuum chamber is pumped directly by a turbomolecular pump. 61

Figure 5.1 Design image of prototype electrode structure for RF discharge tests. 64

Figure 5.2 Closeup design image of prototype crosscut electrode geometry for cooler drag field. 65

Figure 5.3 RF discharge voltages as a function of buffer gas pressure. RF was operated at 5.7 MHz. 66

Figure 5.4 Static discharge voltage as a function of buffer gas pressure. Bias was applied to one segment of the drag field electrode as depicted in Figure 5.2, while the complement, the other segments and the backbone were held at ground. 66

Figure 5.5 Left (a): Prototype electrode structure inside vacuum chamber, bottom view. RF leads protrude from the side of the electrodes. Middle (b): Image of RF induced discharge in a helium buffer gas pressure of about 2 Torr. Right (c): Glow discharge at a pressure of about 55 mTorr. 67

Figure 5.6 Top: Sketch of the ion guide system. Bottom: Sketch of Static potential. 68

Figure 5.7 Image of the ion guide system. 69

Figure 5.8 Ion guide transmission as a function of RF amplitude. Error bars are smaller than displayed points. 70

Figure 5.9 Plot of transport efficiency as a function of ion guide drag field in the high pressure region. Error bars are smaller than the displayed points. 71

Figure 5.10 Transmission efficiency as a function of retardation voltage for different buffer gas pressures. Error bars are smaller than the displayed points. 72

Figure 5.11 Plot of the ion beam energy spread for different buffer gas pressures. 73

Figure 5.12 Transmission efficiency as a function of retardation voltage for different incident beam currents. Error bars are smaller than the displayed points. Pressure in the upstream portion of the ion guide was 24 mTorr. 74

Figure 5.13 Plot of the beam energy spread for different incident currents. . . . 74

Figure 6.1 Layout of the BECOLA facility [16]. 76

Figure 6.2 Photograph of assembled beam cooler and buncher. Beam enters from the right. 78

Figure 6.3 Lateral cross-section view of BECOLA beam cooler and buncher design. The cutaway view shows the RFQ electrodes (teal) extending the length of the interior, with stacks of Macor discs forming the differential pumping channels. 79

Figure 6.4 Design image of BECOLA beam cooler and buncher. The vacuum chamber interior view shows the exterior of differential pumping channel and cooling region. 80

Figure 6.5 Design image of injection optics. The ejection side is similar, though it lacks the buffer gas (He) inlet. 82

Figure 6.6 Left (a): Design image of injection stage of BECOLA beam cooler and buncher. Right (b): Photograph of beam cooler injection stage, including cooler, 1st differential pumping channel, and cryogenic cooling loop. 83

Figure 6.7 Photograph of beam cooler injection electrodes. The injection cone electrode sits immediately upstream of the flared RFQ rods, and the RF conductors can be seen connecting opposite backbone electrodes together. 83

Figure 6.8 Photograph of partially assembled drag field electrode and RF backbone substructure. 85

Figure 6.9 Photograph of buncher electrodes, with pen for scale. 86

Figure 6.10 Photograph of buncher electrodes 86

Figure 6.11 Photograph of RFQ electrode cross section. A Macor disc frames the exterior, and the hole in the center of the extraction cone can be seen through the center of the RFQ in green. 87

Figure 6.12 Design image of the vacuum-air interface for the RF and bias voltage circuitry. 87

Figure 6.13 Sketch of the circuit which supplies RF and static voltages to RFQ electrodes. Red and blue indicate opposite RF phases, and static voltage connections are depicted in green. The transmission line transformer (TLT) matches the output impedance of the RF amplifier to the resonant load impedance. 88

Figure 6.14 Measured bunched mode efficiency as a function of buffer gas pressure in the cooler. 91

Figure 6.15 Bunched mode efficiency versus cooling time for different numbers of ions per bunch. 92

Figure 6.16 Efficiency versus incident ions per bunch. A confinement time of 10 ms was used. 93

Figure 6.17 Bunched mode efficiency as a function of static voltage trap depth. . 94

Figure 6.18 Results of efficiency measurements as a function of the extraction field at the potential minimum. 95

Figure 6.19 Level scheme of hyperfine levels for the D1 transition of ^{39}K [45]. Energy differences are not to scale. 96

Figure 6.20 Hyperfine spectrum of D1 transition of ^{39}K for two different RF settings. Left (a): Spectrum was taken using 5.3 MHz frequency and 900 V_{pp} amplitude. Right (b): Spectrum was taken using 1.2 MHz RF frequency and 110 V_{pp} amplitude. 97

Figure 6.21 A comparison of bunched and unbunched fluorescence spectra. . . . 99

Figure 6.22 Simulated time of flight spectrum. Results were obtained using a particle in cell (PIC) code, simulating 10^5 ions ejected from the buncher. 100

Figure 6.23 Particle in cell simulation of 10^6 bunched and ejected from the beam cooler and buncher. 101

Figure 6.24 Measured time of flight spectrum of a bunched beam with 10^5 ions per bunch. 101

Figure 6.25 Measured time of flight spectrum of a bunched beam with 10^6 ions per bunch. 102

Figure 6.26 Measured time widths of bunched beams versus ion count per bunch. 102

Figure 6.27 Measured energy widths of bunched beams versus ion count per bunch. 103

Figure 6.28 Measured time of flight spectra of bunched beams as a function of extraction field. As with the efficiency measurements, the extraction fields were calculated using experimental voltage inputs with a SIMION model. 104

Figure 6.29 Measured energy spread versus extraction field, compared to PIC and SIMION simulation results. 105

Figure 6.30 Measured time widths as a function of longitudinal trap depth. . . . 106

Figure 6.31 Measured energy widths as a function of longitudinal trap depth. . . 106

Figure 6.32 Example of a beam spot on MCP phosphor screen. 108

Figure 6.33 Example of beam profile projected onto one axis with a Gaussian fit. 109

Figure 6.34 Example of beam profile widths (squared) plotted versus lens voltage with parabolic fit. 110

Figure 6.35 Measured transverse emittances versus static trap potential depth. . 111

Figure 6.36 Measurement of extracted transverse emittance as a function of incident ions per bunch. 112

Figure 6.37 Measurement of extracted transverse emittance as a function of incident ions per bunch. 113

Figure 6.38 Measured transverse emittances as a function of cooling time in the buncher. 114

Figure 6.39 Transverse emittance measurements versus buncher pressure. The cooler pressure is about a factor of 100 higher than that in the buncher due to the differential pumping scheme. 115

Figure 6.40 Measurements and PIC simulation of transverse emittances versus RF pseudopotential, and fit to $f(V) = a + \frac{b}{\sqrt{V}}$. stability parameter q was held at 0.38. 115

Figure 6.41 Measured transverse emittances versus stability parameter. The pseudopotential was kept constant. 116

Figure 6.42 Left (a): Hyperfine spectrum of D1 transition of ^{37}K and Voigt fit. Right (b): Hyperfine spectrum of D1 transition of ^{39}K and Voigt fit. Due to hyperfine isotope shift, the f_0 values in the two plots are not the same. 120

Figure A.1 Sketch of RF and bias voltage circuit, with switch and low pass filter. Only one bias channel is shown in this example. Typical resistance and capacitance values are listed. Thick lines indicate RF circuit components; thin lines represent static voltage circuitry. At points of intersection, bias leads are threaded through the center of hollow RF conductor, e.g. through the inductors. 126

Figure A.2 Left (a): Photo of the upstream RF circuit. Right (b): Photograph of the downstream RF circuit. 127

Figure A.3 Sketch of electrode layout, with each electrode labeled. Beam travels left to right. 129

Figure A.4 Left (a): Photograph of flange/plug interface (see also Figure 6.12). Right (b): Diagram of the pin assignment as viewed from the face of the plug. 130

Figure C.1 Exploded design view of BECOLA beam cooler and buncher. For ease of machining and assembly, the RFQ structure is split into upstream and downstream subassemblies, each of which are mounted to flanges at either end of the vacuum chamber. 136

Figure C.2 13.25" flange mounted to maintenance cart. RFQ electrodes are mounted to the far side. 139

Figure C.3 Sketch of the shim under the rotating flange on the vacuum chamber. 140

Chapter 1

Introduction

The study of rare isotopes has important implications for understanding the details of nuclear structure [1], nuclear astrophysics [2], and fundamental symmetries [3]. As rare isotopes are short-lived and only produced in nature in extreme astrophysical environments, it is necessary to devise techniques to produce and study rare isotopes in a laboratory environment, and to maximize the sensitivity of such studies, if the characteristics of the rarest species are to be understood.

Ion manipulation and trapping with radiofrequency electric fields and buffer gas is a widely used technique to tailor the properties of ion beams for a variety of experiments [4, 5, 6], and enjoys extensive use in precision low energy nuclear physics studies [7, 8]. The use of such techniques is particularly important for precision experiments involving rare isotope beams, where highly efficient beam transport and detection are necessary. This dissertation details the development and commissioning of an ion beam cooler and buncher intended to enhance the sensitivity of collinear laser spectroscopy measurements at the National Superconducting Cyclotron Laboratory (NSCL) at Michigan State University while improving on the designs of previous such devices.

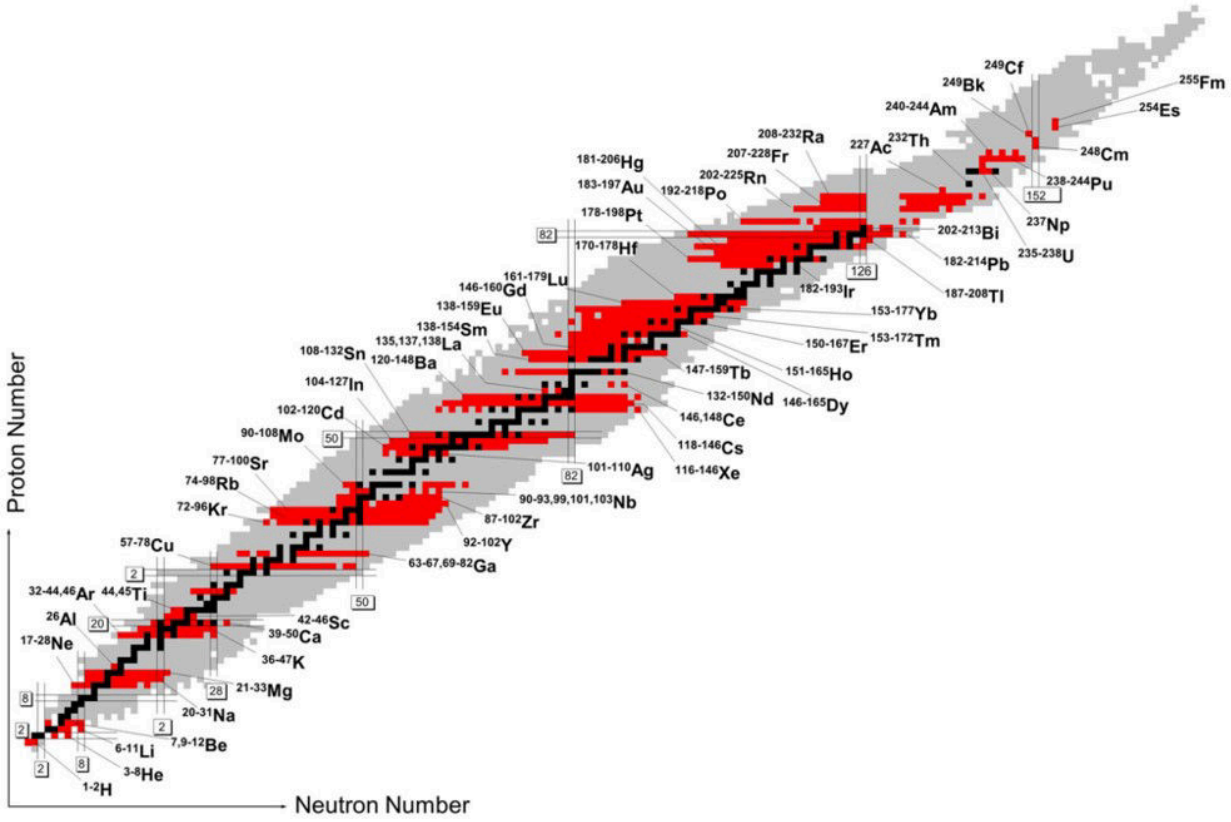

Figure 1.1: Chart of the nuclides illustrating which isotopes have been studied via collinear laser spectroscopy [9]. Black squares indicate stable nuclei; gray squares represent known unstable nuclides. Nuclei which have been studied in collinear laser spectroscopy experiments have been colored in red.

1.1 Collinear Laser Spectroscopy of Rare Isotopes

Collinear laser spectroscopy provides a model independent means of investigating nuclear spin, magnetic dipole and electric quadrupole moments, as well as shifts in mean square charge radius through study of the hyperfine coupling of electronic angular momentum to ground state or long lived isomeric nuclear wavefunctions [10]. Such studies can lend insights into how ground state nuclear moments and charge radii evolve across isotopic chains through direct measurement without recourse to a particular model to infer the quantities of interest. Collinear laser spectroscopic measurements of nuclear moments and mean square charge radius shifts can therefore be compared against theoretical predictions of nuclear size (mean

square charge radius) and shape (multipole moments) trends.

Collinear laser spectroscopy requires beam energies of order a few tens of keV, with spread in beam energy equal to or better than a few eV. The majority of collinear laser spectroscopy measurements of rare isotopes performed to date were carried out at Isotope Separation On-Line (ISOL) type facilities [11], where intense beams of unstable nuclei are readily available at low energies and energy spreads suitable for collinear laser spectroscopy measurements. At an ISOL facility, light beams, such as protons or ^{3}He, are impinged on a production target thick enough to stop the beam, where products from beam-target reactions are produced essentially at rest. The reaction products diffuse out of the target, are post-ionized and can then be formed into a beam for physics experiments. Beams of elements with rapid diffusion times, such as alkali metals and noble gases, are particularly well suited for production at ISOL type facilities, and have been used extensively in ISOL based experiments, including collinear laser spectroscopy efforts.

Figure 1.1 shows the nuclides that have been studied via collinear laser spectroscopy. The pattern of certain groups of elements having been studied extensively while others have yet to be probed in this way becomes immediately clear. In order to expand the reach of collinear laser spectroscopy experiments, it is beneficial to take advantage of beam production techniques whose capabilities complement those of ISOL. Projectile fragmentation uses a heavy beam impinged on a light production target thin enough that the reaction products escape the target still traveling at high velocity ($\sim$100 MeV/u), while all isotopes but the one of interest are filtered out in flight. Production rates are therefore independent of diffusion times out of a target. However, while beams produced in this manner are well suited to higher energy experiments, and while laser spectroscopy measurements have been performed in flight [12], the adaptation of such a fast beam to low energy precision experiments, such

as collinear laser spectroscopy, poses a host of technical challenges. In particular, the beam must be decelerated by several orders of magnitude quickly and efficiently.

1.2 Gas Stopping

Advances in gas stopping techniques [8, 13, 14] allow projectile fragmentation beam energies to be reduced to the energies required for low energy precision experiments [15, 16]. Simply decelerating the beam electrostatically is infeasible for two reasons. First, the voltages necessary are impractically large, and second, since the transverse emittance scales reciprocally with beam momentum, the ability to efficiently transport such a decelerated beam becomes challenging without some cooling mechanism. These obstacles can be overcome by slowing the beam through solid matter and bringing the beam to rest in a gaseous (usually helium) environment. The ions can then be manipulated by a combination of static and RF fields [8, 17], to guide ions way from internal gas cell surfaces and out of the vessel towards the experiment. Efficient ion beam capture can be accomplished if the gas cell is long enough to span the range of incident ions [18], and collisions with the gas atoms also serve to reduce both transverse and longitudinal energy spread, thus avoiding the ion optical difficulties from simple electrostatic deceleration. For some experiments, additional beam manipulation, such as bunching, may be necessary to attain the desired sensitivity for the measurement.

1.3 Beam Cooling and Bunching

Although projectile fragmentation yields are higher than those of ISOL for certain isotopes, it is still necessary to maximize the sensitivity of the collinear laser spectroscopy apparatus to measure the isotopes furthest from stability. Collinear laser spectroscopy sensitivity can

be enhanced by the use of a beam cooler and buncher in two significant ways. Buffer gas cooling [19] can be used in the presence of confining radiofrequency and static electric fields to reduce the energy spread of the ion beam and hence decrease the Doppler broadening of the fluorescence spectrum. Moreover, photon backgrounds, especially those from scattered laser light, decrease the signal to noise ratio of a collinear laser spectroscopy measurement. Reduction of such background is critical for low count rate experiments, as experiments using rare isotopes tend to be. One important technique for reducing photon background is to use a pulsed or bunched beam, and coincide fluorescence measurements with the arrival of the pulse of ions or neutralized atoms through the photon counting region. By efficiently accumulating the ions into a pulse with a short width, and by timing the pulses to arrive over periods much longer than the pulse width, it becomes possible to reduce the photon background due to stray light by that same duty cycle factor while preserving the signal, thus dramatically enhancing the sensitivity of a collinear laser spectroscopy measurement.

While beam cooling and bunching was already a known technique adapted to Penning trap mass spectrometry [20], the Jyväskylä group was the first to demonstrate its use with collinear laser spectroscopy [21]. Since low count rates are an inevitable obstacle to the measurement of the most exotic nuclides, regardless of production mechanism, beam cooler and bunchers have become a standard tool in collinear laser spectroscopy of rare isotopes. Beam cooler and bunchers have been installed at other facilities where collinear laser spectroscopy experiments are performed, including ISOLDE [22], Mainz [23], TRIUMF [24], and now, NSCL. While gains observed in energy spread and background suppression due to cooling and bunching have been substantial, the highest gains will be realized for systems capable of fast, efficient cooling and bunching. The design of a next generation beam cooler and buncher must consider injection efficiency, seek to avoid in-trap losses, minimize cooling times to reduce

decay losses, and eject ion bunches efficiently without increasing energy spread.

1.4 Beam Production and Delivery to the BEam COoling for LAser Spectroscopy (BECOLA) Facility at NSCL

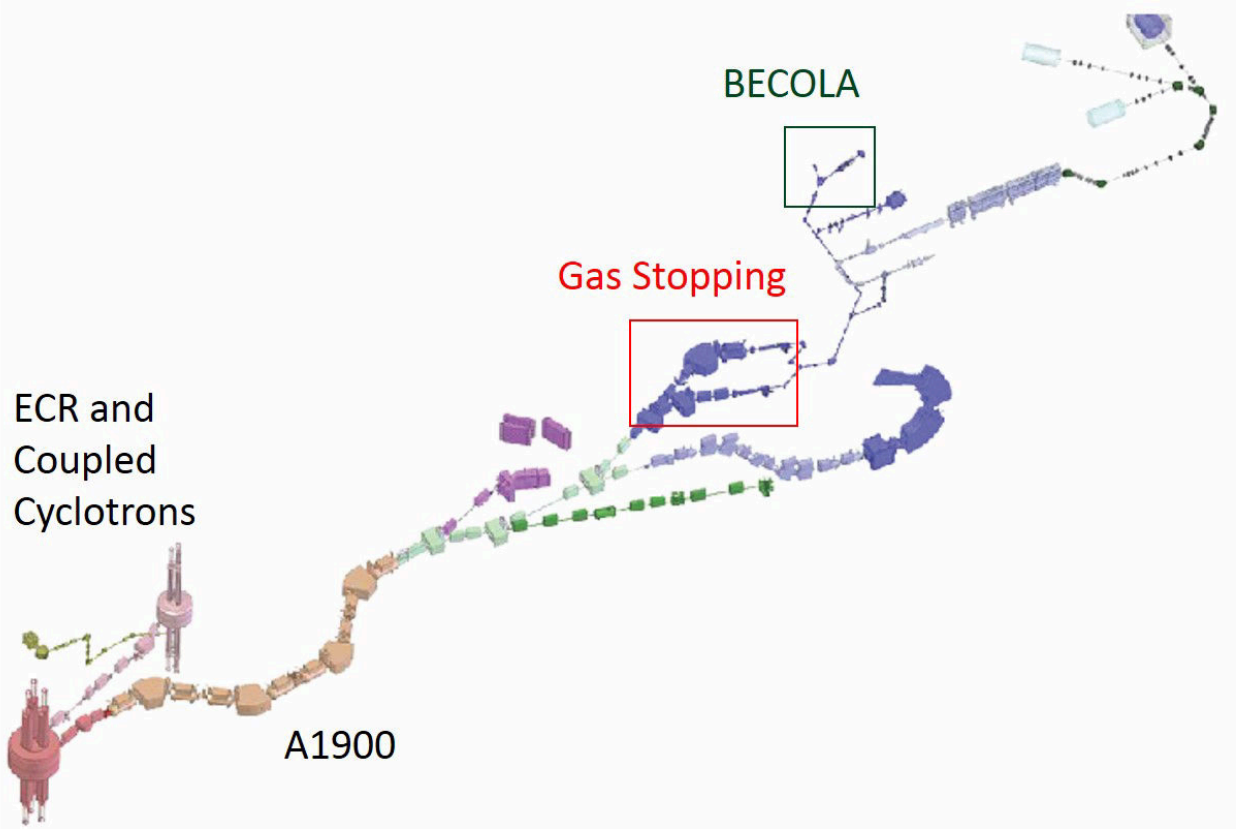

Figure 1.2: Layout of the Coupled Cyclotron Facility at NSCL.

The development of the BEam COoling for LAser spectroscopy (BECOLA) facility at NSCL (see Figure 1.2) represents a new installation of a collinear laser spectroscopy experimental station at a projectile fragmentation facility, thus extending the range of isotopes available for study. As part of the commissioning of the BECOLA facility, including

the beam cooler and buncher, an online experiment was performed using neutron deficient potassium isotopes produced by the NSCL Coupled Cyclotron Facility (CCF) [25]. The CCF consists of an electron-cyclotron resonance (ECR) ion source, the K500 cyclotron, the coupling line, the K1200 cyclotron, the A1900 fragment separator, and several experimental stations. Stable, highly charged beams from the ECR ion source are accelerated in the coupled cyclotrons to a final energy of 100-150 MeV/u. The primary beam is then impinged on a beryllium production target. The projectile fragments are then filtered through the A1900 fragment separator to obtain a beam of the isotope of interest. For precision low energy experiments, the beam is sent through the gas stopping station (red box in Figure 1.2). The beam passes through a solid energy degrader and finally brought to rest inside a helium filled vessel. The ions are transported by a combination of RF and static electric fields to a nozzle, where gas flow transports the ions out of the gas cell. To convey the ions from the high pressure ($\sim$100 mbar) gas cell environment to the low pressure (about 10^{-7} mbar) beamline environment, a radiofrequency quadrupole based ion guide is employed with differential pumping to reduce the pressure of the system in stages. At the exit of the ion guide the beam is then reaccelerated electrostatically to 30 keV for transport to the BECOLA cooler and buncher. The beam cooler and buncher resides upstream of the collinear laser spectroscopy beamline, all of which comprise the BECOLA facility (Figure 1.2, green box) The incident beam is cooled and bunched, and sent to the collinear laser beamline where the fluorescence spectra are measured.

1.5 Dissertation Overview

This dissertation accounts for the design, development, construction and commissioning of a next generation ion beam cooler and buncher for use with the BECOLA collinear laser spectroscopy beamline installed at NSCL, as well as a new ion guide system coupled with a next generation gas stopping system. Chapter 2 discusses the basics of what an ion beam cooler is, the essential features of a beam cooler, and the physics of how ions behave in a beam cooler. Chapter 3 lays out a new concept for how a cooler and buncher might be built which simplifies designs used in previous devices. Chapter 4 discusses the simulation work undertaken to inform in more detail the particular design parameters such a cooler and buncher should have and how such a device should be expected to perform. Chapter 5 describes the developmental work done to test the design concepts on a prototype electrode assembly as well as an ion guide implemented as part of the NSCL gas stopping facility. Chapter 6 presents the final design and characterization results of the BECOLA beam cooler and buncher. Chapter 7 concludes the discussion of the advanced ion guide concept.

Chapter 2

Physics of Ion Beam Coolers

2.1 Basic Concepts

An ion beam cooler is a type of ion guide intended to reduce the transverse phase space volume, or emittance, and energy spread of an ion beam. The majority of ion guides or beam coolers rely on the use of a linear radiofrequency quadrupole field (RFQ, see Figure 2.1) for transverse confinement. Four rods are placed such that, viewed from the cross-section, the centers of the rods form the vertices of a square. An oscillating potential is applied such that adjacent rods are of opposite polarity, yielding an oscillating quadrupole potential. An ion beam traveling through the center of the quadrupole will, for certain potential amplitudes and frequencies, experience a time averaged radially confining force. Additional static (DC) fields can be applied in a segmented system for complete 3-dimensional ion confinement. Beam cooling is accomplished by a damping force introduced through collisions with a buffer gas which, on average, tends to damp ion motion towards the potential minimum created by the superposition of RF and static fields.

2.2 Radiofrequency Quadrupole Equations of Motion

The motion of an ion in an RFQ can be characterized by two independent sinusoidal oscillations (see Figure 2.2). The ion undergoes oscillatory micromotion at the driving frequency, as well

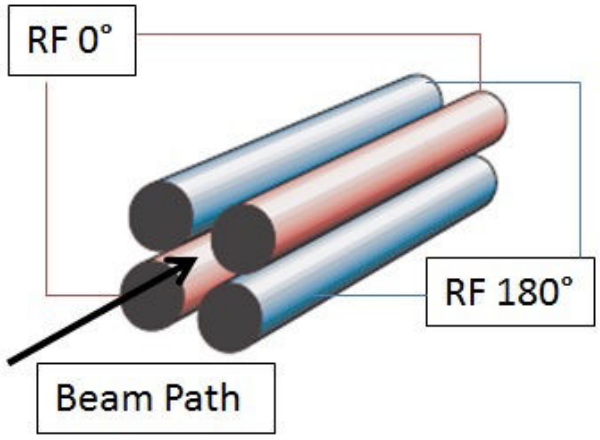

Figure 2.1: Sketch of linear radiofrequency quadrupole (RFQ) structure.

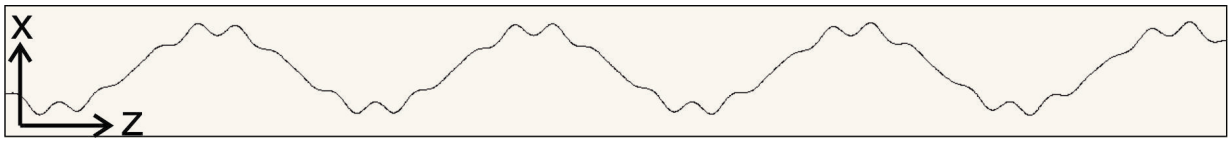

Figure 2.2: SIMION [26] simulation of an ion trajectory inside a radiofrequency quadrupole. x represents the transverse motion coordinate, while z refers to the coordinate along the beam axis.

as a slower macromotion arising from confinement in a so-called pseudopotential produced by the oscillating quadrupole fields.

2.2.1 Pseudopotential

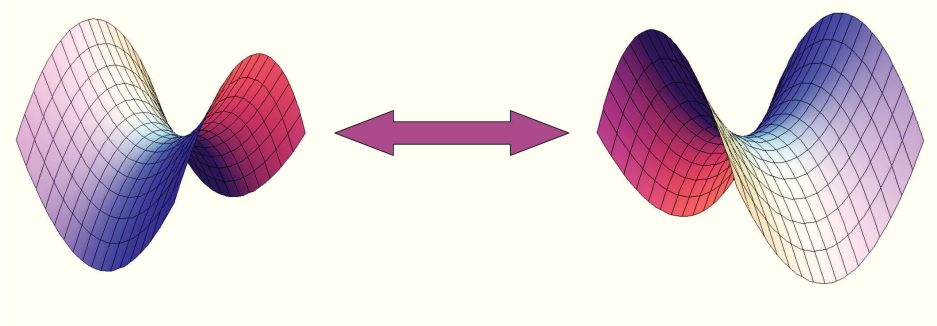

Figure 2.3: An oscillating or rotating saddle-point potential, such as that produced by a radiofrequency quadrupole.

According to Earnshaw's theorem [27], full 3-dimensional confinement of a collection of

charges cannot be realized through static electric fields alone. Further, the lowest order multipole which allows a potential minimum is the quadrupole. Even so, such a potential yields a saddle point, that is, ion motion will be stable in one direction but unstable in a transverse direction. This instability can be circumvented by the use of time-varying, inhomogeneous fields. Conceptually, one can imagine that this is equivalent to oscillating or rotating the saddle point (see Figure 2.3) such that the ion, rolling down the hill in the unstable direction, experiences a restoring force back towards the saddle point after a time equal to half the RF period. Dehmelt showed [19] that an inhomogeneous RF field can create a nonzero time averaged force on a test charge, which can be expressed in terms of the gradient of a pseudopotential. Since such devices typically use fields that oscillate with frequencies in the MHz region for heavy ions, they are often referred to as radiofrequency quadrupoles, or RFQs. In the case of a linear quadrupole geometry, the pseudopotential takes the form [28]

$$V_{pseudo}(r) = \frac{eV_{RF}^2}{4mr_0^4\omega_{RF}^2}r^2 \tag{2.1}$$

in the plane transverse to the axis of symmetry, where r_0 is the distance from the central axis to the RFQ electrode, m is ion mass, e is the ion charge, ω_{RF} is the RF angular frequency and V_{RF} is the peak to peak RF amplitude. Hence a radiofrequency electric field applied in a linear quadrupole geometry creates a harmonic oscillator potential. For the rest of this dissertation, the term pseudopotential depth shall be used to mean Equation 2.1 evaluated at $r = r_0$. In an ideal quadrupole geometry, the electrode surfaces themselves form hyperbola in the transverse plane, and are described by

$$y^2 - x^2 = \pm r_0^2 \tag{2.2}$$

Confinement along the axis of symmetry can be realized by either segmenting the rods and applying static voltage offsets to the individual segments, or by adding external electrodes and applying trapping potentials.

2.2.2 Mathieu Stability Parameter

It is not sufficient to apply arbitrary RF parameters and expect to achieve ion confinement, however. To draw upon the oscillating saddle point potential picture again, one can conceive that, in the limit of large RF amplitudes but low frequencies, the ion is driven strongly away from the saddle point before the potential has time to switch to the opposite polarity and keep the ion confined. In order to understand under what conditions ion motion is stable it is necessary to look to the equations of motion [5]. In a linear quadrupole geometry, the solution to the Laplace equation takes the form

$$\Phi = \frac{\Phi_0}{2r_0^2}(y^2 - x^2) \tag{2.3}$$

where Φ_0 is the potential applied across adjacent electrodes. This looks like a stable harmonic oscillator in one coordinate and an unstable harmonic oscillator in the other, depending on the sign of Φ_0. Thus we can write down the usual 2nd order differential equations to describe simple harmonic motion:

$$\frac{d^2x}{dt^2} - \omega^2 x = 0 \tag{2.4}$$

$$\frac{d^2y}{dt^2} + \omega^2 y = 0 \tag{2.5}$$

where $\omega^2 = \frac{e\Phi_0}{mr_0^2}$. Since the discussion pertains to a radiofrequency device, the potential Φ_0 will oscillate in time, according to

$$\Phi_0 = V_{RF} \cos \omega_{RF} t \tag{2.6}$$

The fact that the potential oscillates in time prevents the existence of a closed-form solution. However, with some additional substitutions, it is possible to cast the above differential equations in the form of the canonical Mathieu equations and analyze the behavior of ions in terms of a so-called Mathieu stability parameter q. One can define the parameters

$$q = \frac{2eV_{RF}}{mr_0^2\omega_{RF}^2} \tag{2.7}$$

$$\tau = \frac{\omega_{RF} t}{2} \tag{2.8}$$

and can rewrite the equations of motion as follows

$$\frac{d^2\xi}{d\tau^2} + 2q\cos(2\tau)\xi = 0 \tag{2.9}$$

where ξ represents either the x or y coordinate. τ is the RF phase divided by 2, and q is a dimensionless parameter which represents the permissible combination of RF amplitude, frequency, trap dimension, ion charge and mass for stable trajectories. The criterion for stable ion motion is $q < 0.908$ [28]. It is possible to express the motion of the ions as a product of a rapid oscillation due to the direct drive of the RF itself, coupled with a slower macrooscillation in the pseudopotential well (see top portion of Figure 2.2). If we define a

macrooscillation frequency ω_{mac} such that $V_{pseudo}(r) = \frac{m\omega_{mac}^2 r^2}{2}$ and refer to Equations 2.1 and 2.7 for the pseudopotential and stability parameter, one can show

$$\omega_{mac}^2 = \frac{q^2\omega_{RF}^2}{8} \tag{2.10}$$

or

$$\omega_{mac}^2 = \frac{2e}{mr_0^2} V_{pseudo}(r_0) \tag{2.11}$$

2.2.3 Longitudinal Confinement

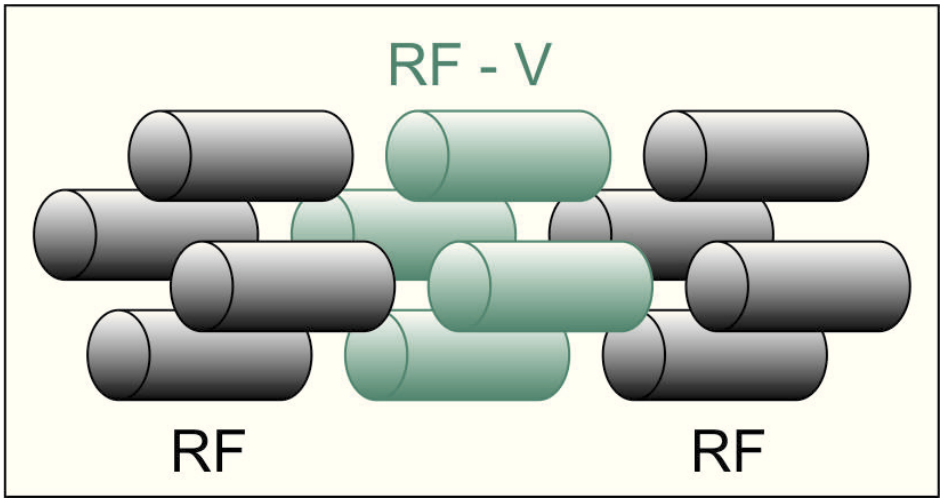

Figure 2.4: An illustration of a set of segmented RFQ rods.

Static electric fields are employed to move ions through buffer gas or to form a longitudinal trap. In the case of the formation of a trap, a simple example would consist of three sets of adjacent electrodes, each set with the same quadrupole RF setup, but with different static offsets (see Figure 2.4). If the outer two sets of electrodes hold no offset, and the middle experience an offset $-V_{static}$, a symmetric trap is formed. From the Laplace equation, the static potential in such a case takes the form

$$V(r,z)_{static} = \frac{V_{static}}{z_0^2}\left(z^2 - \frac{r^2}{2}\right) \tag{2.12}$$

where z_0 is a characteristic distance determined by system geometry. The result is that, although confinement along the beam axis is achieved, the static potential destabilizes motion in the transverse plane. The pseudopotential from the RF must therefore be deep enough to counteract this effect.

2.2.4 Space-Charge Imposed Limits on Ion Storage

The number of ions able to be held in an ion trap is limited by Coulomb repulsion among ions in the cloud, also known as the space charge effect. A simple argument presented by Dehmelt [19] can be used to estimate the maximum charge density attainable in the trap. In this picture, the space charge limit is reached when the potential due to space charge cancels that of the confining fields. From the Poisson equation $\nabla^2\phi = \frac{\rho}{\epsilon_0}$, the maximum charge density can be calculated from the Laplacian of the static potential and pseudopotential. From Equations 2.1 and 2.12, we have

$$\phi = V_{pseudo} + V_{static} = \frac{eV_{RF}^2}{4mr_0^4\omega_{RF}^2}r^2 + \frac{V_{static}}{z_0^2}\left(z^2 - \frac{r^2}{2}\right) \tag{2.13}$$

Taking the Laplacian, we have

$$\nabla^2\phi = \frac{eV_{RF}^2}{mr_0^4\omega_{RF}^2} = \frac{\rho}{\epsilon_0} \tag{2.14}$$

To provide an example, for a mass 39 beam of singly charged ions, using an RFQ geometry with a characteristic r_0 of 3.5 mm, an RF frequency $f = \frac{\omega_{RF}}{2\pi}$ of 1.2 MHz, and 100 V RF

peak to peak amplitude, a maximum density of about 1.5×10^5 ions per mm^3 is predicted to be possible. If the ion cloud is presumed to extend laterally to the electrode surface, and if the longitudinal trap is formed by a segment 5 mm long, a maximum ion number of about 3×10^7 ions is estimated. In order to trap more ions, a larger trap volume or stronger pseudopotential is required.

2.3 Buffer Gas Cooling

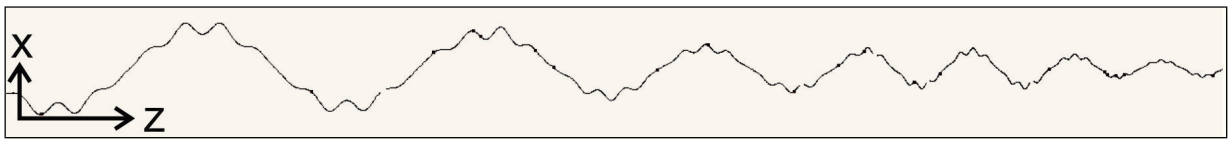

Figure 2.5: Simulation of ion trajectory in an RFQ in the presence of buffer gas. As in Figure 2.2, x is the transverse coordinate, z is the longitudinal coordinate.

Liouville's theorem asserts that when only conservative forces act on a collection of particles the phase space volume, or emittance, of that ensemble is conserved. Therefore, in order to shrink the phase space volume of an ion pulse, it is necessary to introduce a non-conservative force to the system. The presence of buffer gas in the ion trap volume adds a damping force, which is nonconservative and therefore permits reduction of phase space volume. While ions in a buffer gas environment alone would eventually simply follow a random walk, the presence of the confining potential due to RF and static fields causes the ions to settle near the potential minimum, while oscillations about that minimum are damped by collisions with the buffer gas (see Figure 2.5).

For low ion energies, the effect of the buffer gas can be approximated as a viscous drag force

$$\vec{F}_{drag} = m\delta\vec{v} \tag{2.15}$$

where m and v are the ion mass and velocity, and δ is a damping coefficient related to the buffer gas temperature T, pressure P and ion mobility K_0 for the chosen gas according to

$$\delta = \frac{e}{mK_0}\frac{T_{room}}{T}\frac{P}{P_{atm}} \tag{2.16}$$

The amplitude of (macro)oscillation in the presence of buffer gas will decay exponentially according to

$$x(t) = (x_0 - x_f)e^{-\delta t} + x_f \tag{2.17}$$

where x_0 is the initial amplitude, determined by the initial transverse energy of the ion, and x_f is the final amplitude, in principle dictated by the temperature of the buffer gas.

Noble gases, especially helium, tend to be the gases of choice for buffer gas cooling. The high ionization potentials of noble gases mean that, for other ions with lower ionization potentials which interact with the buffer gas, it is energetically unfavorable for a singly charged ion to charge exchange with the buffer gas and therefore be neutralized and lost, although most multiply charged species can still charge exchange. Buffer gas cooling of multiply charged ions of most elements is therefore infeasible.

Helium, in particular, not only has the highest ionization potential, but is also the lightest of the noble gases. While the larger difference in masses reduces the momentum transfer per collision to the ion, resulting in longer cooling times, it also minimizes the probability to scatter the ion out of the potential well.

2.4 Acceptance and Emittance

In thermal equilibrium, that is, when the ions have been completely cooled by the buffer gas, the phase space density of a collection of ions confined in a harmonic potential takes the form

$$\frac{d^2N}{d\xi dp_\xi} = \frac{N\omega_{mac}}{2\pi k_B T} \exp\left(\frac{-m\omega_{mac}^2}{2k_B T}\left(\xi^2 + \left(\frac{p_\xi}{m\omega_{mac}}\right)^2\right)\right) \tag{2.18}$$

where ξ and p_ξ are the canonical position and momentum coordinates, and k_B is the Boltzmann constant. In the case where ξ represents one of the transverse coordinates in a linear RFQ, the relevant frequency ω_{mac} is the macrooscillation frequency of the ion in the pseudopotential, not the actual RF frequency. Equation 2.18 describes a Gaussian distribution in phase space with variances

$$\sigma_\xi^2 = \frac{k_B T}{m\omega_{mac}^2} \tag{2.19}$$

$$\sigma_{p_\xi}^2 = mk_B T \tag{2.20}$$

Note that, if the ions are in thermal equilibrium with the buffer gas, the temperature in the above phase space density expression is the buffer gas temperature. Therefore a colder buffer gas in principle permits a lower ion emittance. Note as well that the above temperature refers exclusively to motion in the pseudopotential well, since the motion due to the direct response to the RF field is coherent and therefore has no temperature to speak of. To clarify, strictly speaking the volume containing 100% of the particles described by the above phase space distribution is infinitely large. Therefore, as a practical matter emittance or phase space volume refers to the volume containing a certain fraction of particles described, usually 90% or 95%. Integrating Equation 2.18 out to amplitudes equal to $\sqrt{6}\sigma$ in both ξ and p_ξ

yields an emittance of

$$\epsilon_{95\%,n} \approx 6\pi \frac{k_B T}{\omega_{mac}} \tag{2.21}$$

Using Equation 2.11, the emittance can be expressed in terms of the pseudopotential depth

$$\epsilon_{95\%,n} \approx 6\pi k_B T r_0 \sqrt{\frac{m}{2eV_{pseudo}(r_0)}} \tag{2.22}$$

Thus the bunched emittance is expected to scale reciprocally with the square root of the pseudopotential depth $V_{pseudo}(r_0)$.

More generally, as the beam propagates outside of a confining potential, the emittance ellipse evolves in such a way that the position and momentum will change, but the area remains constant, as it must according to Liouville's theorem [29]. The relationship between beam emittance, the widths of particle positions and momenta, and the correlation between position and momentum is described by [30]

$$\epsilon^2_{RMS,n} = \sigma^2_\xi \sigma^2_{p_\xi} - \sigma_{\xi p_\xi} \tag{2.23}$$

Where σ^2_ξ and $\sigma^2_{p_\xi}$ are position and momentum variances, and $\sigma_{\xi p_\xi}$ is the covariance between position and momentum. For bunched beams, similar expressions can be obtained to describe the longitudinal emittance, substituting the oscillation frequency in the static trapping potential for the macrooscillation frequency derived from the pseudopotential in Equation 2.21. The longitudinal emittance can also be expressed in terms of the widths of beam energy and time spread instead of axial position and momentum. The n subscript indicates a

normalized emittance, which is a conserved quantity under acceleration or deceleration. The unnormalized emittance is the normalized emittance with the average forward momentum divided out, and is often expressed, rather than in units of action, in units of π mm mrad or π m rad. Different texts use different conventions regarding the inclusion of π; this dissertation will include it.

The ideal beam cooler and buncher should have as large an acceptance as possible, and deliver a beam with the smallest emittance possible. The acceptance of a beam cooler is defined as the maximum emittance an incident beam can possess and still be transmitted through the device with no losses, and in the case of a beam cooler and buncher is determined by the injection optics and RF settings. The ion optics act to both decelerate and focus the beam on the way into the RFQ, after which the RF parameters must be selected such that the pseudopotential is deep enough to contain the transverse momentum of the beam and still maintain stable motion, i.e. stability parameter $q < 0.9$. Design considerations made in order to maximize device acceptance and improve other performance characteristics will be discussed in the following chapter.

Chapter 3

Advanced Beam Cooler Concept

3.1 Desired Performance Characteristics

There are three basic criteria to gauge the performance of a beam cooler and buncher for rare isotopes. It must operate efficiently, the beam must be thoroughly cooled, and the process should be accomplished as quickly as possible. Simplicity of design also becomes an important characteristic for device construction and maintenance. The design of the BECOLA beam cooler and buncher incorporates design lessons from previous cooler and buncher devices, and features some new design concepts to enhance performance and simplify device maintenance, in order to satisfy the above criteria.

3.2 High Efficiency - Large Acceptance and Minimized Transport Losses

In experiments involving low rate beams, maximizing the efficiency of each stage of beam delivery is of paramount importance. In the case of beam cooling and bunching, this means injecting and capturing incident beam as efficiently as possible, and minimizing losses inside the cooler and buncher. Injecting beam efficiently means ensuring that the emittance of the incident beam fits within the acceptance of the beam cooler and buncher as much as possible.

A large device acceptance facilitates tuning the beam into the beam cooler and buncher. As the upstream optics and incident beam emittance were not known at the time of initial beam cooler design, a large cooler acceptance was particularly important. The acceptance is determined by the injection optics, or the electrode geometry and voltages applied, and the RF settings. One idea put forth by the Moore group at McGill [31] involves the use of a hyperbolic ring on high voltage to both electrostatically decelerate the beam as well as provide a cylindrically symmetric quadrupole field to focus the beam into the RFQ region (see Figure 3.1). A cone electrode is also included along the equipotential to the hyperboloid ring to mitigate the penetration of the RF field into the deceleration region.

The notion of flaring the first segment of RFQ electrodes was introduced in order to further enhance the acceptance of the system. Drawing the electrodes away from the beam axis while tapering them back in over a distance of several cm allows the beam to expand slightly after passing through the hyperboloid electrode without striking the RFQ electrodes, yet still maintains sufficient confinement to avoid ion losses. Simulations which will be elaborated on in the next chapter show that flaring out the RFQ electrodes in this manner (see Figure 3.1) enhances the acceptance of the system compared to a completely straight geometry.

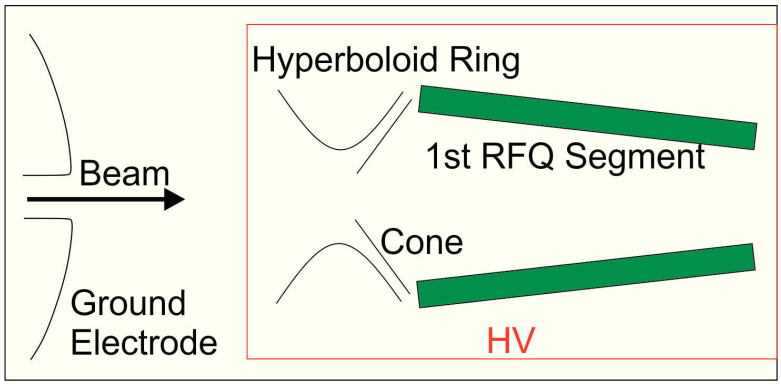

Figure 3.1: Illustration of injection electrodes for the BECOLA beam cooler and buncher.

Once the beam has been successfully transmitted into the cooler, the ions must be

transported and bunched in the cooler and buncher with as few losses as possible. A large pseudopotential, defined in the previous chapter, is crucial to efficiently transporting through the cooler as well as establishing a large acceptance. From Equation 2.1, one can see that a tighter electrode spacing results in a stronger confining potential for a given RF amplitude and frequency. Therefore the design incorporates an electrode spacing tight enough to provide superior pseudopotential confinement, yet done in such a way that the risk of RF discharge is mitigated.

Large pseudopotentials are particularly important when a next generation design seeks to accommodate high beam currents, where space charge effects will work to defocus the beam, resulting in losses when ions come into contact with electrode surfaces. From Equation 2.14, in the approximation used the maximum linear charge density attainable in a beam cooler is directly proportional to the pseudopotential, so a logical step towards a high intensity beam cooler is to operate at higher RF frequencies and amplitudes, provided one can do so and still avoid discharge.

Even in the low current limit, high pseudopotentials are still important for beam bunching. The bunch is formed in a longitudinal trap formed from a static potential, which from Equation 2.12 it is shown that such a trap weakens transverse confinement, requiring a steeper pseudopotential than is necessary in the absence of static voltage offsets.

3.3 Low Emittance and Energy Spread

The energy spread of an ion beam, which arises from longitudinal emittance, limits the attainable sensitivity of a collinear laser spectroscopy measurement. An ion pulse with a larger energy spread necessarily has a larger velocity spread, which is reflected in the Doppler

broadening of the fluorescence spectrum. It is imperative, therefore, that the beam cooler and buncher should deliver a beam with as small of an energy spread as can be attained. Beam cooling also minimizes the transverse emittance of a beam, maximizing the transport efficiency to the collinear laser spectroscopy experiment. A beam with a reduced emittance is also more easily focused and overlapped with the laser beam, which enhances the resulting fluorescence signal.

The emittance achievable by beam cooling is limited by the temperature of the buffer gas. Therefore, one can improve the performance of a beam cooler by cooling the buffer gas. The LEBIT beam cooler has been designed to do so [32], and the improvement of buncher performance by cooling the gas has been demonstrated. The option to cryogenically cool the buffer gas has been added to the design of the BECOLA cooler and buncher. Cooling of the buffer gas can be realized through the installation of a cold surface, or coldhead, inside the vacuum vessel. The buffer gas is then cooled through contact with the coldhead, thus allowing further cooling of the ion cloud.

Previous generation devices operate with the cooling and bunching regions at the same buffer gas pressure [33, 34]. Higher pressure allows for shorter cooling times, but high pressures in the extraction region outside the RFQ structure also result in more collisions with buffer gas and therefore undesired emittance growth. It is possible, however, to design a differential pumping system to maintain a higher pressure in the cooling region, where most of the transverse energy spread of the ions is removed, while maintaining a lower pressure in the buncher, where the ions are accumulated to form a pulse. The pressure can be chosen such that cooling times are still short enough that experiments with short-lived nuclides are still feasible, yet such that the mean free path is longer than the distance to the extraction electrode, thus minimizing reheating of the ions on ejection.

3.4 Simplicity of Construction and Maintenance

In the design of a mission critical device, the design should not only strive for simplicity in order to minimize this risk, but to facilitate ease of corrective action as and when something does break. From previous operational experience with other beam coolers and ion guides, loose or broken electrical connections are a common failure mode. The best practice when designing beam coolers is to minimize the number of required electrical connections, thus mitigating the risk to operation due to damaged connections.

In the high pressure cooling regions of beam coolers, static potentials are added in order to either guide the beam longitudinally through the buffer gas or form a trap for beam bunching. One popular and conceptually straightforward approach is to simply segment the RFQ electrodes and add a separate static offset to each segment, thus creating a stairstep-like drag potential [21, 20, 33, 35, 36, 37]. While this approach does accomplish the intended goal if implemented properly, in the case of long RFQ devices or fine segmentation it can lead to a large number of internal components and connections which makes construction more difficult and provides more possibilities for loose or missing connections, complicating device maintenance. It is possible to reduce the number of electrodes required to create the longitudinal drag field by simply cutting them in a different way. If, instead of cutting the electrodes into several straight segments, with the cut perpendicular to the beam axis, one instead cuts a longer segment into diagonal wedges, one can create a uniform drag field over an arbitrarily long distance, depending on how long is convenient to make each rod segment (see Figure 3.2).

If such a segmentation is employed, it is also necessary to drive each segment, regardless of bias, with the same RF signal. Such a scheme requires a potentially large network of

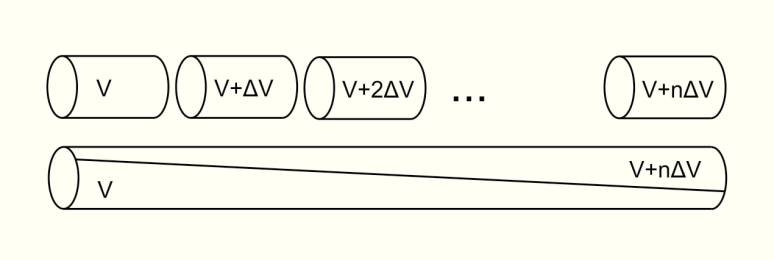

Figure 3.2: A comparison between using fine segmentation and using a diagonal crosscut to create a drag potential in a beam cooler.

capacitors or transformers to isolate the voltage offset of each segment from the RF amplifier. One can further reduce the complexity of such a system by using a common RF electrode to couple capacitively to each individual RFQ segment (see Figure 3.3). The backbone runs the length of the beam cooler and buncher, while each RFQ segment maintains a local static voltage offset on top of the RF from the backbone. Static voltage leads are fed through holes in the backbone to connect directly to each RFQ segment to provide the bias.

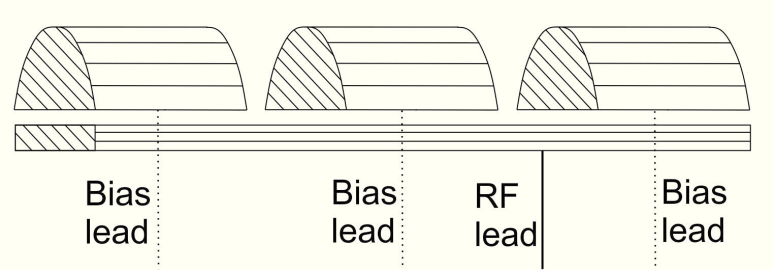

Figure 3.3: An illustration of the RF backbone coupling scheme.

A sketch of the whole BECOLA beam cooler and buncher system is shown in Figure 3.4. The beam is decelerated and focused into the RFQ structure by the injection optics, consisting of a ring shaped as a hyperboloid of revolution, and a cone with a central aperture. The voltage applied to the hyperboloid provides a cylindrically symmetric decelerating and focusing field, while the cone minimizes penetration of the RF field into the decelerating gap. The RFQ electrodes provide the transverse confinement, and the ions are injected with sufficient energy to travel into the cooling region. Collisions with the buffer gas remove excess energy

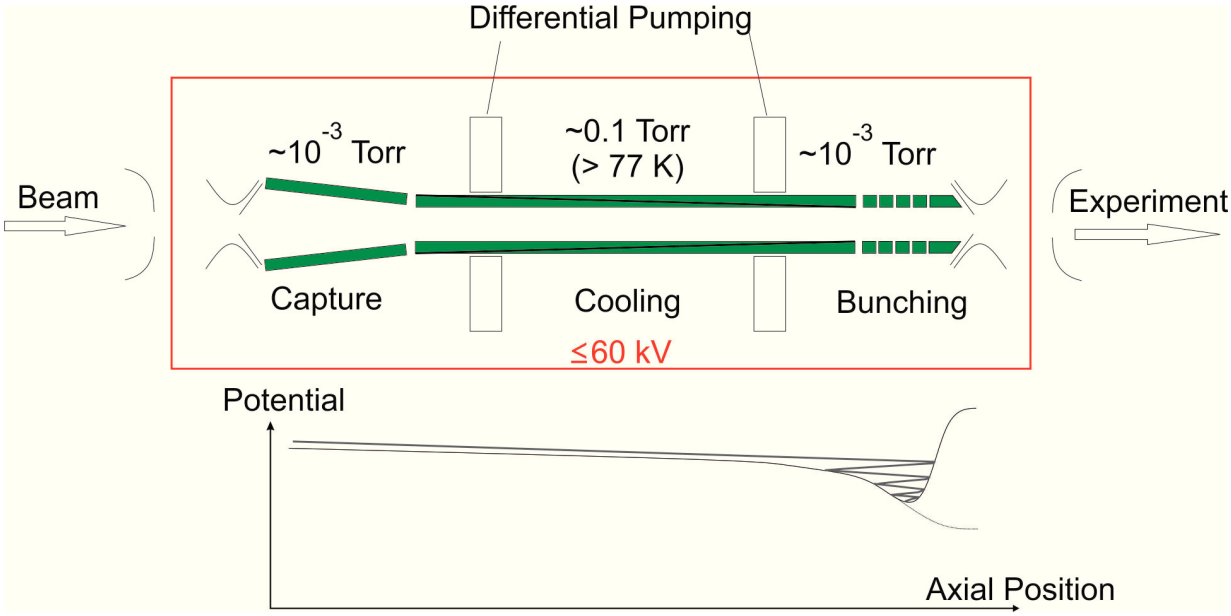

Figure 3.4: Top: A schematic of the overall structure of the BECOLA beam cooler and buncher. Bottom: A sketch of the static potential with a sample ion trajectory in grey. The dashed line on the right side of the potential indicates the potential when the ion bunch is released.

from the ions, while a drag field pulls the ions through the gas at drift velocity. Differential pumping barriers restrict gas flow from the higher pressure cooling region to maintain the regions immediately upstream and downstream at a lower pressure. Ions are collected in the bunching region using thin segmented RFQ electrodes to form a longitudinal trap. After cooling, they are released and reaccelerated.

In order to refine the design concepts discussed here, it was necessary to perform a series of simulations and prototype studies to determine the appropriate electrode and gas handling geometries for most efficient operation of the beam cooler and buncher. The results of these simulations, which are discussed in the subsequent chapter, dictated the detailed design requirements for the BECOLA beam cooler and buncher. Prototype work is discussed in Chapter 5.

Chapter 4

Simulations for the BECOLA Beam Cooler and Buncher

4.1 Simulated Characteristics of Interest

A set of simulations was undertaken using SIMION 8.0 [26] to inform the eventual design of the BECOLA beam cooler and buncher. SIMION is a widely used ion optics software package which, given an electrode geometry as an input, solves the Laplace equation for the boundary conditions specified by the individual electrode definitions to determine the electric fields which govern ion motion. SIMION also includes the ability to employ user generated programs to add functionality such as time varying fields (RF) or the effects of collisions with background gas atoms.

Device acceptance as a function of electrode geometry and RF parameters was studied. Subsequent simulations investigated RF parameters needed for ion confinement, as well as buffer gas pressure and length of cooling region required to allow for the flexibility to cool a wide range of beams of different masses. Finally, simulations of the bunching and extraction part of the beam cooler and buncher were undertaken. The effects of trapping and extraction potentials, cooling times, and ejection optics on outgoing transverse and longitudinal emittances were explored. The simulation of the beam cooler was divided into

three sections. The capture region, cooling region, and bunching region (see Figure 3.4) were all simulated separately, where ions transmitted through one stage were used as input for the subsequent stage.

4.2 Acceptance Studies

Ion optics simulations were performed to inform an injection optics design which optimizes the acceptance of the beam cooler and buncher. Key concepts include the use of a ring electrode, hyperbolic in cross section, to provide a quadrupole focusing and deceleration field, and a tighter RFQ electrode spacing for enhanced pseudopotential depth for a given RF frequency and amplitude. Variations in electrode geometry, especially the opening angle of the first set of RFQ electrodes (see Figure 3.1), were explored, as well as the effects of the injection optics and RF settings in the first stage of the RFQ where the beam is captured within the device after the injection optics. Unless otherwise noted, simulation parameters for acceptance studies are listed in Table 4.1.

An incident beam of 60 keV was used, with a phase space of uniform density large enough to envelope the acceptance of the injection optics. For the purpose of acceptance studies, the simulation geometry included the deceleration and injection optics and RFQ electrodes for several cm, long enough for the incident ions to execute multiple macrooscillations. If the ions traveled 15 cm deep into the 1st RFQ section, where they would be free to execute stable motion dictated by the RF parameters, the ions were said to have been accepted into the device, and would contribute to the calculation of the acceptance ellipse. The beginning and final phase space coordinates, or transverse positions and momenta, of a collection of ions were recorded, and the starting values of the ions which were transmitted into the device

without striking an electrode surface were used to calculate the size and orientation of the acceptance ellipse. The uncertainties of all simulated acceptance and emittance results in this chapter were calculated from statistical variation, assuming a relative uncertainty $\sqrt{2/N}$, where the factor of 2 arises from the variation of two independent parameters, position and momentum. Typical values of N varied from 700 to 1000, yielding a relative uncertainty of about 5%.

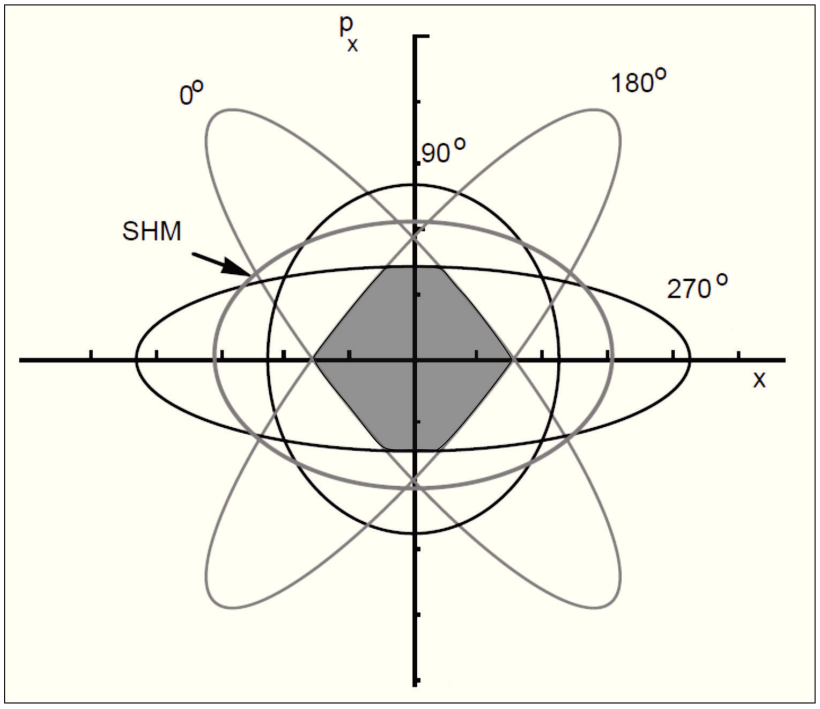

Figure 4.1: Sketch of emittance or acceptance ellipses at different RF phases. The SHM (simple harmonic motion) curve refers to the motion in the pseudopotential for all RF phases. The shaded grey area illustrates the RF independent region for the given phases. Adapted from [38, 39].

The orientation of the acceptance ellipse of an RF based device depends on the phase at which the beam encounters the RF field, as is illustrated in Figure 4.1. However, since the incident beam is continuous, all RF phases are sampled. In order to quantify the acceptance of the beam cooler and buncher, the intersection of all phase-specific acceptance ellipses was calculated from simulation results and is called the "RF independent" acceptance, since ions

in this region of phase space will be accepted into the beam cooler regardless of RF phase. The RF independent acceptance is interpreted as the device acceptance for a continuous beam.

The acceptance is calculated using the recorded initial phase space coordinates of the ions which are successfully transmitted into the cooler. One can explicitly calculate the emittance of a beam, or in this case the acceptance of a device, using the transverse position and momentum variances and covariance according to [30] (see also Equation 2.23)

$$\epsilon_{RMS}^2 = \langle x^2 \rangle \langle x'^2 \rangle - \langle x x' \rangle^2 \tag{4.1}$$

The simulated incident beam was modeled as a uniform phase space density inside a certain area, and is zero outside of that area. A uniform distribution was used in order to map out the entire area of the device acceptance, as opposed to a Gaussian distribution used to represent a typical incident beam. It can be shown that the area of uniform phase space density whose boundary is defined by the device acceptance is equal to $4\epsilon_{RMS}$.

One of the novel ideas incorporated into the design for the BECOLA beam cooler and buncher involved flaring the first section of RFQ electrodes open in order to allow the beam to expand before tapering the rods further in towards the beam axis to produce a more gradually increasing RF confining field. As part of the simulations to determine the cooler and buncher design parameters, the effect of taper length and angle were investigated. Figures 4.3 and 4.4 illustrate two such sets of studies. The cases with 7 cm long 3° taper and 15 cm long 2° taper offer large acceptances with relative insensitivity to incident energy. The effects of the flared and tapering RFQ electrodes were studied with RF voltage of 3 kV peak to peak and frequency of 8.65 MHz, resulting in a stability parameter q of 0.4 and a pseudopotential

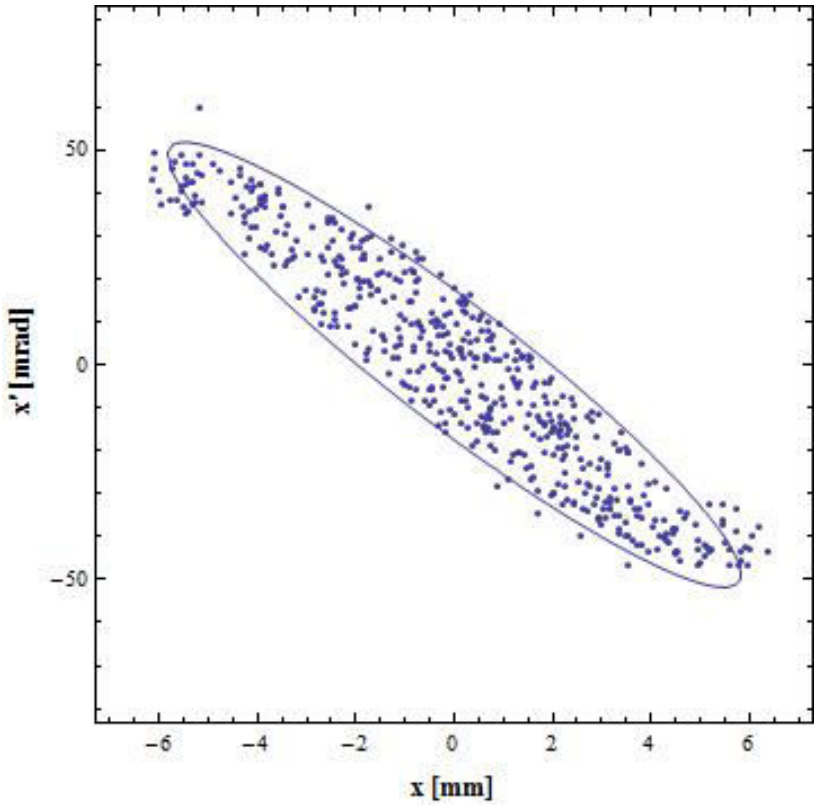

Figure 4.2: Example of a simulated acceptance. Points are individual ion phase space coordinates, while the curve represents the calculated phase space ellipse. This particular example gives an acceptance $4\epsilon_{RMS}$ of about 100 π mm mrad.

depth of 150 V for a mass 40 beam. The injection energy in these and subsequent acceptance study plots refers to the difference between the incident beam energy and the bias applied to the first set of RFQ electrodes. For example, if the incident beam has an energy of 60 keV, and the cooler and buncher is floated to a potential of 59.5 kV, with an additional bias of 100 V on the RFQ rods specifically, the injection energy in this case is 400 eV.

The dependence of the cooler acceptance on RF parameters was also simulated. In particular, the RF voltage and frequency were varied to study the effects of the stability parameter q and the pseudopotential depth, keeping one constant while scanning over the other, according to Equations 2.1 and 2.7. As can be seen in Figures 4.5 and 4.6, the acceptance is maximized for small q and large pseudopotential depth. In particular, the

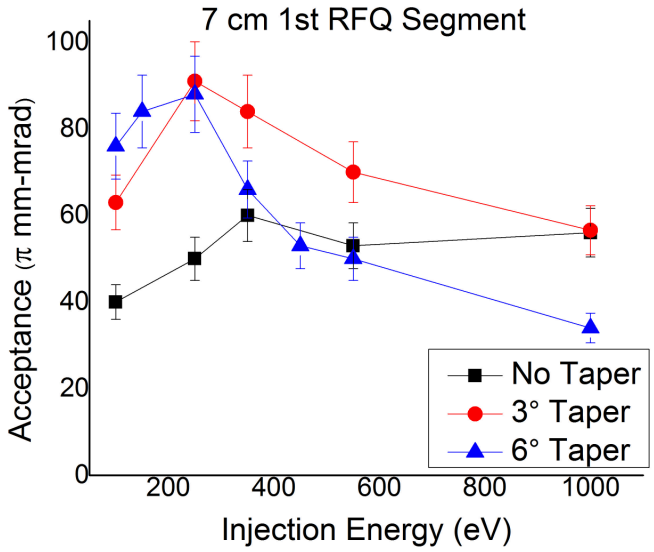

Figure 4.3: Plot of simulated acceptances as a function of injection energy and opening angle of the 1st tapered segment of RFQ electrode for 7 cm length.

RF independent acceptance benefits significantly from a smaller q, though a simple RMS calculation shows little effect. This effect can be explained in terms of an RF distorted action diagram such as in Figure 4.1. For a large q, where the phase-specific ellipse might be quite large, as the RF voltage evolves and the ellipse distorts and moves, the area circumscribed by all phase ellipses might be quite small. Therefore certain portions of phase space outside the RF independent acceptance may be transmitted with an efficiency dictated by what fraction of time that region remains in the phase-specific acceptance ellipse. To minimize the rotating ellipse effect, a small q is recommended, which in conjunction with a large pseudopotential, means a system must be designed to operate with as large an amplitude and as high a frequency as can be sustained.

Finally, the effect of ion mass on cooler acceptance was investigated as well. Since it is desirable to perform collinear laser spectroscopy measurements on a variety of different nuclides, the beam cooler and buncher must be capable of delivering as wide a range of masses

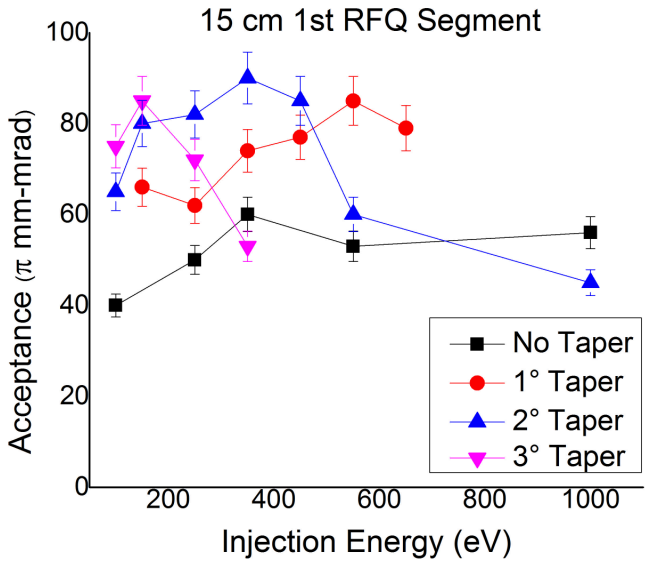

Figure 4.4: Plot of simulated acceptances as a function of injection energy and opening angle of the 1st tapered segment of RFQ electrode for 15 cm length.

as possible in the chart of the nuclides. Figure 4.7 shows the results of RF independent acceptance simulations for different incident masses, both for fixed RF voltage and frequency, as well as for fixed stability parameter q and pseudopotential depth. Provided that the stability parameter and pseudopotential depth, themselves functions of ion mass, are adjusted to hold constant values, cooler acceptance is insensitive to ion mass. For fixed RF voltage and frequency, the cooler acceptance has a maximum value for an intermediate mass, with values decreasing either for lower mass, due to rising stability parameter value, or for higher mass due to shrinking pseudopotential depth. For best device operation, the RF circuitry must be broadly tunable to select RF parameters for a variety of incident ion masses.

To maximize device acceptance, a large pseudopotential depth and a small stability parameter are necessary, meaning that larger frequencies and amplitudes are desired. In addition, to accommodate a range of incident masses, the frequency and amplitude should be adjusted to maintain a large pseudopotential depth and a small stability parameter.

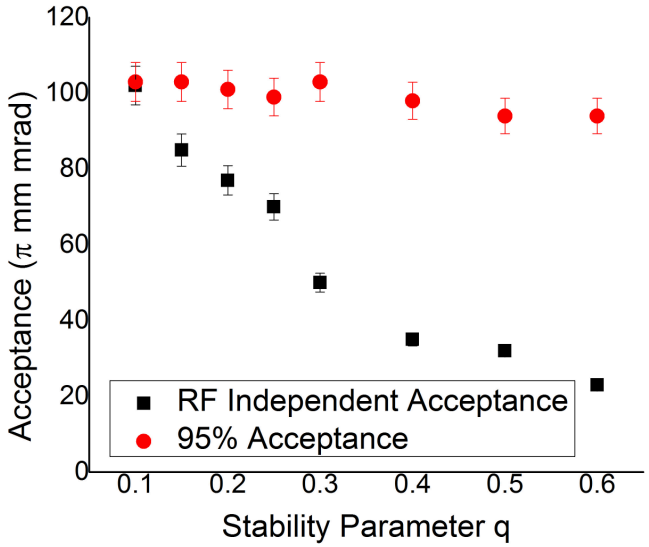

Figure 4.5: Simulated acceptance as a function of the stability parameter q chosen such that the pseudopotential at the electrode surface is 75 V using a mass 20 beam. Both 95% and RF independent acceptances are plotted.

Increasing the spacing of the first set of RFQ electrodes and tapering them down to the design r_0 further enhances device acceptance. Setting the RFQ bias to maintain an injection energy of about 200 V results in a large acceptance. The length of the deceleration gap, from the tip of the ground electrode to the center of the hyperboloid, affects the orientation of the acceptance ellipse but not the size. Other parameters, such as hyperboloid and cone electrode voltages, were found to not have a significant impact on acceptance, unless the voltages were so large as to block transmission altogether.

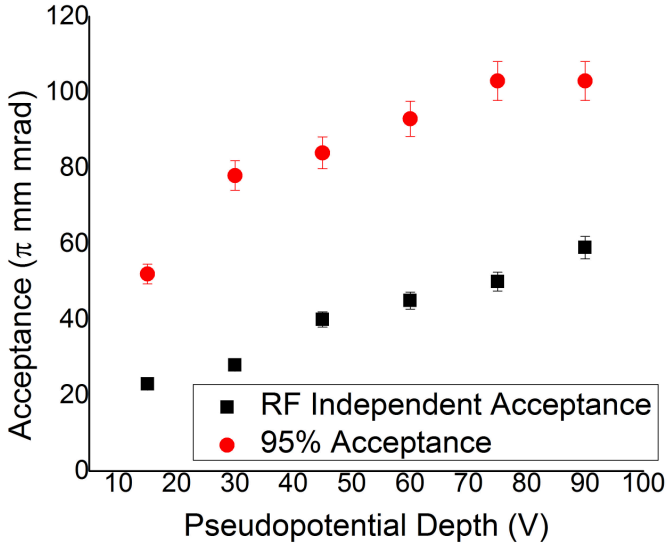

Figure 4.6: Simulated acceptance as a function of the pseudopotential depth chosen such that the stability parameter q is 0.3 using a mass 20 beam. Both 95% and RF independent acceptances are plotted.

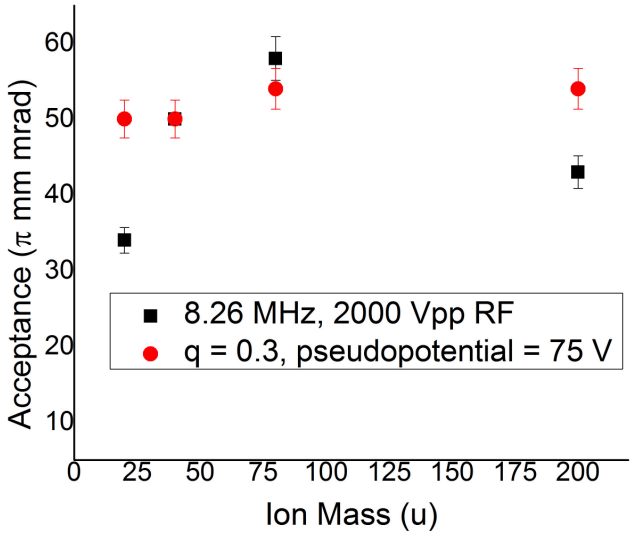

Figure 4.7: Simulated RF independent acceptance as a function of the ion mass.

Parameter	**Value**
Incident Beam Energy	60 keV
Beam Mass	40 amu
Ion Charge	+1
High Voltage	59.6 kV
Hyperboloid Voltage	1.5 kV
Cone Voltage	-2 kV
RFQ Bias	200 V
RF Frequency	8.26 MHz
RF Amplitude	1 kV
Taper angle	2°
1st RFQ length	15 cm
Deceleration Gap Length	50 mm
Electrode to Beam Axis	3.5 mm

Table 4.1: Parameters used for simulation of injection of incident beam into the cooler and buncher, unless otherwise indicated in results figures. All biases are with respect to the high voltage bias.

4.3 Simulations of Cooling Region

As shown in Figure 3.4, after the ion beam is successfully injected into the first stage of the beam cooler and buncher, it travels through the first differential pumping channel into the cooling region. Simulations were performed to fine tune the shape of the drag field electrodes and the overall length of the cooling region. A collection of ions transmitted from the acceptance simulations was used as the input for the cooling region simulation, with the ions situated far enough into the RFQ structure that edge effects could be neglected. Ions which arrived within 2 cm of the downstream edge of the RFQ rods were said to have reached the edge, again to avoid simulated edge effects. The effects of the buffer gas were modeled using a hard sphere collision routine in conjunction with the existing static and RF potentials. The collision cross sections were modified to reflect experimental mobility data for different ion energies [40, 41].

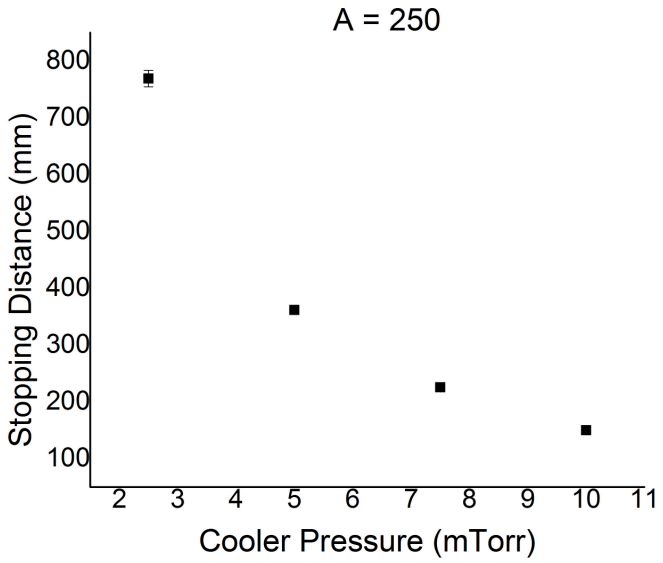

Figure 4.8: Characteristic simulated stopping distance versus buffer gas pressure for a mass 250 u beam. Stopping distances are the result of exponential fits of average ion energy versus distance in the presence of buffer gas.

For the most effective operation, the majority of ion energy must be removed in the high pressure region before the ions are bunched. To this end, the cooler should be designed to be long enough and operate at sufficient pressure to cool any incident beam. From Equation 2.16, we expect the damping effect to be less prominent for heavier beams. To account for a worst case scenario, simulations were performed using a hypothetical mass 250 u beam, and characteristic stopping distances are plotted as a function of buffer gas pressure in Figure 4.8. For each pressure, the average ion energy was recorded as a function of distance and fitted to an exponential $f(z) = e^{\frac{-z}{z0}}$, and the z_0 values are plotted as a function of cooler pressure. The quoted uncertainties are the standard error calculation results for the associated fit parameters. While it is in principle possible to design a short, high pressure device, the maximum pressure permissible is limited by the Paschen discharge voltage for a given RF amplitude. The results of these simulations, in conjunction with those from discharge tests carried out using a prototype electrode structure (see chapter 5), informed the design for the final cooling length.

The drag field electrode shapes were also simulated in order to verify that a suitable drag field could be obtained from the proposed geometry. Drag field refers to the electric field parallel to the beam axis that prevents the ions from losing all of their forward momentum and being stopped completely in the buffer gas. Each drag field electrode pair has a gap which runs diagonally across the surface, as illustrated in Figure 4.9. The cut along the electrode surface permits a gradually changing potential for a smooth drag field. The dotted line in Figure 4.9 extending from electrode centerline illustrates how far out the crosscut extends, and it is this quantity which is varied from one curve to the next in Figure 4.10. Drag potentials were simulated for different crosscut geometries, where each geometry is quantified by the maximum distance from the center of the electrode the gap travels. Simulation results,

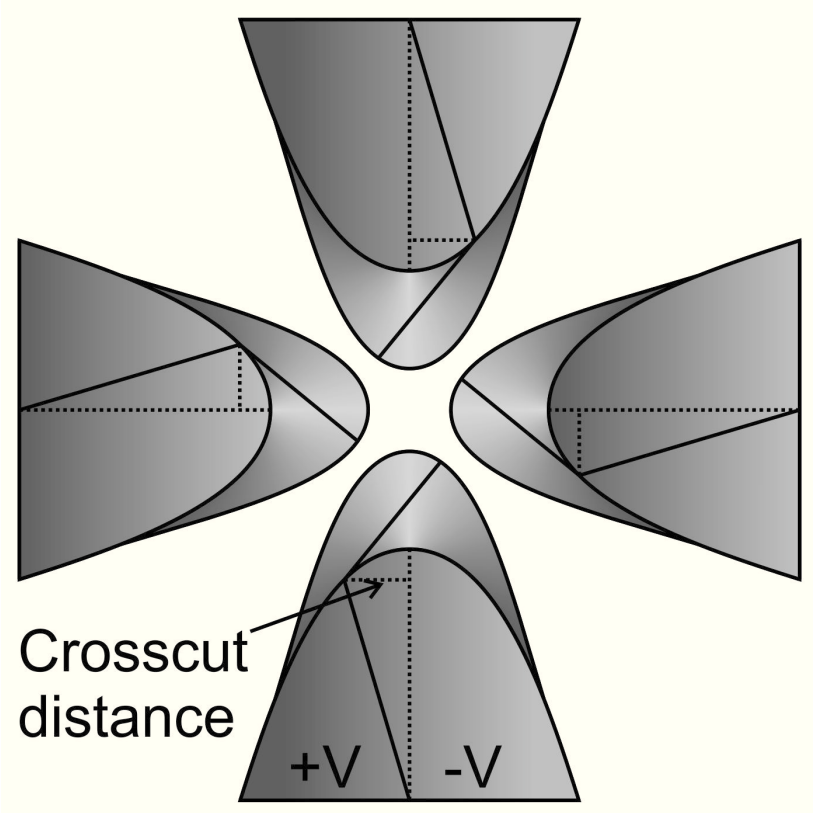

Figure 4.9: Sketch of crosscut geometry looking along the beam axis.

shown in Figure 4.10, indicate that excursions away from the central axis less than $\frac{r_0}{2}$, where r_0 is the distance from the electrode tip to the beam axis, the resultant field is quite uniform. Larger deviations result in flat regions near electrode edges.

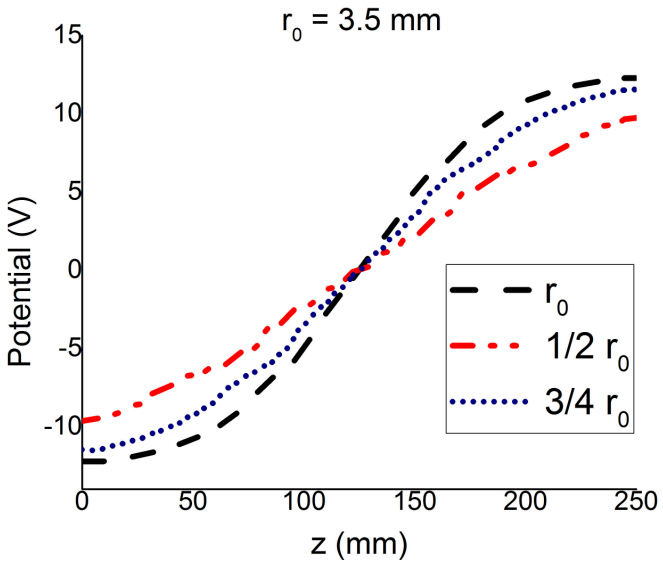

Figure 4.10: On-axis drag potentials for different crosscut distances (see Figure 4.9). Curves are labeled by how far away from the central axis the crosscut sits at the edge of the electrode. r_0 refers to the distance from the electrode tip to the central beam axis.

4.4 Bunching and Ejection Simulations

Simulations of the bunching and extraction portion of the BECOLA beam cooler and buncher were carried out to guide the design and to understand what operating parameters should be used for the experiments. Upon exiting the high pressure cooling region described in the previous section, ions were bunched in a longitudinal trap as illustrated in Figure 4.11. A set of four segmented RFQ electrodes, downstream of the last drag field electrodes, are used to apply the trapping potential (bottom portion of the figure). The presence of buffer gas damps ion motion as in the cooler region, causing ions to cool and accumulate near the trap minimum (grey trace). The voltage on the last RFQ electrode is then switched down (dashed trace) to permit the ion pulse to leave the trap and reaccelerate back to < 60 keV.

A pressure of 1.5 mTorr was applied in the bunching region, and the ions were held in the buncher for 820 μs, a little over twice the damping time constant of about 370 μs. The same hard sphere model used in the cooler simulations was used in the bunching region. Initial conditions were determined by the ions which were successfully transmitted through the cooling region. Unless otherwise specified, the simulations were perfomed with RF amplitude and frequency of 460 V peak to ground and 5.3 MHz, resulting in stability parameter and pseudopotential depth of 0.33 and 38 V respectively for a mass 39 beam. A longitudinal trap depth (compared to the last segment of drag electrode) of 2.5 V was used, and the extraction field was 0.76 V/mm. A final ion ejection energy of 29.85 kV was used. This was dictated by the maximum bias achievable by the built device. Ion transverse emittances, time and energy spread were recorded upon arrival at the field free region inside the ground electrode as sketched in Figure 4.11. Simulations of emittance, time and energy spread were performed as a function of pseudopotential depth, stability parameter, switching voltage slew

time, longitudinal trap depth and extraction field. Typical simulation settings are listed in Table 4.2.

Transverse emittances were calculated from the variances and covariances of particle positions and angles according to Equation 4.1, similar to the acceptance studies described earlier. The RMS value was multiplied by 6, to produce a 95% confidence interval value for a bi-Gaussian distribution. The time and energy spreads were, in general, not symmetric, and therefore could not be reliably fit to Gaussian functions. The energy and time of flight spectra were fit to Fermi-Dirac type functions multiplied by an exponential decay. Such a function takes the form $f(x) = \frac{e^{-x/x_0}}{1+e^{-x/x_1}}$, where x represents either energy or time depending on the spectrum in question. The different decay constants x_0 and x_1 account for the peak asymmetry, and once determined from the fit routine are used to calculate the full width at half maximum (FWHM), which is quoted as the width of the relevant spectrum. Error bars in simulated transverse emittances are statistical, as with the acceptance studies.

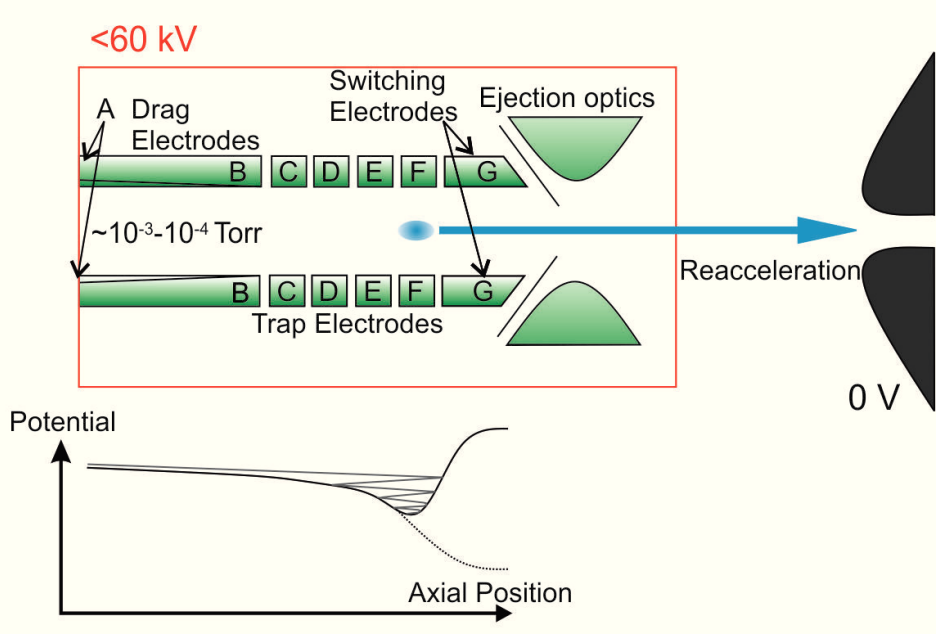

Figure 4.11: Sketch of the buncher and extraction portion of the BECOLA beam cooler and buncher.

Parameter	**Value**
Beam Mass	39 amu
Ion Charge	+1
High Voltage	29.85 kV
Hyperboloid Voltage	-1 kV
Cone Voltage	-1 kV
Drag Electrode A Bias	10 V
Drag Electrode B Bias	1 V
Trap Electrode C Bias	0.015 V
Trap Electrode D Bias	0.015 V
Trap Electrode E Bias	-0.02 V
Trap Electrode F Bias	-5.75 V
Switching Electrode G Trapping Bias	18 V
Switching Electrode G Extraction Bias	-6 V
Slew Time	5 μs
RF Frequency	5.3 MHz
RF Amplitude	460 V
Buncher Pressure	1.5 mTorr
Bunch Time	820 μs
Number of Ions	800

Table 4.2: Parameters used for simulation of ejection of bunched beam, unless otherwise indicated in results figures. All biases are with respect to the high voltage bias. Electrode labels refer to those found in Figure 4.11.

4.4.1 Simulated Beam Properties versus Pseudopotential

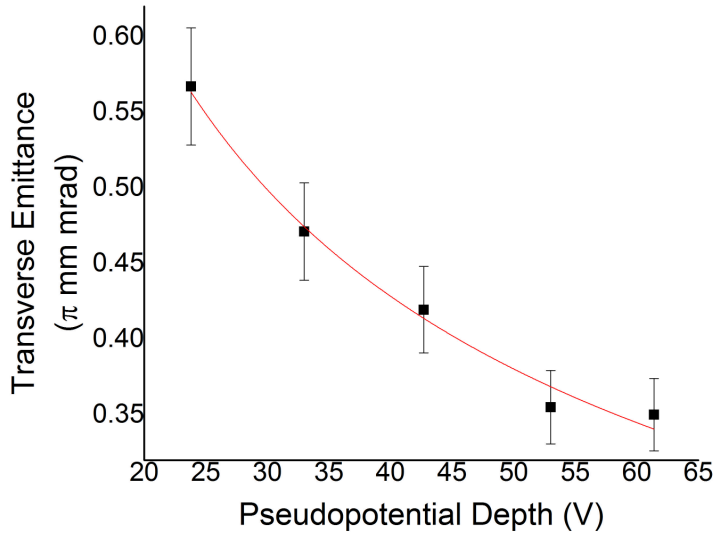

Figure 4.12: Plot of simulated extracted transverse emittance versus pseudopotential depth $V_{pseudo}(r_0)$ (see Equation 2.1). A fit of the data to a function of the from $f(V) = a + \frac{b}{\sqrt{V}}$ is shown in red.

Figure 4.12 shows the results of simulated ejected transverse emittances as a function of RF generated pseudopotential depth, while Figures 4.13 and 4.14 illustrate the results of simulating time and energy spread versus pseudopotential. The RF frequency and voltage were varied in such a way as to scan over pseudopotential (Equation 2.1) while maintaining a constant stability parameter value of 0.38 (Equation 2.7). From Equation 2.22, the extracted emittance is expected to scale inversely with the square root of the pseudopotential depth, and simulation agrees with prediction as illustrated in Figure 4.12. A reduced χ^2 value of 0.18 was obtained, with an offset consistent with zero.

Ideally the transverse and longitudinal degrees of freedom are decoupled, therefore changes in the transverse confining pseudopotential should have little effect on the longitudinal time spread and energy width. Figure 4.13 shows that this is indeed the case for time spread,

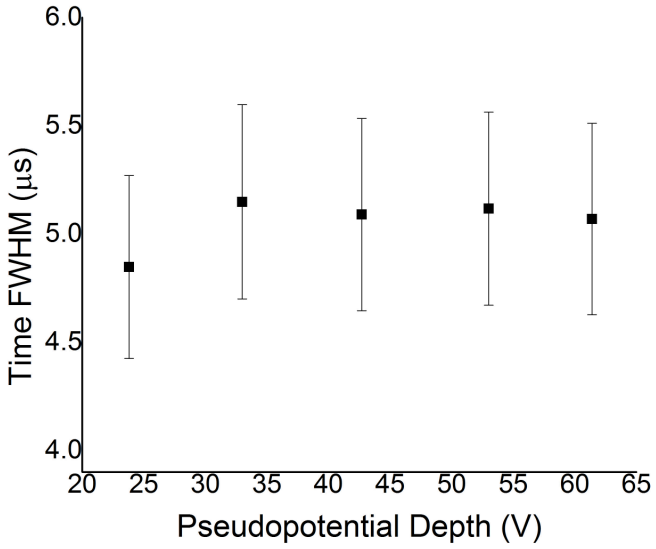

Figure 4.13: Plot of the simulated full width at half-maximum (FWHM) of the extracted time of flight spectra as a function of pseudopotential depth.

though an increased pseudopotential does result in slight broadening of ion energy spread as shown in Figure 4.14. The RF field penetrates partially into the reacceleration region, however, at which point any off-axis ions may experience a longitudinal field component. Since the time spread of the ions is much longer than the RF period, the ion cloud samples all RF phases, thus experiencing the full range of potential variation due to RF oscillation.

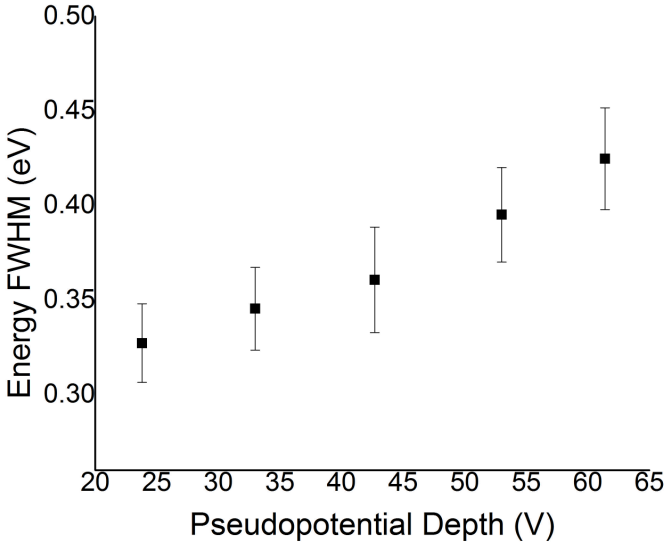

Figure 4.14: Plot of simulated energy spread of extracted ion pulses versus pseudopotential depth.

4.4.2 Simulated Beam Properties versus Stability Parameter

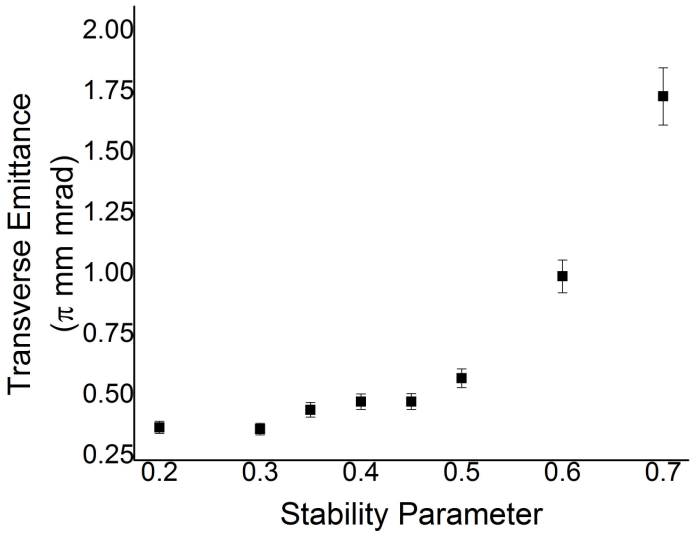

Figure 4.15: Plot of simulated extracted transverse emittance versus stability parameter q (see Equation 2.7). RF voltage and frequency were varied in such a way as to keep the pseudopotential (see Equation 2.1) constant.

The effects of the stability parameter q (Equation 2.7) on transverse emittance, time of flight width and energy spread were also investigated, while the pseudopotential was held constant at 33 V. Figure 4.15 shows only slight dependence of extracted emittance on q for values less than 0.5, but has a dramatic effect for larger q values. Although the pseudopotential is held constant, a larger q nonetheless results in larger microoscillations [39] which, upon exit from the RFQ region, can result in a larger effective emittance. As with the pseudopotential study, the stability parameter has little effect on time spread (see Figure 4.16), which is consistent with expectation. The effect of the stability parameter on energy width, shown in Figure 4.17, is caused by a larger radial extent of the ion cloud due to larger microoscillations, which samples a larger off axis RF field on extraction, resulting in a larger energy spread.

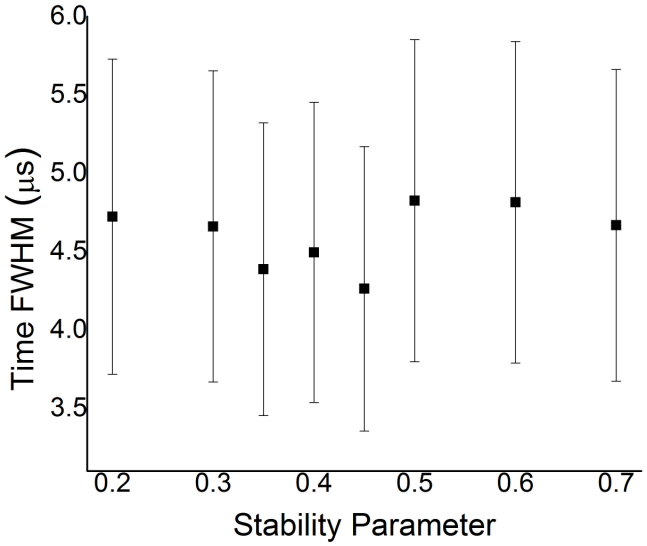

Figure 4.16: Plot of the simulated time spread of extracted pulses as a function of stability parameter.

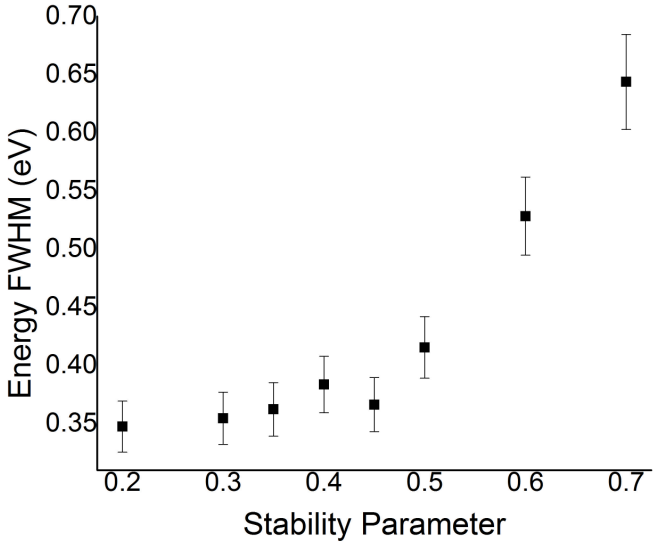

Figure 4.17: Plot of the simulated energy spread of extracted pulses as a function of stability parameter.

4.4.3 Simulated Beam Properties versus Slew Time

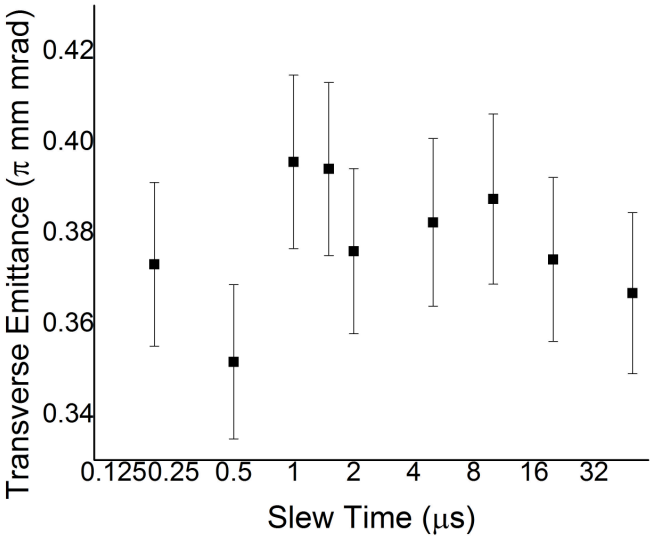

Figure 4.18: Plot of simulated extracted transverse emittance versus extraction voltage slew time.

Simulations were performed to examine the effect of the rate at which the buncher potential was opened to release the ion pulse, or the slew time of the voltage switch. The static voltage applied to the last RFQ segment during bunching was ramped down from +18 V to -10 V to release the ions from the trap. The voltage was ramped exponentially with different time constants, and transverse emittance, time spread and energy spread were recorded for different time constants. The results are plotted in Figures 4.18, 4.19 and 4.20. In the limit of very fast voltage changes, one expects that a sudden change in potential will introduce an energy spread, comparable to the axial size of the ion cloud multiplied by the local ejection field, in addition to minimizing the time width. In the other limit, a slow ramp rate amounts to an adiabatic shift in potential, thus minimizing the energy spread due to changing potential while also adding a time spread. The relevant time scale for comparison is the oscillation period of the ion in the longitudinal trap, which is 5 μs for the trap settings

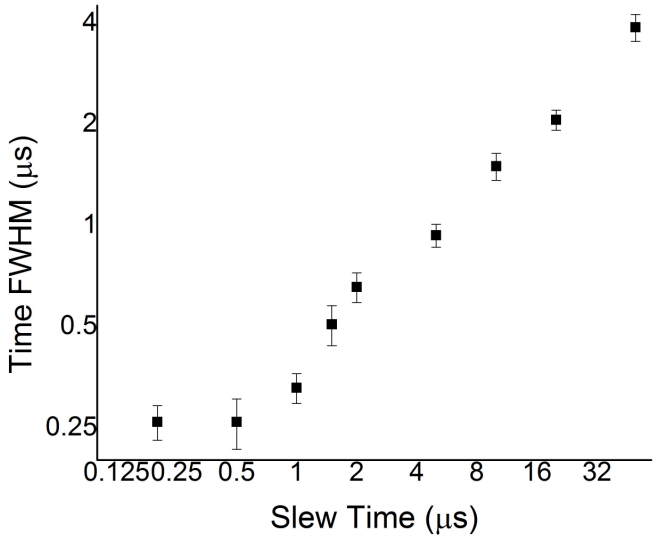

Figure 4.19: Plot of the simulated time spread of extracted pulses as a function of slew time.

used here. Both the time and energy spectra show changes in behavior near the 1 μs time scale, or a fraction of the time an ion takes to traverse the longitudinal trap. The increase in time spread with increasing slew time is consistent with prediction, and the relatively small effect on the energy is likely due to the relatively weak extraction field employed.

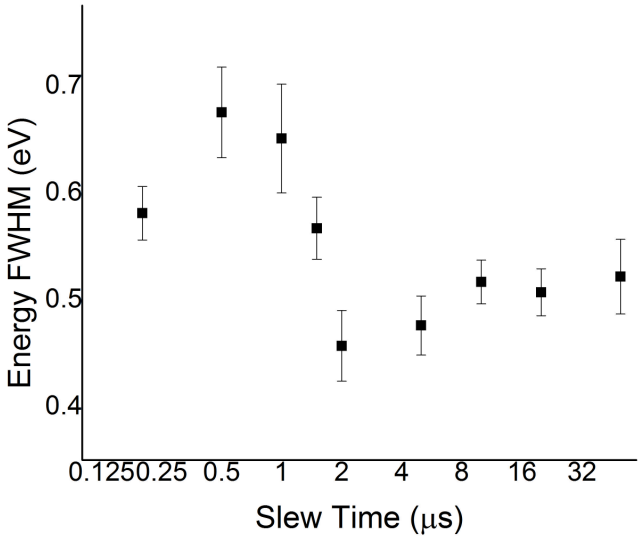

Figure 4.20: Plot of the simulated time spread of extracted pulses as a function of slew time.

4.4.4 Simulated Beam Properties versus Longitudinal Trap Depth

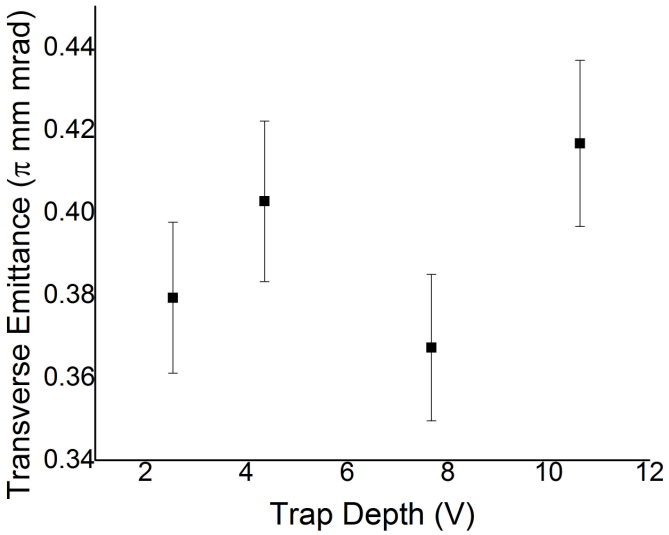

Figure 4.21: Plot of simulated extracted transverse emittance versus longitudinal trap depth.

The results of simulations of energy and time spreads versus longitudinal trap depth are shown in Figures 4.22 and 4.23. Trap depths were varied in such a way as to maintain the extraction field fixed at 0.76 V/mm. The longitudinal trap depth is defined as the potential difference between the well minimum and the edge of the drag field before the bunching region. Realistic potentials were calculated using SIMION generated potential arrays to determine the actual potential on axis when the quoted electrode biases were applied. The trap depth was varied by adjusting the voltage applied to trapping segment F (see Figure 4.11). Once again, an exchange between energy and time width is observed. A deeper trap is likely to confine the ions to a smaller axial extent and produce stronger fields closer to the trap center, which will tend to result in shorter pulses but with a larger energy spread, which is consistent with simulation. As with the slew time, the longitudinal trap depth is expected to have minimal impact on the transverse emittance, and apart from some scatter the simulation

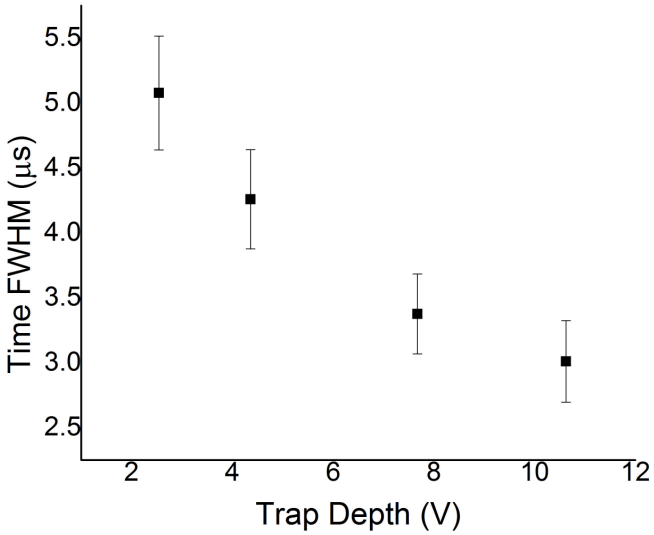

Figure 4.22: Plot of simulated extracted time width versus longitudinal trap depth.

results in Figure 4.21 bear that out.

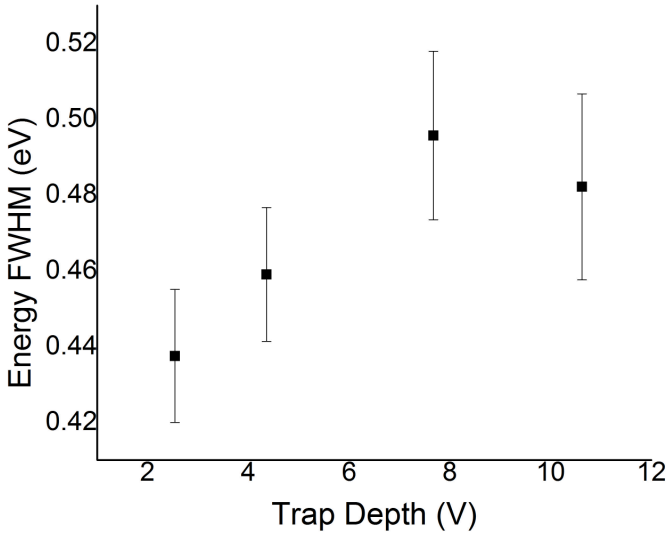

Figure 4.23: Plot of simulated extracted energy spread versus longitudinal trap depth.

4.4.5 Simulated Beam Properties versus Extraction Field

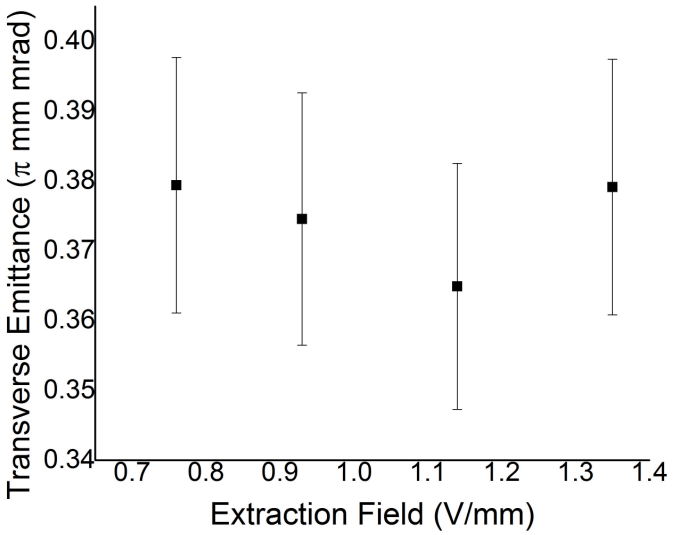

Figure 4.24: Plot of simulated extracted transverse emittance versus extraction field at the trap center.

Bunching simulations were performed to explore the impact of the extraction field on outgoing beam properties. The results are shown in Figures 4.24, 4.25 and 4.26. As with sharper trapping potentials, a stronger longitudinal field is likely to compress the ions in time, but introduce an energy spread, which can be seen in the simulation data. Once again, the extraction field, a longitudinal field, has little effect on the transverse emittance.

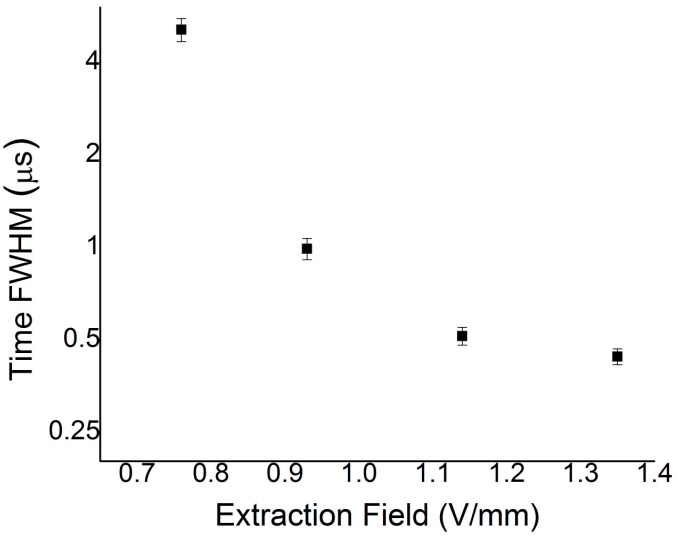

Figure 4.25: Plot of simulated extracted time width versus extraction field at the trap center.

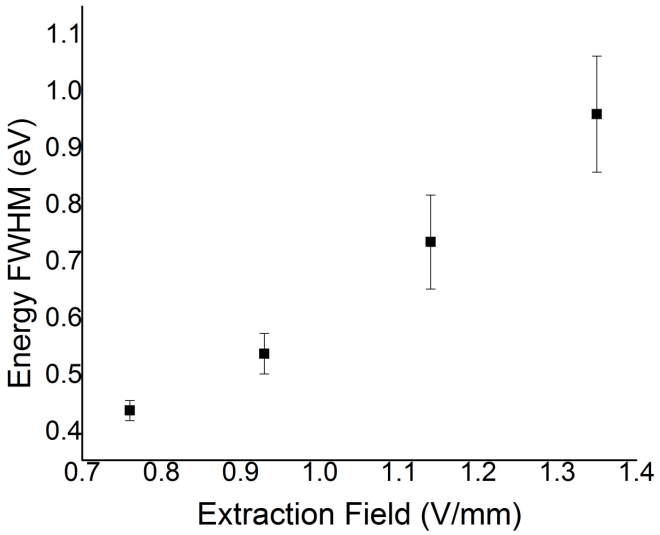

Figure 4.26: Plot of simulated extracted energy spread versus extraction field at the trap center.

4.4.6 Buncher and Ejection Simulation Results Summary

To minimize simulated extracted emittance, the RF voltage and frequency should be operated to maximize pseudopotential depth while maintaining a small stability parameter, as with maintaining a large device acceptance. However, a larger pseudopotential does modestly increase the energy spread of the outgoing beam, which must be weighed against the advantage of having a smaller transverse emittance. The RF parameters had little effect on the simulated time width of extracted beam bunches. A longer slew time for opening the buncher trap results in a longer time distribution, though with a smaller energy spread for times less than 2 μs. Longer slew times than 2 μs have little effect on the energy spread. The slew rate has little effect on the transverse emittance. Sharper longitudinal potential gradients, in the form of either a deeper longitudinal trap or a stronger extraction field, result in decreased time spread of the ion bunch, at the expense of increasing the energy width, while having little discernible effect on the transverse emittance.

4.5 Differential Pumping Simulations

Gas flow simulations were also carried out in order to characterize the length and diameter of the differential pumping regions required in order to maintain the cooling and bunching regions of the cooler and buncher at different pressures. A user program was used with the SIMION software to adapt what is normally an ion optical routine to mimic individual gas atoms in the molecular flow limit to model gas flow through a narrow channel. In the molecular flow limit, gas atoms free stream through empty space until they come into contact with a solid surface, from which they are re-emitted with a $\cos(\theta)$ angular distribution consistent with diffuse reflection from a surface [42]. A collection of gas atoms was initiated

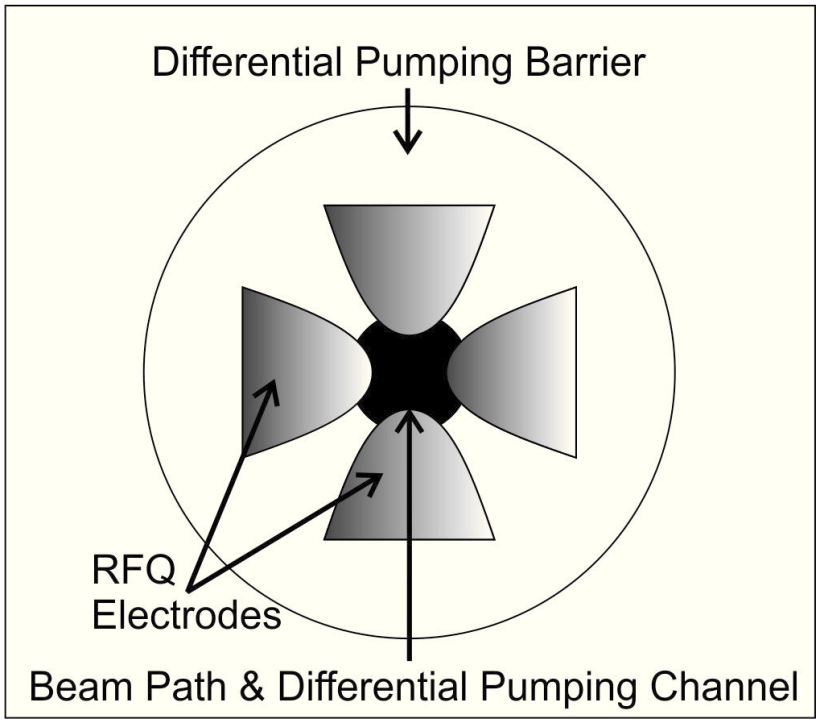

Figure 4.27: Sketch of differential pumping channel cross section.

at one end of the differential pumping channel, attached to a high pressure chamber, and the average time for the gas atoms to migrate to the low pressure side of the channel was calculated, using a calculated average velocity of 1000 m/s based on gas temperature and mass. The uncertainties in the conductance are calculated from the statistical variation of gas atom transit time through the differential pumping channel.

A sketch of the differential pumping channel is shown in Figure 4.27. The electrodes, in gray, are surrounded by an insulating material, in white, apart from a central region through which ions (and gas) are permitted to pass, shown in black. To determine the conductance, a channel length of 10 cm is modeled, and the conductance is plotted as a function of the outermost "radius" of the open (black) region in Figure 4.28. The distance from the electrode tip to the central axis is taken to be 3.5 mm. The RFQ electrodes cause the departure of the simulated conductance from the cylindrical result.

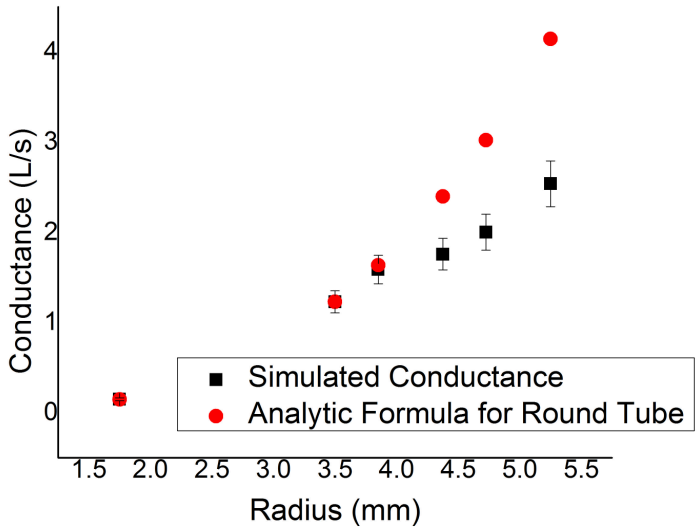

Figure 4.28: Simulated conductance of differential pumping channel as a function of radius of open region (black central region of Figure 4.27), compared to the calculated value for a cylindrical tube. A channel length of 10 cm was used in simulation.

To determine the conductance of the channel, one looks to the relationship between gas throughput, conductance and pressure [42]

$$Q = C(P_{high} - P_{low}) \tag{4.2}$$

where Q is the gas throughput, C is the channel conductance, and P_{high} and P_{low} are the high (cooler) and low (buncher or capture region) pressures at either end of the differential pumping channel (see Figure 4.29). The throughput can be interpreted as the power needed to transport a quantity of gas across a given plane [42], or

$$Q = \frac{d}{dt}(PV) \tag{4.3}$$

taking average values, we have

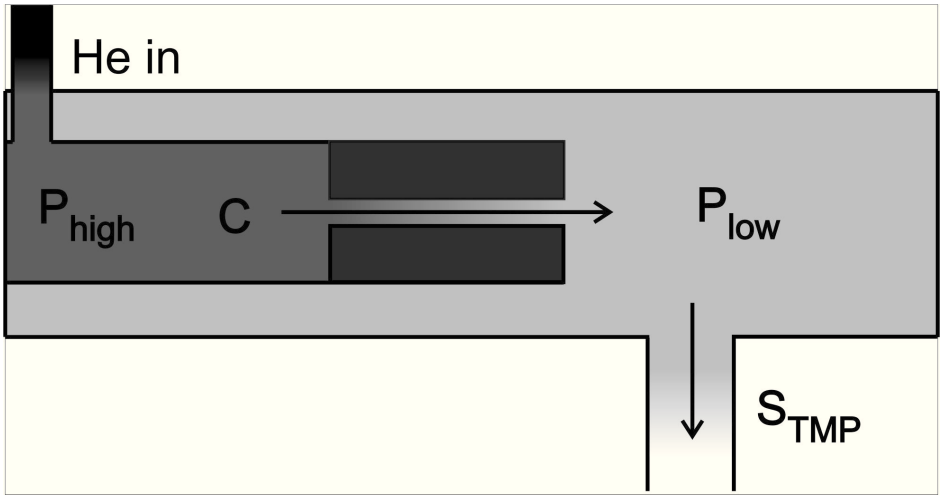

Figure 4.29: Illustration of a portion of the vacuum system involved in calculating the differential pumping channel conductance. A helium inlet feeds gas into the high pressure cooling region, while gas flow out of the cooler is restricted by the differential pumping channel. The buncher region of the vacuum chamber is pumped directly by a turbomolecular pump.

$$Q \approx \frac{\langle P \rangle V}{\langle t \rangle}. \tag{4.4}$$

If we take the approximation $P_{high} \gg P_{low}$, then

$$\frac{P_{high} V}{2\langle t \rangle} \approx C P_{high} \tag{4.5}$$

thus once the average transit time has been simulated and the channel cross-sectional area and length have been calculated, the conductance can be determined. In order to establish a relationship between the differential pumping conductance and the cooler and buncher pressure, we can appeal to continuity. That is, the throughput through the entire system must be constant. From Figure 4.29 and Equation 4.2, and once again requiring $P_{high} \gg P_{low}$,

$$C P_{high} \approx S_{TMP} P_{low}. \tag{4.6}$$

Where S_{TMP} represents the pumping speed of the turbomolecular pump used to pump down the chamber. Note as well that the RFQ rods themselves will restrict gas flow, thus reducing the effective speed of the pump. If a pressure ratio of about 100:1 is desired between the cooler and buncher regions, assuming an effective pumping speed of about 100 l/s, the design for the differential pumping channel should strive for a pumping speed of about 1 l/s. While this serves to estimate differential pumping channel dimensions, it should be noted that molecular flow conditions were assumed for this simulation, and that conditions can change for pressures approaching 100 mTorr or so.

The simulation results discussed here, in conjunction with the development results discussed in the next chapter, served to drive the mechanical design of the BECOLA beam cooler and buncher.

Chapter 5

Development of Electrode Structure and Ion Guide

A series of tests was performed with a prototype electrode assembly in order to ascertain the feasibility of the proposed electrode shape and RF and static voltage coupling scheme for operation under realistic experimental conditions. In addition, a separate ion guide device, featuring many of the same design considerations intended for the BECOLA beam cooler and buncher, was constructed and commissioned for operation with the NSCL gas stopping facility to transport ions from the 100 Torr gas cell to the 10^{-7} Torr low energy "D" line. The operational characteristics of the ion guide were studied, and the results revealed areas where design improvements might be made for the BECOLA beam cooler and buncher.

5.1 Discharge Tests

The prototype structure, shown in Figure 5.1, consists of a set of four RFQ electrodes, segmented to permit voltage gradients as illustrated in Figure 5.2, each secured to one of four RF backbone electrodes through an insulating layer of Kapton. The four RFQ + backbone subassemblies are held in place with respect to one another via a pair of Macor discs, which in turn are secured to a 13.25" CF flange by three support rods, two of which are visible in

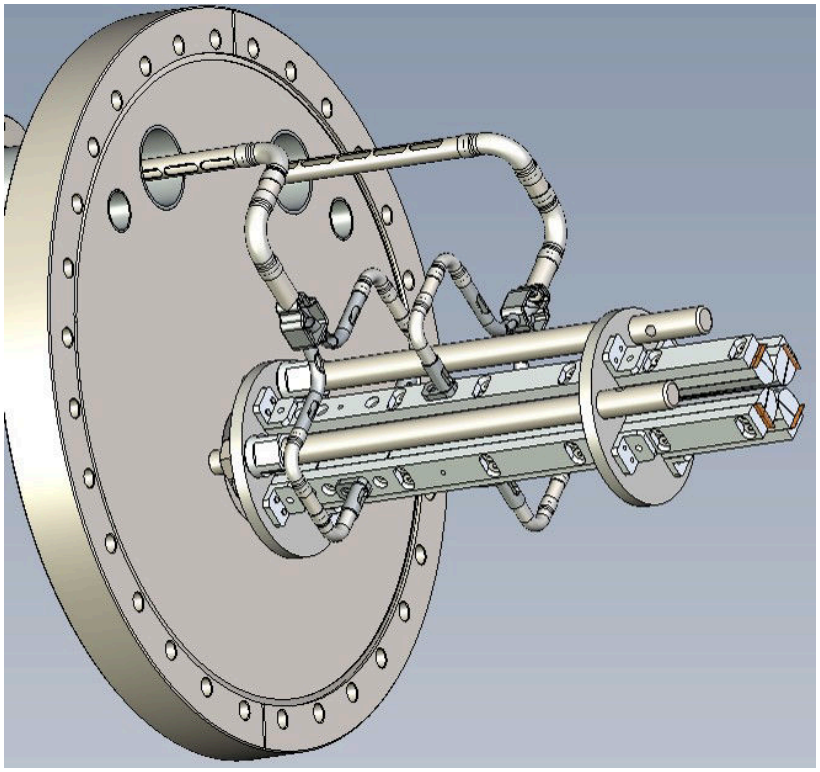

Figure 5.1: Design image of prototype electrode structure for RF discharge tests.

Figure 5.1. Opposite RF backbones are connected together via a hollow RF conductor, while leads for static voltages can be fed through the center of the RF conductor (not shown in the design image).

A series of discharge tests was performed with the prototype structure at different buffer gas pressures. The results are shown in Figures 5.3 and 5.4, and images of glow discharges at low and high pressures are shown in Figure 5.5. Figure 5.3 shows a sharp decrease in discharge voltage with a rise in pressure, similar to the behavior of systems operating at pressures lower than the Paschen minimum for static voltages for a given characteristic length [43]. For parallel plate electrodes the Paschen minimum is about 4 Torr-cm. These results suggest that, provided the cooler is operated at a pressure less than about 50 mTorr, discharge can be avoided. However, in literature the conditions for discharge are expressed in terms of pressure times distance. While doing so is straightforward in a parallel plate geometry,

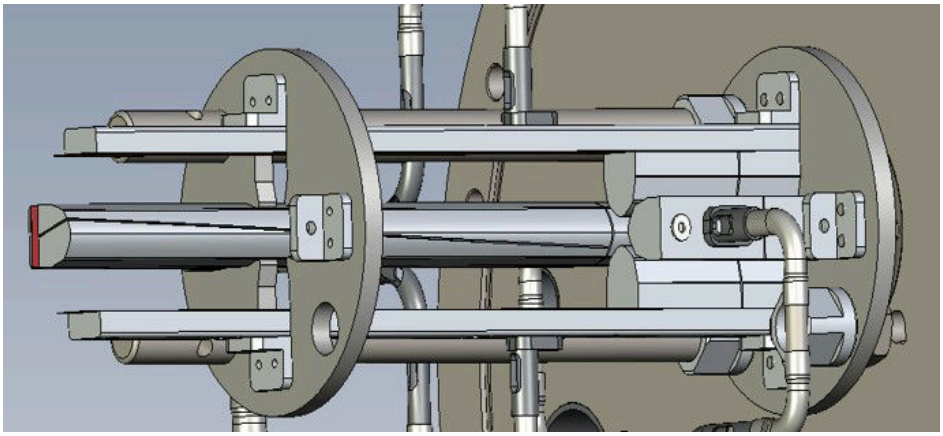

Figure 5.2: Closeup design image of prototype crosscut electrode geometry for cooler drag field.

with a more complicated setup such as the prototype geometry there are several possible characteristic distances over which a discharge might occur, as is shown in Figure 5.5. The discharge shown in the middle image (b) takes place at a voltage of about 100 V_{pp}, at a pressure of about 2 Torr and across a distance of a few cm. The pressures and distances involved are consistent with the literature discharge minimum of 4 Torr-cm. In the image on the right (c), the discharge takes place at a higher RF amplitude of about 1.5 kV_{pp} and a lower pressure of about 55 mTorr, and spans a longer distance, about 15 cm, from the RFQ electrodes to the chamber wall than that in the middle image. The results suggest that, if the distance over which a discharge can be constrained such that discharges over long distances cannot occur, the operating pressure might be pushed higher than what was possible in the prototype tests.

In addition to RF discharge studies, static voltages were applied to the RFQ segments intended to supply the drag field to verify their ability to hold voltage. The results are shown in Figure 5.4. If typical operational drag fields of order 1 V/cm are required, then a maximum voltage of 100 V will be applied. Even at the highest pressure, discharge voltages well exceed the voltages needed to produce drag fields for ion motion through the buffer gas.

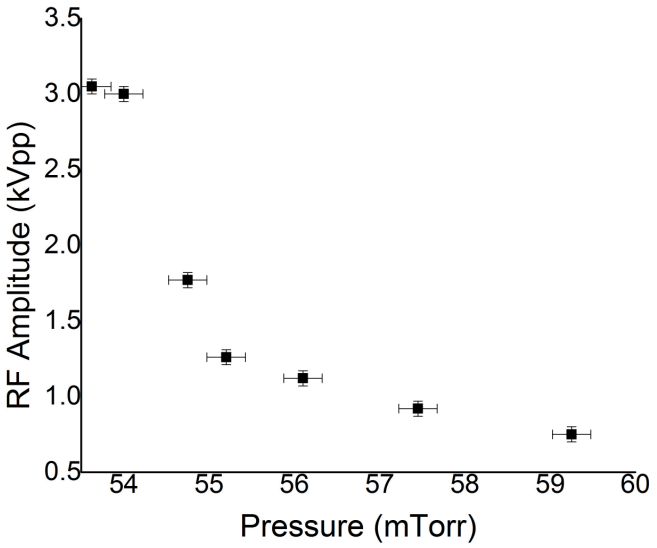

Figure 5.3: RF discharge voltages as a function of buffer gas pressure. RF was operated at 5.7 MHz.

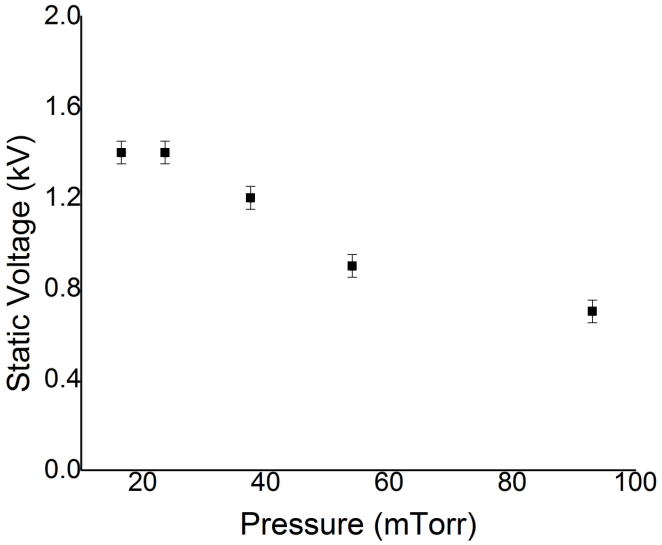

Figure 5.4: Static discharge voltage as a function of buffer gas pressure. Bias was applied to one segment of the drag field electrode as depicted in Figure 5.2, while the complement, the other segments and the backbone were held at ground.

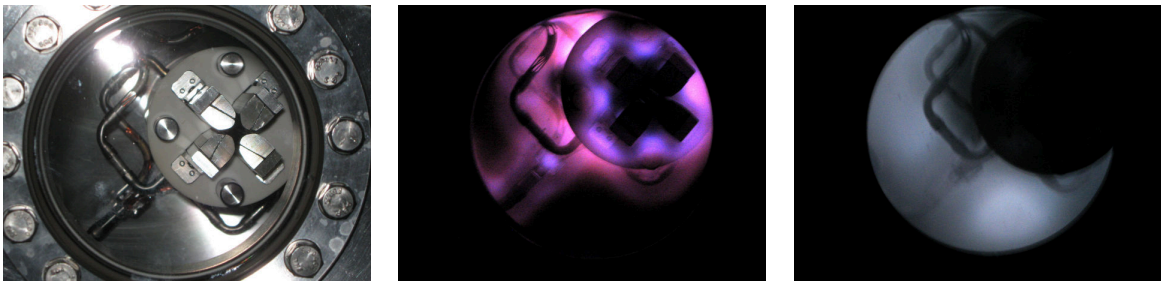

(a) (b) (c)

Figure 5.5: Left (a): Prototype electrode structure inside vacuum chamber, bottom view. RF leads protrude from the side of the electrodes. Middle (b): Image of RF induced discharge in a helium buffer gas pressure of about 2 Torr. Right (c): Glow discharge at a pressure of about 55 mTorr.

5.2 Ion Guide as Cooler and Buncher Prototype: Commissioning Studies

In addition to the discharge tests performed with the prototype structure, an RFQ based ion guide was developed as part of an upgrade to the NSCL gas stopping facility (see Figures 5.6 and 5.7). As part of the ion guide development, many of the design concepts intended for the BECOLA beam cooler and buncher discussed in Chapter 3, including drag field crosscut geometry, RF and static voltage coupling scheme, and differential pumping were implemented in the ion guide. Thus it was possible to test the efficacy of many of these design concepts prior to putting them into practice in the BECOLA device.

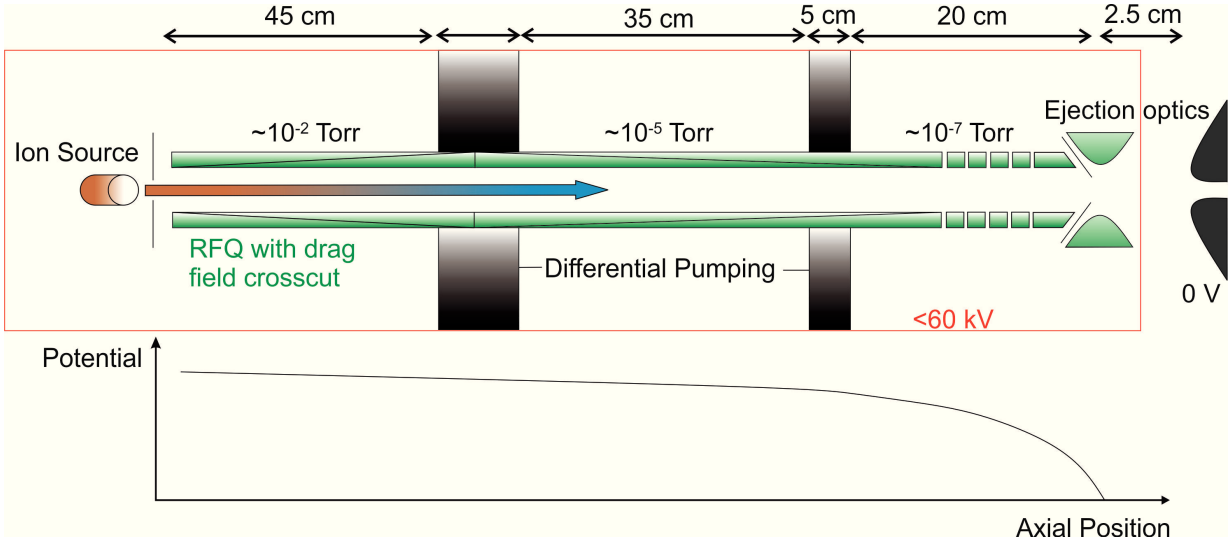

Figure 5.6: Top: Sketch of the ion guide system. Bottom: Sketch of Static potential.

The ion guide consists of three differentially pumped chambers, with a set of RFQ electrodes running the length of the system. Offline tests were conducted with a collimated potassium ion source installed at the entrance to the first set of RFQ rods. The first section is equipped with a helium inlet to allow buffer gas in, and is typically maintained at a helium pressure of few to several tens of mTorr. The RFQ electrodes run through approximately 45

cm of the high pressure region before coming to the first differential pumping section, which is about 10 cm long. The 2nd and 3rd sections of the ion guide are held, through differential pumping, at pressures of order 10^{-5} and 10^{-7} Torr, respectively. They are about 35 and 20 cm long. The whole system is held on high voltage, so that when the ions arrive at the extraction stage, they are electrostatically accelerated to a maximum beam energy of 60 keV. The commissioning studies were performed using a beam energy of 15 keV. Extracted beam currents were measured using a Faraday cup downstream of the ion guide, and upstream currents for efficiency determination were measured through pickup measurements on the first set of RFQ rods with the bias and RF turned off. Efficiency measurements as a function of RF voltage, drag field, incident current and buffer gas pressure were carried out in order to characterize the operational parameters of the ion guide.

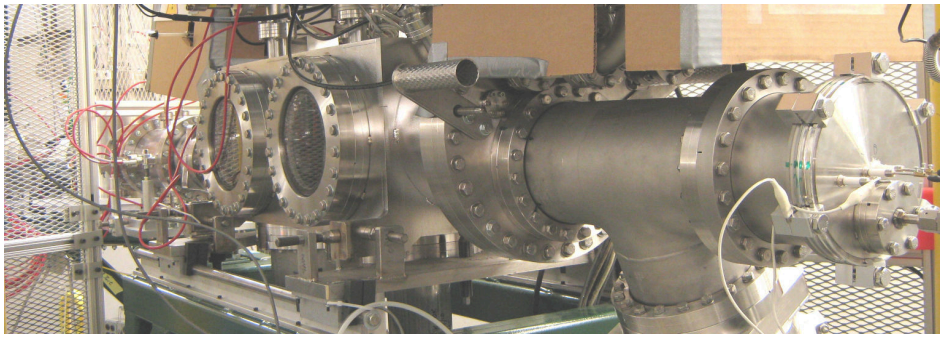

Figure 5.7: Image of the ion guide system.

A photograph of the ion guide is shown in Figure 5.7. The ion source is mounted on the flange with the insulated feedthroughs on the right. The ions travel through the 3 differential pumping stages of the ion guide, the 2nd and 3rd of which are indicated by vacuum flange windows. The ion guide system is enclosed in a protective cage, visible in the photograph on the left, and floated on high voltage to allow electrostatic acceleration of ions upon exit.

Ion guide transmission as a function of RF amplitude was measured, and the results are presented in Figure 5.8. RF was run at a frequency of 3 MHz, with an incident current of 3-5

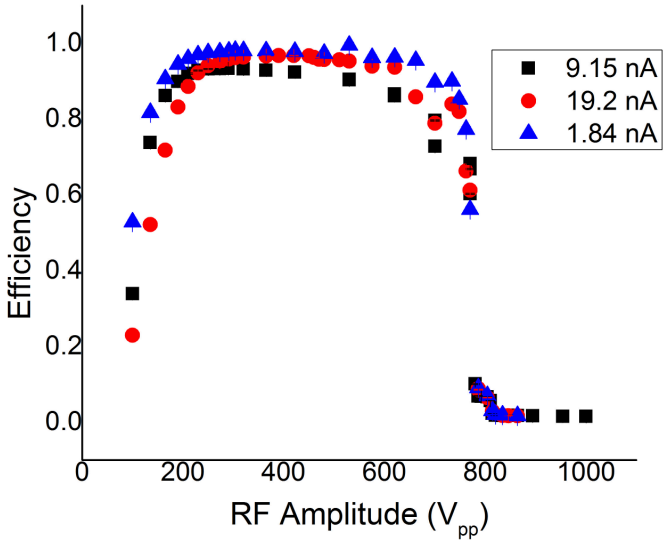

Figure 5.8: Ion guide transmission as a function of RF amplitude. Error bars are smaller than displayed points.

nA and a pressure in the high pressure region of 24 mTorr. High transmission is demonstrated for a large range of RF amplitudes. At the low end, the transmission falls of rapidly for lower voltage below about 165 V_{pp}. This corresponds to an effective pseudopotential depth of about 4.3 V for a mass 39 beam, suggesting that smaller pseudopotentials are not effective for transporting beam from the ion source. At high amplitudes the transmission efficiency decreases rapidly above 785 V_{pp}, corresponding to a stability parameter q of about 0.89 for a mass 39 beam, in close agreement with the predicted cutoff value of 0.9. Due to the $^{1}/_{\text{mass}}$ dependence of the stability parameter, even above the cutoff value for mass 39 ions, higher mass ions should still be transported. The data in Figure 5.8 show a ridge of about 7% efficiency from 785 to about 815 V_{pp}, consistent with the expected natural abundance and cutoff value for ^{41}K. Residual transmission for higher amplitudes is likely due to heavier alkali ions such as rubidium or cesium. Measurements performed with different incident ion currents show that higher currents are somewhat more sensitive to high stability parameters

(high RF cutoff) and low pseudopotential depths (low RF cutoff), but with little sensitivity in the middle of the operational range, suggesting that space charge for currents below 20 nA is not a severe limitation.

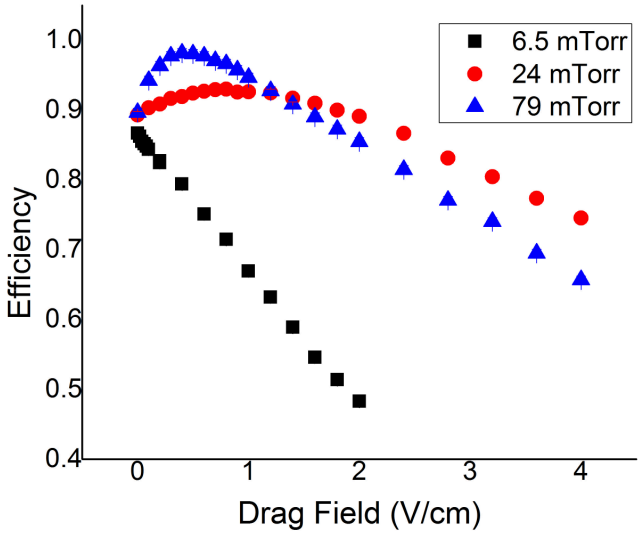

Figure 5.9: Plot of transport efficiency as a function of ion guide drag field in the high pressure region. Error bars are smaller than the displayed points.

Efficiency measurements as a function of drag field were also performed. The drag field was applied only in the high pressure region, after which the ions drifted in a constant potential in the comparatively lower pressure sections downstream. The results of these measurements are plotted in Figure 5.9. Higher buffer gas pressure serves to enhance ion guide performance by quickly damping transverse ion motion as the ions enter the RFQ structure so as to minimize collisions with the electrodes. The decrease in efficiency for higher drag fields can be explained by considering that, since the drag field is applied by a crosscut geometry, sufficiently large voltages result in a transverse octupole potential which can perturb ion trajectories. The results show, however, that it is possible to operate the ion guide at low drag field and still attain efficient ion transport.

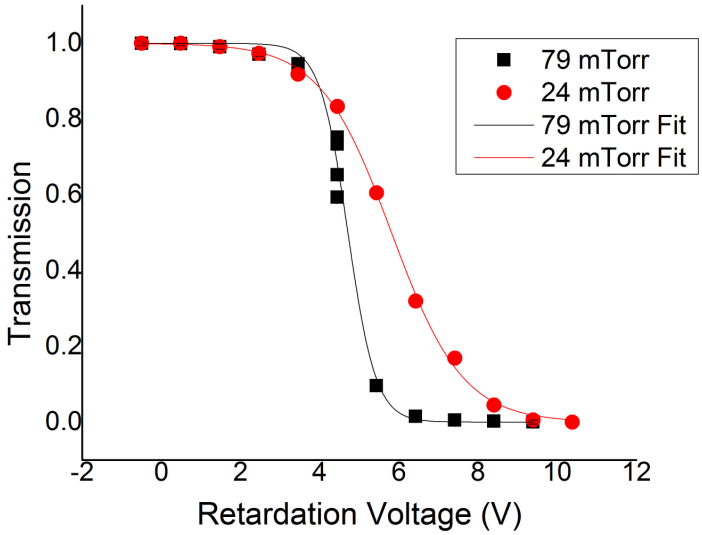

Figure 5.10: Transmission efficiency as a function of retardation voltage for different buffer gas pressures. Error bars are smaller than the displayed points.

In addition to transmission efficiency measurements, a series of measurements with retardation voltages were performed as a means of accessing the energy spread of the ions out of the high buffer gas pressure region. The ions were sent through the high pressure region, while the potential after the first differential pumping channel was held constant, apart from the one segment voltage raised to apply the retardation voltage. The transmission efficiency, referenced to the flat potential case, was measured as a function of the retardation voltage. The results for different pressures are shown in Figure 5.10. The width of the transition from complete transmission to zero transmission can be used to determine the energy spread of the beam. The data were fit to a Fermi-Dirac type function of the form $f(V) = (1 + e^{\frac{V-V_0}{w}})^{-1}$ in order to extract the widths. The widths as a function of pressure are shown in Figure 5.11. The results suggest that beams passing through a higher pressure are more thoroughly cooled, which is consistent with expectation.

A similar retardation voltage study was performed for different incident currents at an

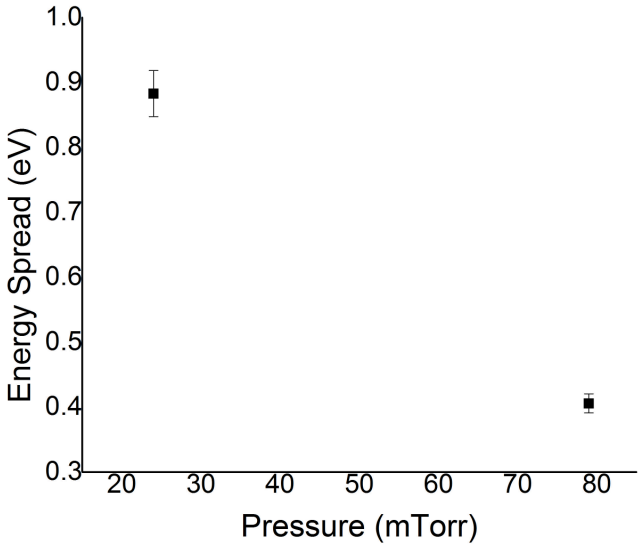

Figure 5.11: Plot of the ion beam energy spread for different buffer gas pressures.

upstream pressure of 24 mTorr. The results are shown in Figure 5.12. The widths of the transition from 100% to 0% transmission, derived from a similar fit routine as the previous study, are shown in Figure 5.13. The results indicate that any space charge due to increased current has little effect on the energy spread of the beam for currents under 20 nA.

Table 5.1 shows an optimized set of parameters based on the results of ion guide characterization measurements. Note that different RF parameters may be necessary for different ion masses. Transmission after the ion guide can be improved by operating the ion guide at a higher voltage than was used for the characterization measurements. In the case of the ion guide operating in conjunction with the gas cell, the upstream pressure will be determined by the pressure of the gas cell itself.

The results of the simulations in Chapter 4 and the developmental experiments presented in this chapter influenced the design of the BECOLA beam cooler and buncher, the details of which will be presented in the following chapter, along with commissioning results.

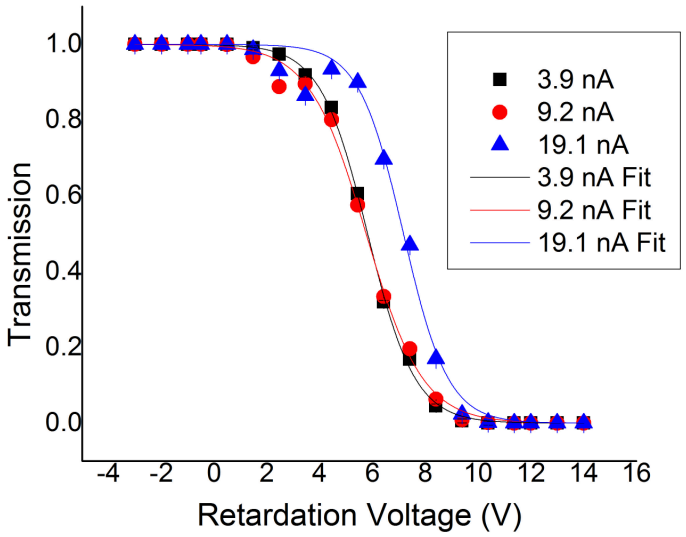

Figure 5.12: Transmission efficiency as a function of retardation voltage for different incident beam currents. Error bars are smaller than the displayed points. Pressure in the upstream portion of the ion guide was 24 mTorr.

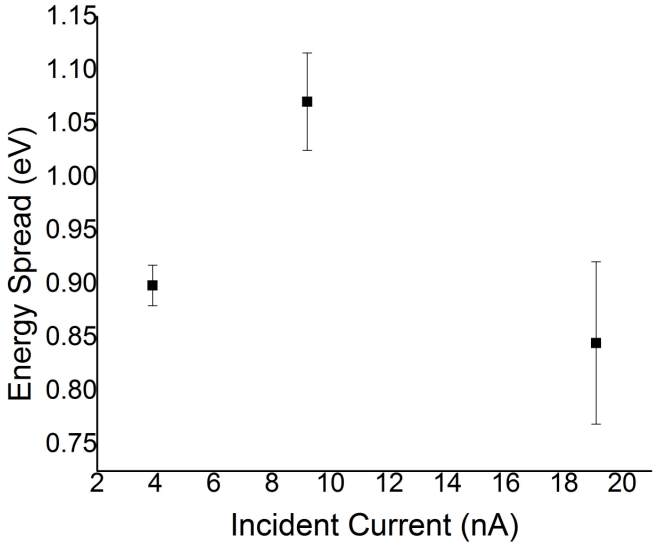

Figure 5.13: Plot of the beam energy spread for different incident currents.

Parameter	**Value**
Beam Mass	39 amu
Ion Charge	+1
High Voltage	15 kV
Hyperboloid Voltage	-1 kV
Cone Voltage	-1 kV
Drag Field	0.5 V/cm
RF Frequency	3 MHz
RF Amplitude	200 V
Upstream Pressure	80 mTorr

Table 5.1: Optimized parameters for ion guide operation based on ion guide characterization studies.

Chapter 6

The Beam Cooler and Buncher for Collinear Laser Spectroscopy

6.1 BECOLA Overview

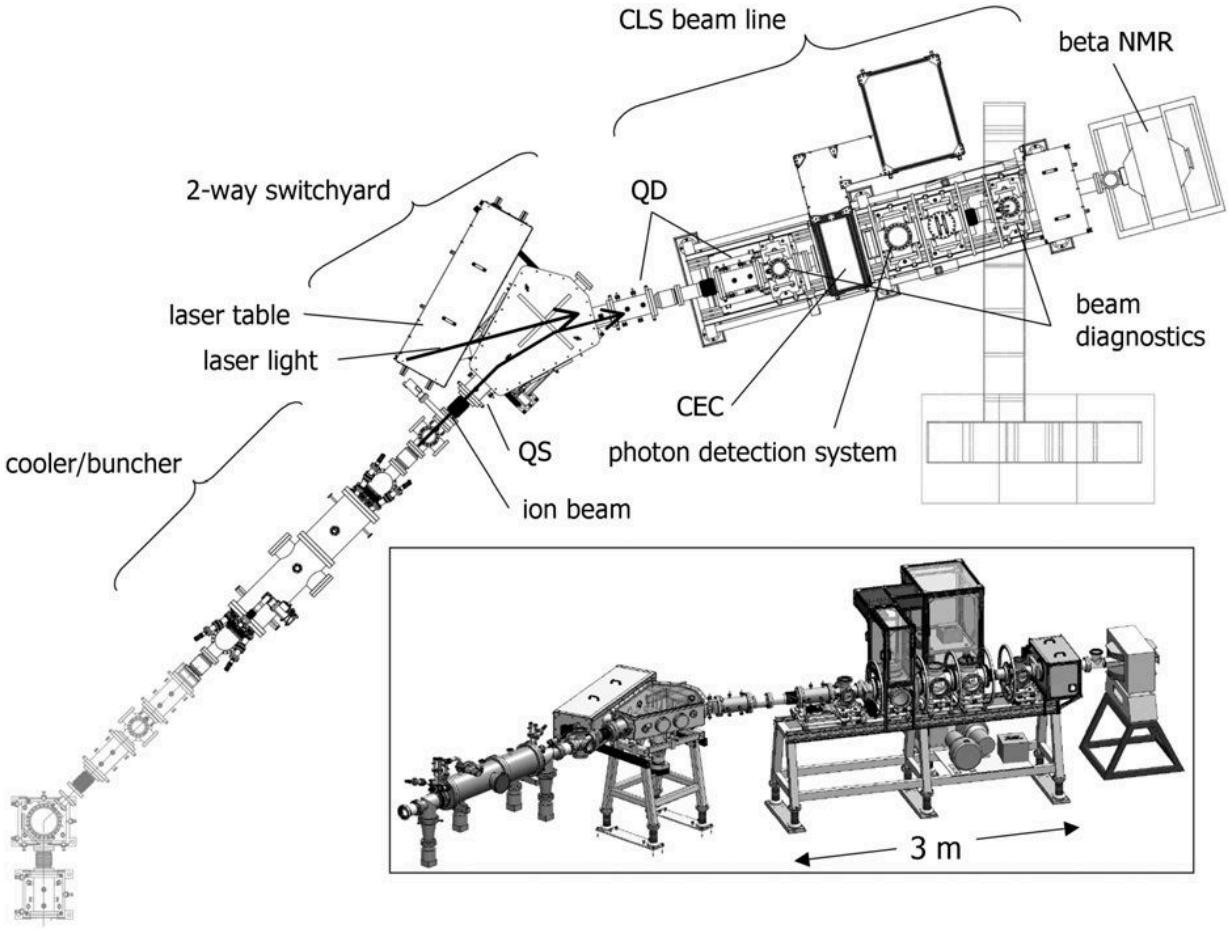

Figure 6.1: Layout of the BECOLA facility [16].

A drawing of the BECOLA facility [16] is shown in Figure 6.1. Downstream of the cooler and buncher, the beam travels through a switchyard, where the beam is bent toward the collinear laser beamline and the laser is introduced to propagate along the beam path. At the entrance to the switchyard is an electrostatic quadrupole singlet which is normally used to vertically focus the beam as it enters the switchyard, but which also can be used as a variable ion optical lens in the transverse emittance measurements. After the switchyard, the main components of the collinear beamline, apart from beamline optics and diagnostics, are the alkali vapor charge exchange cell and photon counting region. The charge exchange cell serves to neutralize the incident ion beam through collisions with a vapor of alkali metal atoms. Thus spectroscopy measurements of either the neutral atom or ion are possible. The photon counting region consists of an ellipsoidal reflector, positioned such that the beam passes through one focus of the ellipsoid, with the surface of a photomultiplier tube or waveguide positioned at the other focus in order to maximize photon collection efficiency. The charge exchange cell and ellipsoidal reflector sit on a local high voltage platform, and the bias of this platform is scanned during the spectroscopy measurement. As the high voltage platform bias is adjusted, the beam velocity is accordingly accelerated or decelerated, thus changing the effective Doppler shift of the laser light seen by the atom or ion beam and moving the beam into and out of resonance with the laser light for a given transition. Fluorescence photons are counted as a function of scan voltage to obtain a spectrum.

6.2 Beam Cooler and Buncher Overview

The design for the BECOLA beam cooler and buncher used the results of the simulations and development work presented in the previous two chapters to determine the specific

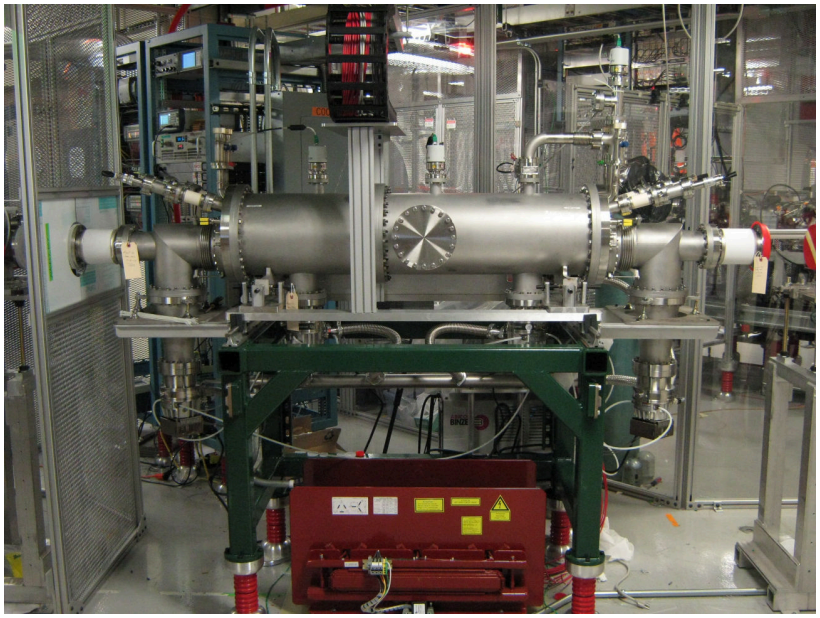

Figure 6.2: Photograph of assembled beam cooler and buncher. Beam enters from the right.

design characteristics necessary for the cooler and buncher to efficiently accept beam from the gas stopping facility and deliver pulsed, low energy spread beams to the collinear laser spectroscopy beamline. A description of the design concepts laid out in Chapter 3, informed by experience from simulation and development work, will be discussed, along with the results of commissioning studies undertaken to evaluate the performance of the cooler and buncher. A photograph of the assembled beam cooler and buncher is shown in Figure 6.2

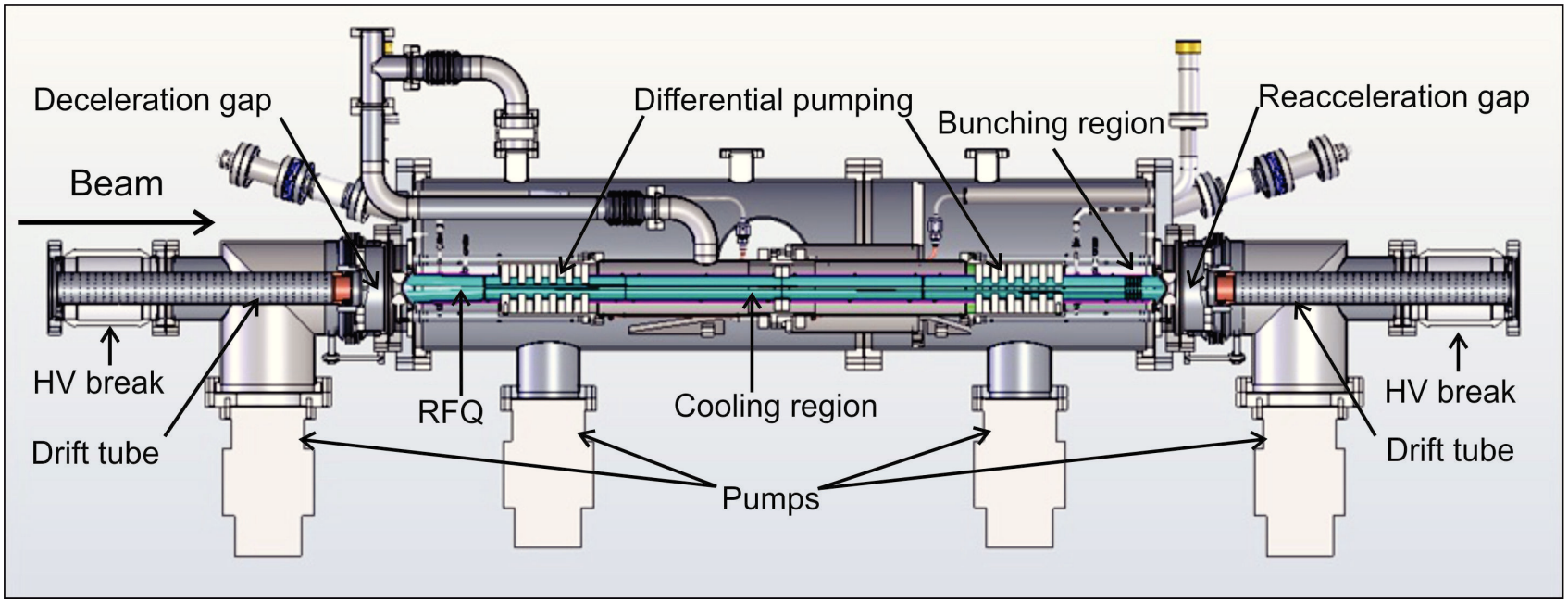

Figure 6.3: Lateral cross-section view of BECOLA beam cooler and buncher design. The cutaway view shows the RFQ electrodes (teal) extending the length of the interior, with stacks of Macor discs forming the differential pumping channels.

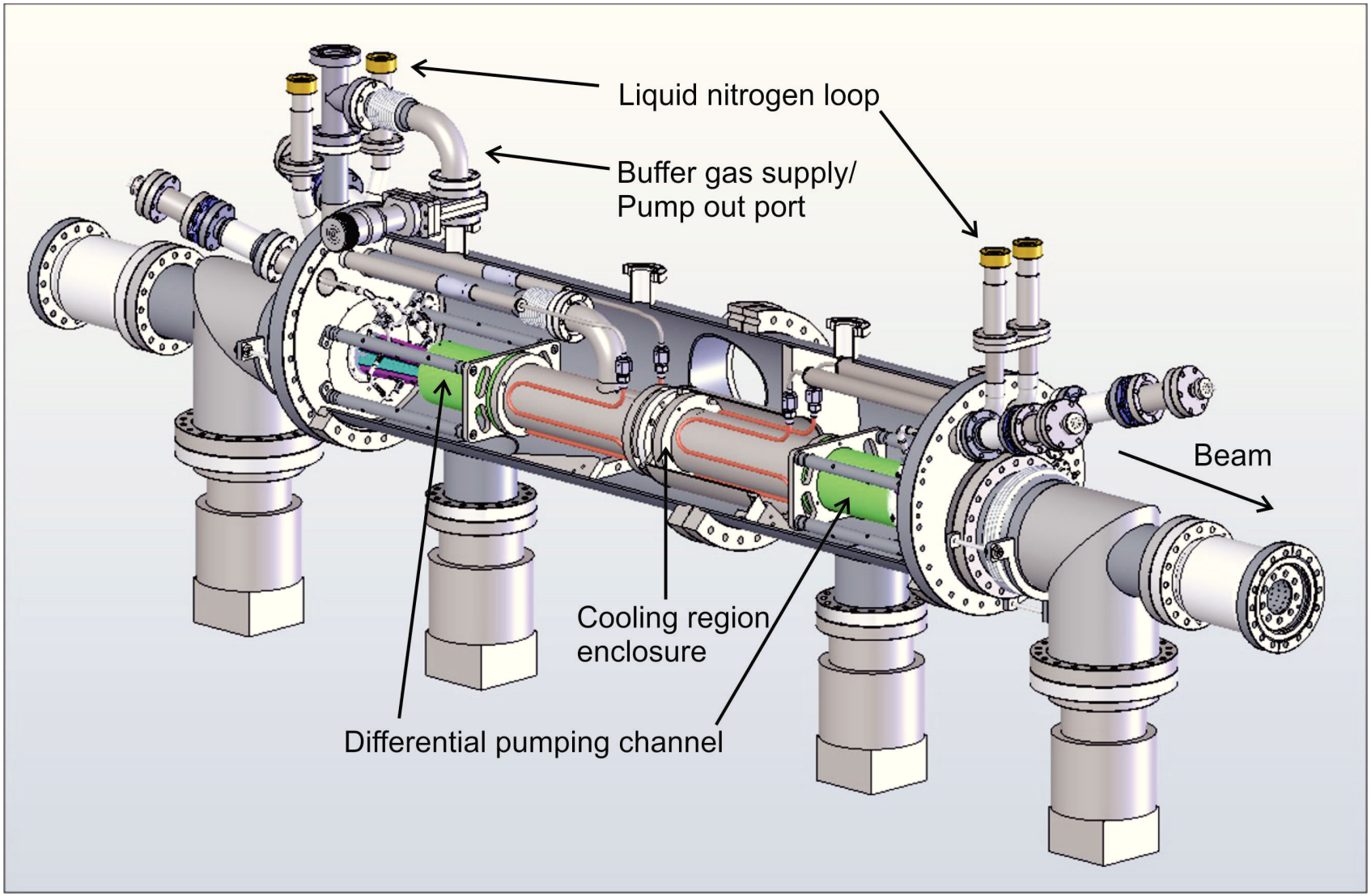

Figure 6.4: Design image of BECOLA beam cooler and buncher. The vacuum chamber interior view shows the exterior of differential pumping channel and cooling region.

6.2.1 Mechanical Systems

Design views of the beam cooler and buncher can be found in Figures 6.3 and 6.4. The beam cooler and buncher is separated from the upstream and downstream beamlines by a pair of insulating high voltage breaks, permitting the application of a high voltage bias to the entire beam cooler and buncher while neighboring sections of beamline remain at ground potential. Between the two high voltage breaks, the beam cooler and buncher consists of a drift region, a deceleration gap, the upstream and downstream halves of the RFQ structure, the reacceleration region, and a downstream drift. At the upstream (left) side, a hollow perforated tube is attached to a flange held at ground potential, and runs through the center of the high voltage break, through a custom tee fitting with bellows, and connects to an endcap electrode on the right.

A gap between the grounded endcap electrode and a hyperbolic ring on high voltage (see Figure 6.5) defines the deceleration region, where the beam is electrostatically decelerated by the high voltage bias applied to the whole beam cooler as it enters the first section of RFQ electrodes. Based on the results of acceptance simulations, the first set of RFQ electrodes was flared out to an angle of 2°, and are about 12 cm in length (see Figures 6.6 and 6.7). As with the ion guide, the electrode segments are mounted to one of four RF backbone electrodes, while the four electrode + backbone assemblies are held in place with respect to one another by Macor discs. One such disc is visible at the end of the RFQ structure in Figure 6.6, and a stack of Macor discs also forms the differential pumping channel (see Figure 6.3). The same crosscut electrode geometry described in previous chapters is employed in the cooling region of the cooler and buncher to provide the necessary longitudinal drag field.

The downstream RFQ assembly shares many of the same features as the upstream half.

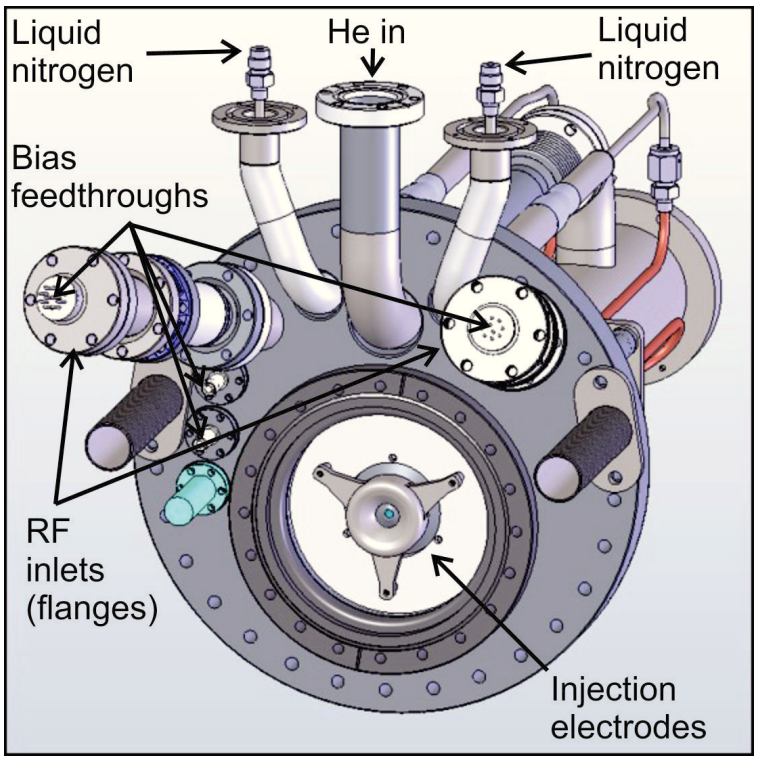

Figure 6.5: Design image of injection optics. The ejection side is similar, though it lacks the buffer gas (He) inlet.

The most important difference is the fine segmentation at the downstream end (Figure 6.10). Four segments, 5 mm in length, permit the formation of the longitudinal trap for beam bunching. Otherwise, the downstream half features a similar scheme for mounting the RFQ rods and forming the differential pumping channel. The downstream coldhead lacks a buffer gas inlet, since only one inlet is necessary and is already present in the upstream design. The ejection optics are also similar in shape, position and mounting scheme to their injection counterparts. Downstream of the reacceleration gap is another drift region nearly identical in form and function to the upstream version, consisting of a custom tee with bellows, perforated tube and high voltage break all similar to those found on the upstream side. For further description of the mechanical design of the beam cooler and buncher, the reader is referred to Appendix C.

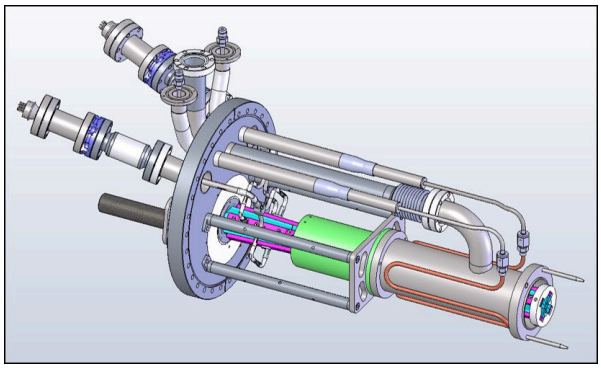

(a)

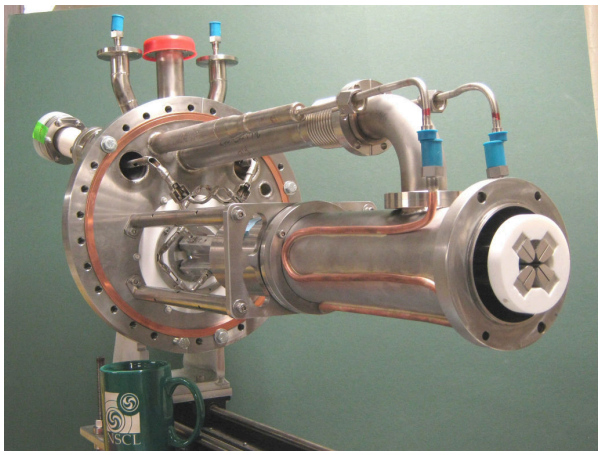

(b)

Figure 6.6: Left (a): Design image of injection stage of BECOLA beam cooler and buncher. Right (b): Photograph of beam cooler injection stage, including cooler, 1st differential pumping channel, and cryogenic cooling loop.

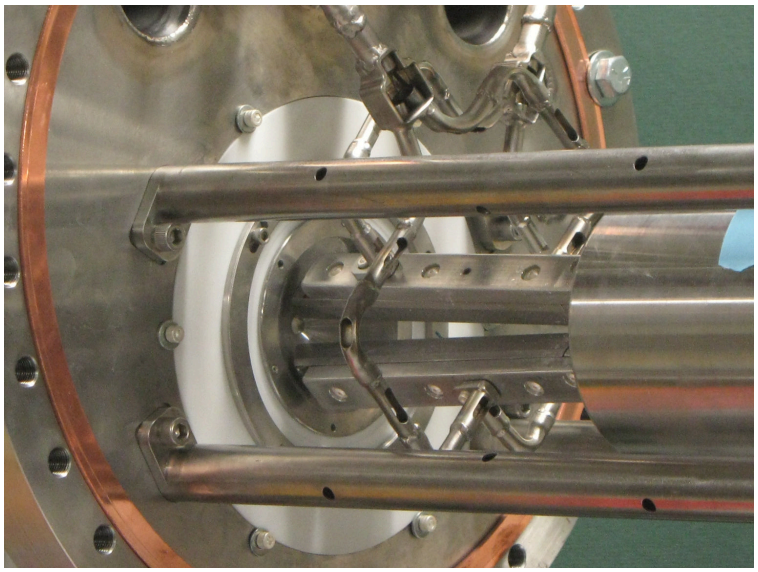

Figure 6.7: Photograph of beam cooler injection electrodes. The injection cone electrode sits immediately upstream of the flared RFQ rods, and the RF conductors can be seen connecting opposite backbone electrodes together.

6.2.2 Electrical Systems

The main electrical system of the beam cooler and buncher consists of the RFQ electrode and backbone subassembly, and the associated connections to supply the relevant voltages. A partially assembled RFQ + backbone can be seen in Figure 6.8. The RFQ electrodes are cut into wedges to provide the drag field, and are secured to the backbone underneath by screws and insulating washers. An insulating layer of Kapton separates the RFQ electrodes and backbone, and the wedge halves are held apart by sets of ceramic dowels. The RFQ electrodes are shaped to have a hyperbolic cross section in order to provide a quadrupole field as discussed in Chapter 2. The distance from electrode tip to beam axis r_0 (see Equation 2.2) was chosen to be 3.5 mm, as this same spacing was demonstrated to perform well in the prototype and ion guide tests.

Once the four RFQ + backbone assemblies are in place with respect to one another (see Figure 6.11), the RF and static voltage connections can be made. The RF signal is transmitted to the backbone electrode through a vented hollow tube which connects opposite backbones to the same RF phase in a pincer-like configuration (see Figure 6.7). The RF conductor extends from the backbone electrodes toward the mounting flange, through a high voltage break and is connected to a grooved flange, which is electrically isolated from the main vacuum chamber, via three setscrews (see Figure 6.12). The bias leads for individual RFQ segments run through the center of the RF conductor, and are connected to the individual RFQ segments through a setscrew and standoff assembly (Figure 6.10), isolated from the backbone by insulating washers. At the vacuum-air interface, individual voltage channels are connected to the feedthroughs in the center of the flange, while the RF is carried on the flange itself and the exterior of the plug on the air side.

On the air side, the RF is supplied to the flange through a tuned LC circuit, as illustrated in Figure 6.13. An RF amplifier sends the signal through an impedance matching transmission line transformer [44]. The output terminals are connected to nearly identical inductances, which are connected one each to the 2.75" flanges, with a tunable capacitor in parallel. The RFQ and tuning capacitor thus form the capacitive load to a resonant LC circuit. The RF voltages at adjacent backbones are equal in amplitude and opposite in phase, resulting in the desired quadrupole field in the RFQ region. The upstream and downstream RFQ sections are driven independently, and thus each has its own tuning circuit. This permits the flexibility to drive the upstream and downstream sections at different frequencies and amplitudes. The bias voltage leads, as with the RF conductor in the vacuum chamber, are run through the center of the inductors between the power supply and feedthrough in order to decouple the RF from the static voltage power supply output. A more detailed description of the RF circuitry is given in Appendix A.

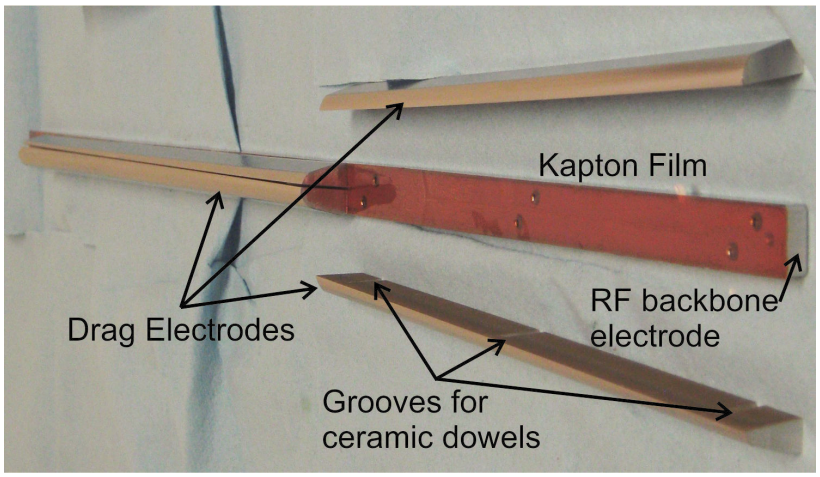

Figure 6.8: Photograph of partially assembled drag field electrode and RF backbone substructure.

Figure 6.9: Photograph of buncher electrodes, with pen for scale.

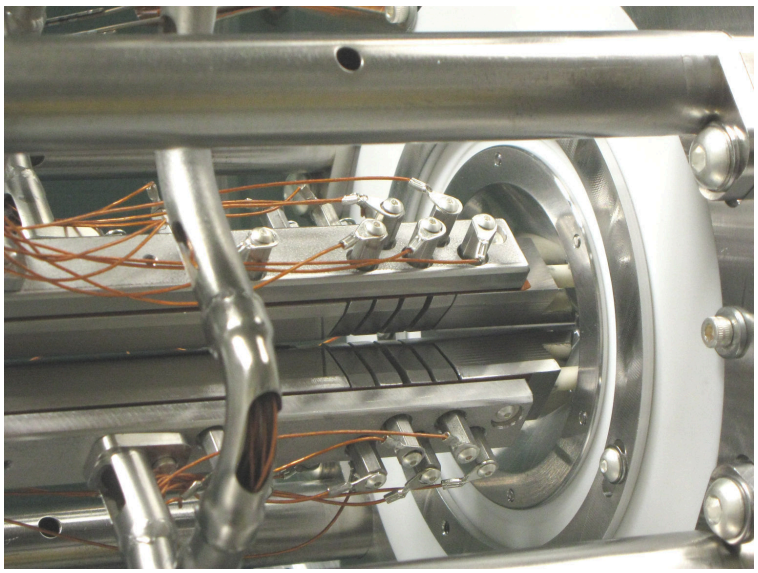

Figure 6.10: Photograph of buncher electrodes

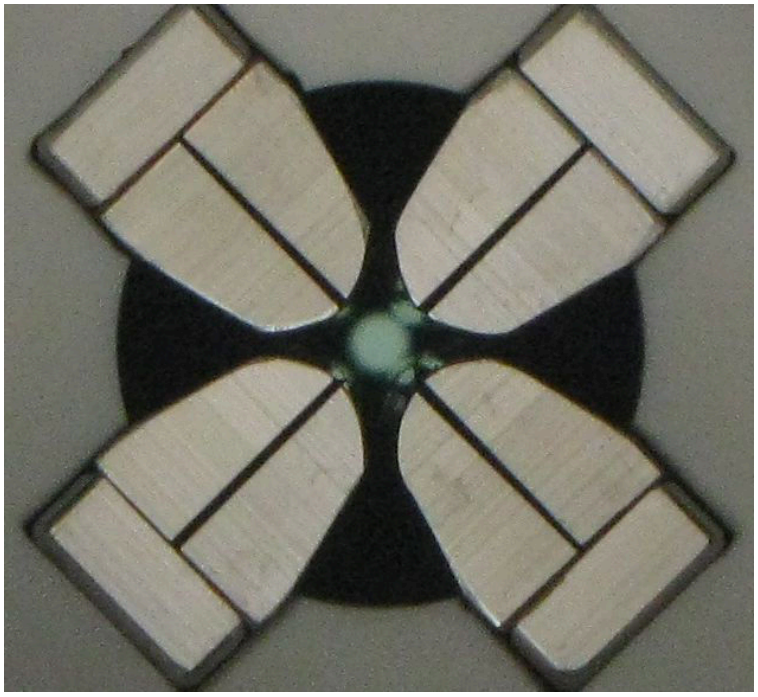

Figure 6.11: Photograph of RFQ electrode cross section. A Macor disc frames the exterior, and the hole in the center of the extraction cone can be seen through the center of the RFQ in green.

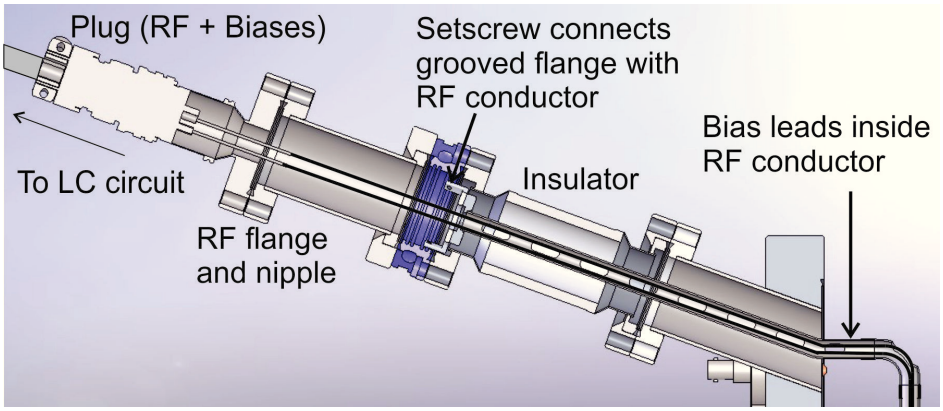

Figure 6.12: Design image of the vacuum-air interface for the RF and bias voltage circuitry.

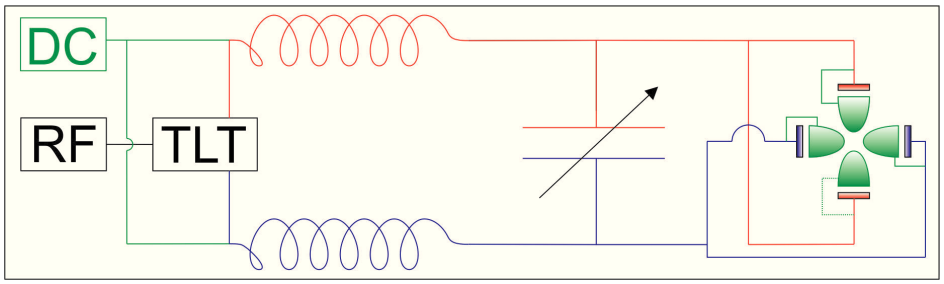

Figure 6.13: Sketch of the circuit which supplies RF and static voltages to RFQ electrodes. Red and blue indicate opposite RF phases, and static voltage connections are depicted in green. The transmission line transformer (TLT) matches the output impedance of the RF amplifier to the resonant load impedance.

6.3 Commissioning Measurements

Measurements of beam transmission efficiency, transverse emittance, time spread and energy spread were performed to commission the BECOLA beam cooler and buncher. An online collinear laser spectroscopy experiment was also performed to demonstrate the readiness of the BECOLA facility, with the newly completed beam cooler and buncher, for collinear laser spectroscopy measurements of rare isotope beams.

6.3.1 Efficiency Measurements

Efficiency measurements were performed using a Faraday cup upstream of the beam cooler and buncher to measure incident current, and another Faraday cup or microchannel plate (MCP) to measure downstream currents. Faraday cups were used for measuring beam currents down to the pA level, while MCPs were used for counting smaller numbers of ions per pulse, up to ∼1000 ions/bunch. More than 1000 ions/bunch would result in pulse pileup making count rates unreliable, while the Faraday cups lack the sensitivity to measure beam currents much lower than, at best, a few hundred fA, or just over 1000 particles per bunch with a kHz bunch rate. Continuous or DC beam efficiency measurements entail a straightforward comparison between incident and outgoing beam currents. For bunched beam measurements, an upstream quadrupole electrode was connected to a voltage switch to fashion a beam gate in order to restrict the number of incident ions per bunch cycle, chopping the beam. The number of incident ions per bunch could then be calculated using the duration of the beam gate in the open state and measured values of upstream current. Downstream of the buncher, for high rates, a Faraday cup was employed to measure an average current, and the number of outgoing ions per pulse was inferred from the bunch repetition rate. For low rates, the

signal from the MCP was sent to a scaler for ion counting, and the bunched beam count rates were compared to the chopped (beam gate on) but not bunched beam count rates. The MCP and Faraday cup in question were mounted to a six way cross as part of a beam observation box (BOB) located about 85 cm downstream of the exit of the beam cooler and buncher.

DC transmission efficiencies of about 80% were consistently observed when measurements were made with the Faraday cup. MCP bunched mode measurements were made relative to the chopped, unbunched rates, and were normalized to 80% to obtain an absolute bunched mode efficiency. A separate measurement was performed in which the RF was turned off, a picoammeter was connected to the first set of RFQ rods, and the current transmitted through the injection optics and into the RFQ region was measured. It was found that 80% of the beam measured at the upstream Faraday cup was picked up on the RFQ rods. Therefore, the DC efficiency is limited by the mismatch between the emittance of the incident beam and the system acceptance, but the efficiency of transport through the beam cooler and buncher is close to 100%. Efficiency uncertainties were estimated based on statistical fluctuations in Faraday cup or MCP count rates.

6.3.1.1 Efficiency versus Buffer Gas Pressure

A plot of the bunched mode efficiency as a function of buffer gas pressure in the cooler is shown in Figure 6.14. While the DC efficiency is insensitive to most parameters discussed here, it was found that the efficiency of both DC and bunched beams suffers if the pressure in the cooler is too low. The dependence of the efficiency on cooler pressure is related to the RF settings used. As was mentioned earlier in the chapter, the upstream and downstream sections are driven independently by separate RF systems. For best acceptance values, the upstream section is operated with relatively high RF frequencies and amplitudes, typically

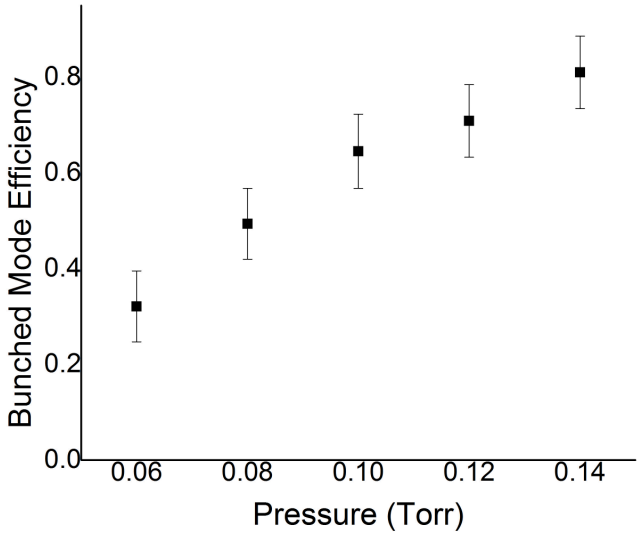

Figure 6.14: Measured bunched mode efficiency as a function of buffer gas pressure in the cooler.

around 5 MHz and 900 V_{pp}. It turns out, for applications such as collinear laser spectroscopy where small energy spread is crucial, it is beneficial to operate the downstream section with much lower RF frequencies and amplitudes, the reason for which is elaborated on in the discussion of longitudinal emittance measurement results. These and all subsequent efficiency studies, unless otherwise specified, were undertaken operating the downstream RFQ section at 1.2 MHz and 110 V_{pp}. The upstream electrodes were operated at 5 MHz and 850 V_{pp} in all efficiency measurements. However, using lower RF amplitudes necessarily means that the confining pseudopotential is weaker in the downstream section. In order to efficiently transport ions, the cooler must be operated at sufficient pressure to cool away the transverse motion of the ions before they reach the region of low RF amplitudes. The results shown in Figure 6.14 indicate an increase in efficiency up to 140 mTorr. Further increases of pressure beyond 140 mTorr did not improve the buncher efficiency. A cooler pressure of 140 mTorr results in a buncher pressure of about 1.4 mTorr due to the differential pumping scheme.

6.3.1.2 Efficiency versus Cooling Time and Ion Count

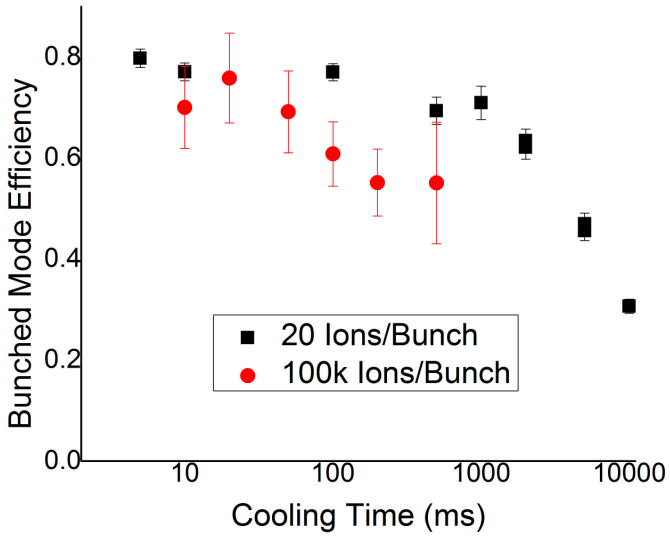

Figure 6.15: Bunched mode efficiency versus cooling time for different numbers of ions per bunch.

A set of efficiency measurements examining the effect of residency time of the ion cloud in the buncher was also undertaken, the results of which are shown in Figure 6.15. These results and those depicted in Figure 6.16 highlight some important issues regarding how the cooler and buncher should be operated for maximum efficiency. For low RF settings, buncher efficiency is sensitive to both cooling time and the number of ions in the trap. In the discussion of space charge limitations in Chapter 2, an upper limit of 3×10^7 ions in the trap was estimated using typical operating parameters. Figure 6.16 shows that the effects of space charge are already apparent well before this value is reached. Moreover, Figure 6.15 shows that the amount of time the ions can remain confined in the trap also depends on the number of ions in the trap to begin with. Using larger RF amplitudes and frequencies to produce deeper pseudopotentials does a great deal to enhance buncher efficiency for large numbers of ions per bunch. For buncher pressures of 1.4 mTorr, cooling times of a few ms

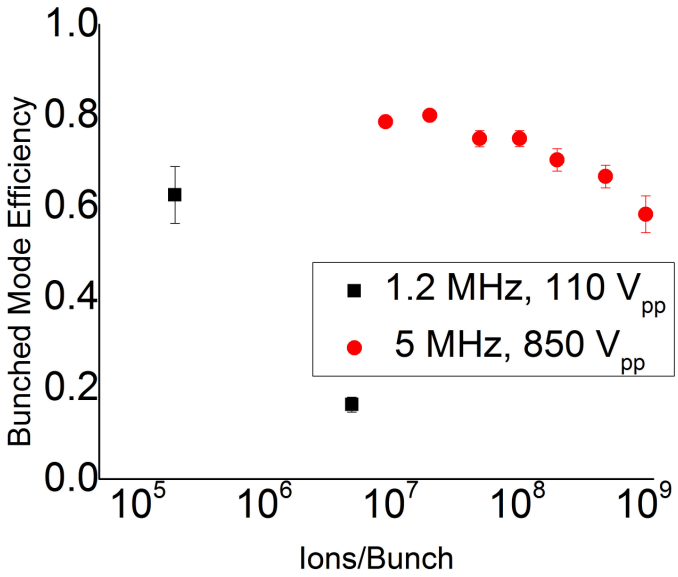

Figure 6.16: Efficiency versus incident ions per bunch. A confinement time of 10 ms was used.

are sufficient to cool the ions in the buncher. Therefore the buncher should be operated with cooling time no longer than about 5 ms at 1.4 mTorr for the ideal combination of complete cooling and minimal in-trap losses. It should be noted, however, that the low efficiency for high count rates is only an issue for offline experiments, and is unlikely to be a problem for online rare isotope measurements, where beam rates tend to be lower.

6.3.1.3 Efficiency versus Longitudinal Trap Depth

The results of efficiency measurements with respect to the depth of the longitudinal confining potential can be found in Figure 6.17. Longitudinal trap depths were calculated using a SIMION model of the buncher and experimental voltage settings. As with the simulation results discussed in Chapter 4, a SIMION potential array was used to calculate the potential on the beam axis given the buncher electrode geometry and voltage settings, and the trap depth is determined by the voltage difference between the potential well minimum and the

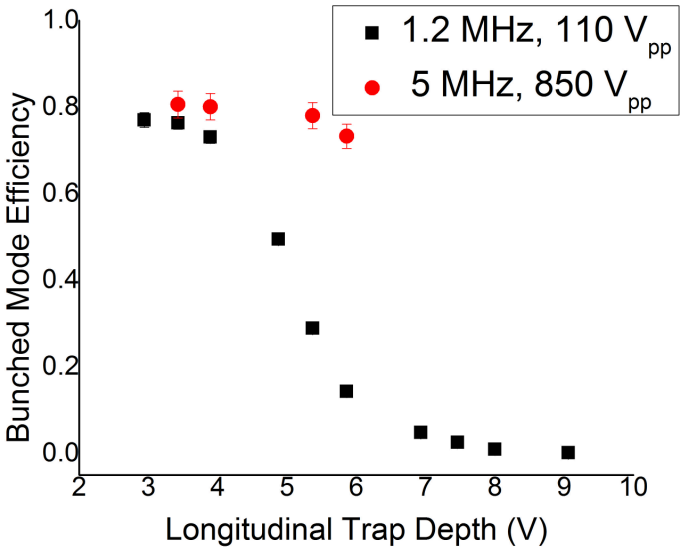

Figure 6.17: Bunched mode efficiency as a function of static voltage trap depth.

edge of the drag field at the entrance of the bunching region. The results indicate that a deeper well can actually be detrimental to buncher performance, especially for the lower RF frequencies and amplitudes. This can be understood from Equation 2.12, which shows that a deeper longitudinal trap reduces the effective transverse confinement, hence the earlier decrease in efficiency for the low RF amplitude case.

6.3.1.4 Efficiency versus Extraction Field

Figure 6.18 illustrates the results of the bunched mode efficiency measurement as a function of extraction field at the buncher trap minimum. The extraction fields were calculated by using a SIMION potential array and the experimental voltage settings using the same technique as was used in the trap depth calculation. The fields were calculated at the position where the potential minimum was when the trap was closed. A decrease in efficiency with increasing extraction field is apparent in Figure 6.18. The most likely cause is that, due to the large stability parameter value of 0.8 used for the measurements, the lateral extent of the ion cloud

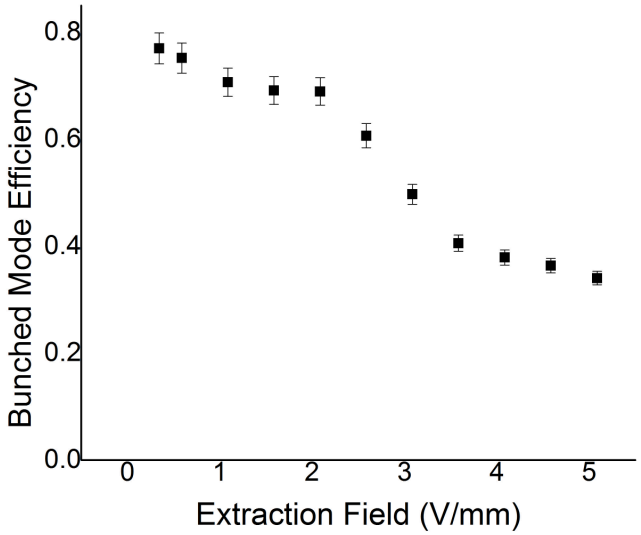

Figure 6.18: Results of efficiency measurements as a function of the extraction field at the potential minimum.

in the trap is relatively large due to microoscillation amplitudes. Therefore a larger ejection field introduces more energy to the ion bunch, which can destabilize the ions nearer the edge of the cloud.

6.3.2 Buncher Performance Studies by Collinear Laser Spectroscopy

In addition to efficiency, the time width and energy spread of outgoing bunched beam were also characterized as a function of several operating parameters. The collinear laser spectroscopy system was used to measure the time and energy spread of the bunched beam. The laser was tuned to probe the D1 transition of ^{39}K. An electronic energy level scheme for ^{39}K is shown in Figure 6.19. After the ion pulse is released from the trap, the bias on the photon counting region and charge exchange cell were scanned, and fluorescence photons were counted in a two dimensional histogram of time and bias voltage. The projections onto the time and voltage axes were fit, and the FWHM are extracted. Time of flight spectra were

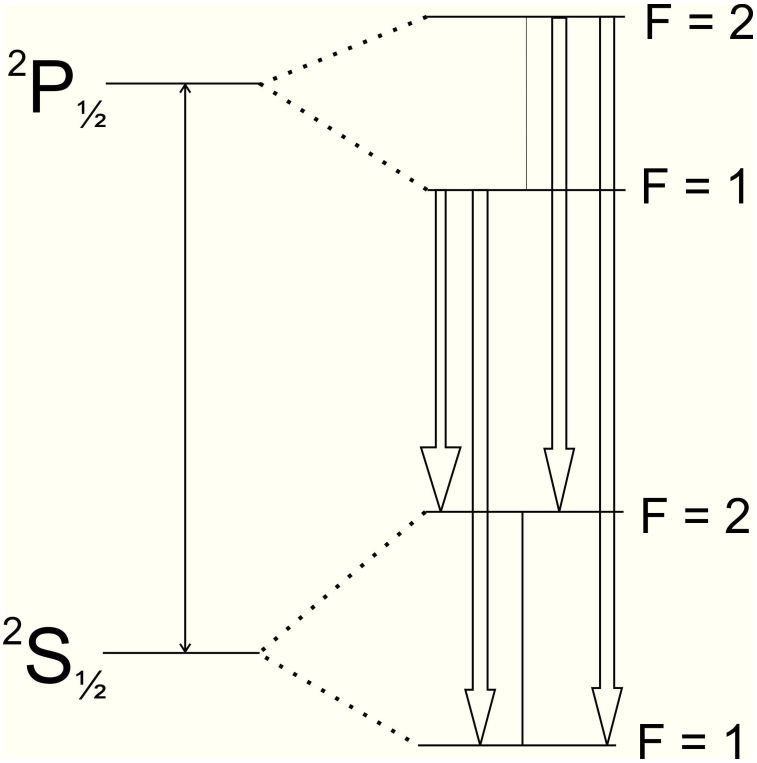

Figure 6.19: Level scheme of hyperfine levels for the D1 transition of ^{39}K [45]. Energy differences are not to scale.

fit to decaying Fermi-Dirac type functions similar to those used with the simulation data. The fluorescence spectra used to deduce the energy widths were fit to a linear combination of Lorentzian and Gaussian curves with a common mean, used to mimic a Voigt distribution, with an exponential tail to account for additional scattering in the neutralization process. Measurements as a function of extraction field, ion count per bunch and longitudinal trap depth will be presented and discussed. FWHM uncertainties were determined from standard error calculations of the fit parameters used to calculate the widths.

As was mentioned in the previous chapter, in order to perform collinear laser spectroscopy measurements it was necessary to operate the upstream and downstream sections of RFQ at different frequencies and amplitudes. Although larger amplitudes result in more efficient operation, especially when more ions per bunch are involved, the larger amplitudes distort

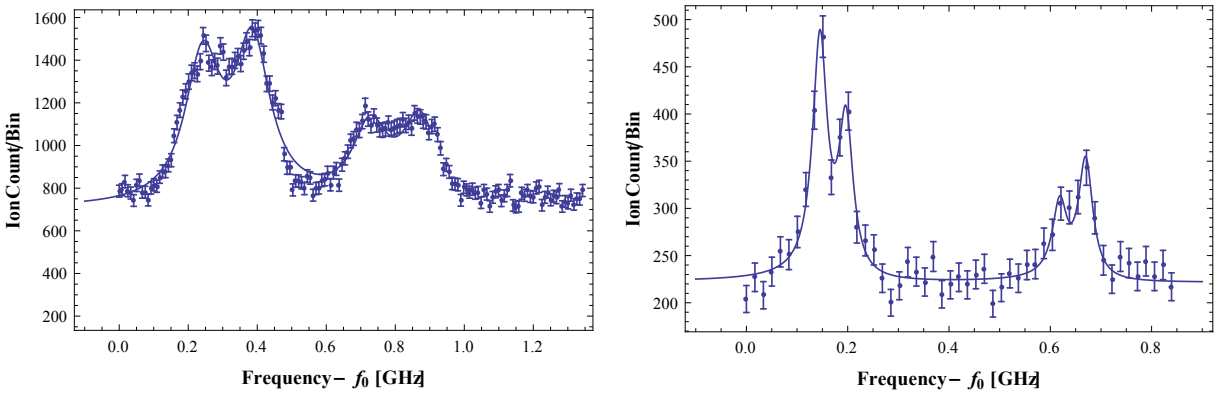

(a) (b)

Figure 6.20: Hyperfine spectrum of D1 transition of ^{39}K for two different RF settings. Left (a): Spectrum was taken using 5.3 MHz frequency and 900 V_{pp} amplitude. Right (b): Spectrum was taken using 1.2 MHz RF frequency and 110 V_{pp} amplitude.

the energy spread of the ion bunch, which is not suitable for collinear laser spectroscopy experiments. An example of RF induced energy spread distortion can be seen in Figure 6.20. The spectrum on the left was taken using an RF frequency of 5.3 MHz and an amplitude of 900 V_{pp} on the downstream side, and the spectrum on the right was taken using an RF frequency and amplitude of 1.2 MHz and 110 V_{pp}, also on the downstream portion. In both cases the upstream RFQ rods were operated at 5.3 MHz and 900 V_{pp}. The shift and broadening of the peaks in the high frequency and amplitude are readily apparent. In principle, if all electrodes are perfectly aligned, and the RF signals are tuned such that the two phases are precisely equal and opposite, and if the ions are confined near the beam axis, then a low-energy spread with high frequency and amplitude should be possible. It was found during commissioning measurements, however, that tuning the RF circuit to yield precisely matched phases and amplitudes to better than about 2° or 5% was difficult with the current design. For a 900 V_{pp} signal, a mismatch of 2° results in a potential oscillation on the beam axis of about 3.5% of the total amplitude. If the time structure of the beam is much longer than the RF period, which is usually the case, this translates to a smearing out of the ion

cloud energy, as can be seen in the left portion of Figure 6.20. For a mass 39 beam at an energy of 30 keV, an energy spread of 10 V translates to a broadened spectrum of about 85 MHz, much wider than the natural linewidth of ∼10 MHz for a hyperfine transition in ^{39}K. Distortion of the energy spread was circumvented by operating the bunching region at lower RF amplitudes, at the cost of efficiency for high ion counts.

For some cases, a series of simulations was performed using a particle-in-cell (PIC) approach [46] which, in addition to simulating the external RF and static fields, also simulates the effects of space charge. The inclusion of space charge effects results in much closer agreement with experiment than was achieved with SIMION simulations. The remaining discrepancies between the measured and simulated values likely arise from misaligned electrodes or mismatched RF amplitudes or phases, which can cause the on-axis potential to change with time, thus smearing out energy and time distributions.

6.3.2.1 Sensitivity Improvement by Beam Bunching

A comparison of bunched and unbunched fluorescence spectra is shown in Figure 6.21. The spectrum of the unbunched beam is completely obscured by background photons, while the spectrum from the bunched beam is readily apparent. The advantage of using bunched beams for experiments with low count beams is clear.

6.3.2.2 Measured Time and Energy Widths versus Ion Count per Bunch

Apart from the efficiency issues with high count rates discussed earlier, the number of ions per bunch also had an impact on the time structure of extracted ion pulses. Figures 6.22 and 6.23 show PIC simulated time of flight spectra. Figure 6.22 shows a sample of 10^5 ions per bunch, while Figure 6.23 shows an order of magnitude more, 10^6 ions per bunch. As the

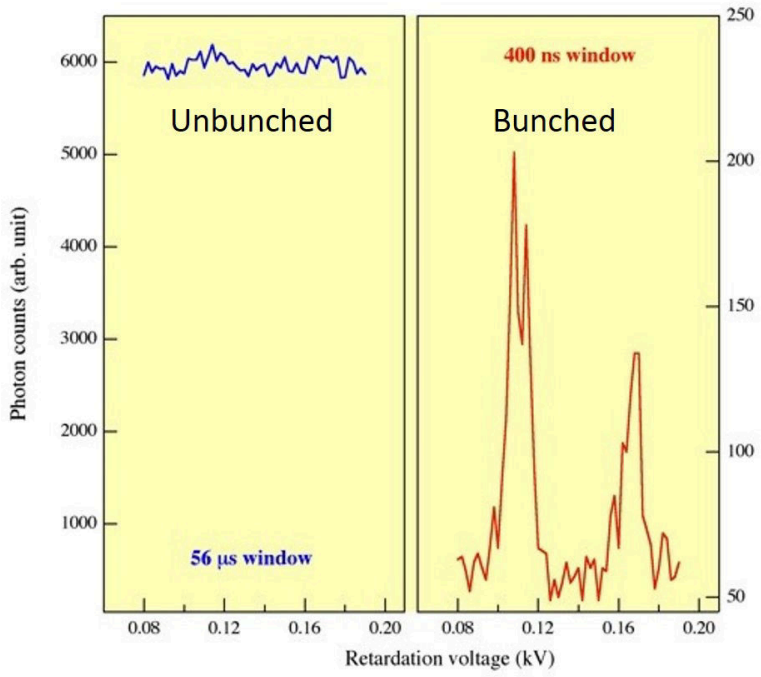

Figure 6.21: A comparison of bunched and unbunched fluorescence spectra.

trap fills up, the ion cloud extends backwards toward the differential pumping region, where the potential is much flatter. When the trap is opened, these additional ions comprise the additional time of flight peak which appears a few μs before the main peak. As the number of ions per bunch is increased, the early satellite peak grows, while the main peak stays approximately the same size.

Figures 6.24 and 6.25 show measured time of flight spectra exhibiting the same behavior as is seen in simulation. Figure 6.24 shows the results from a measurement with 10^5 ions per bunch, and Figure 6.25 shows the result of a measurement with 10^6 ions per bunch. The results show a similar emergence of an earlier time peak when the number of ions in the trap is increased. The discrepancy in absolute flight times between simulation and measurement can be attributed to the fact that in simulation, the times are recorded immediately after the ground electrode, while the measurement times are taken at the photon counting region 5 m away.

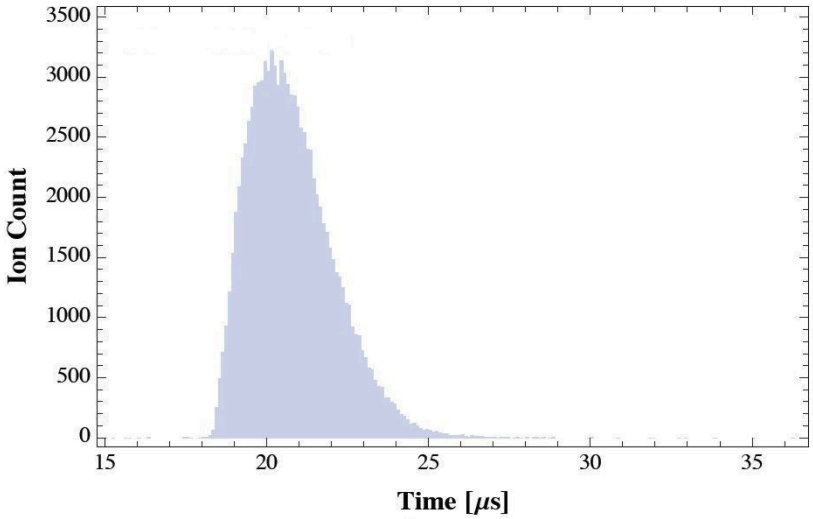

Figure 6.22: Simulated time of flight spectrum. Results were obtained using a particle in cell (PIC) code, simulating 10^5 ions ejected from the buncher.

The simulated and measured widths of the time of flight and energy distributions are plotted in Figures 6.26 and 6.27. In the high ion count case, where multiple time of flight peaks appeared, the width of the main (2nd) peak is plotted, and a cut was applied to the energy data to only fit data coincident with the 2nd time of flight peak. The increased ion count per bunch has only a modest effect on the energy spread, but broadens considerably the time width, due to the increased initial size of the ion cloud.

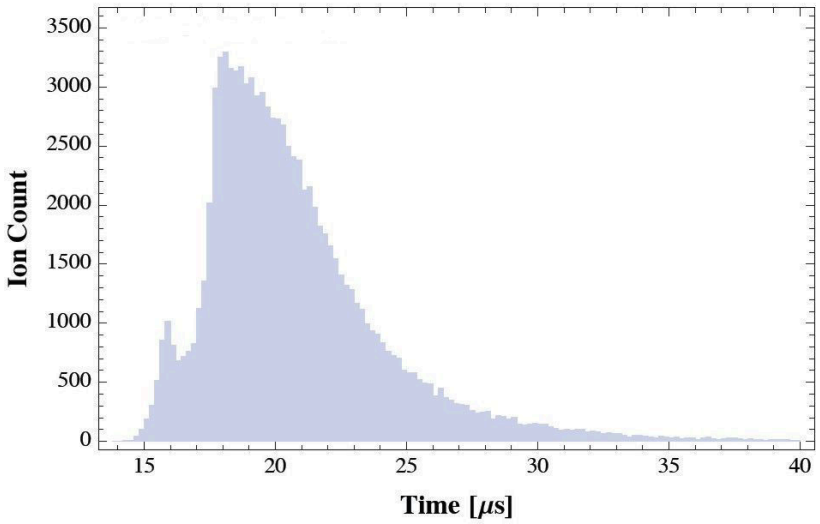

Figure 6.23: Particle in cell simulation of 10^6 bunched and ejected from the beam cooler and buncher.

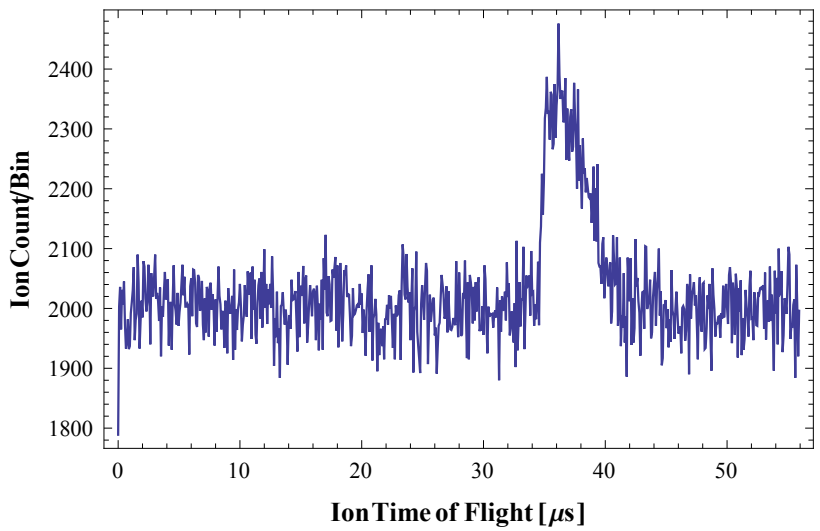

Figure 6.24: Measured time of flight spectrum of a bunched beam with 10^5 ions per bunch.

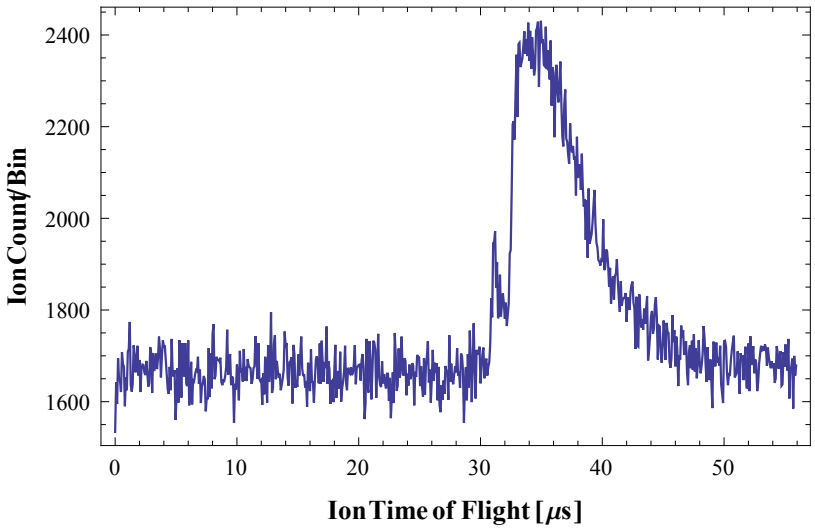

Figure 6.25: Measured time of flight spectrum of a bunched beam with 10^6 ions per bunch.

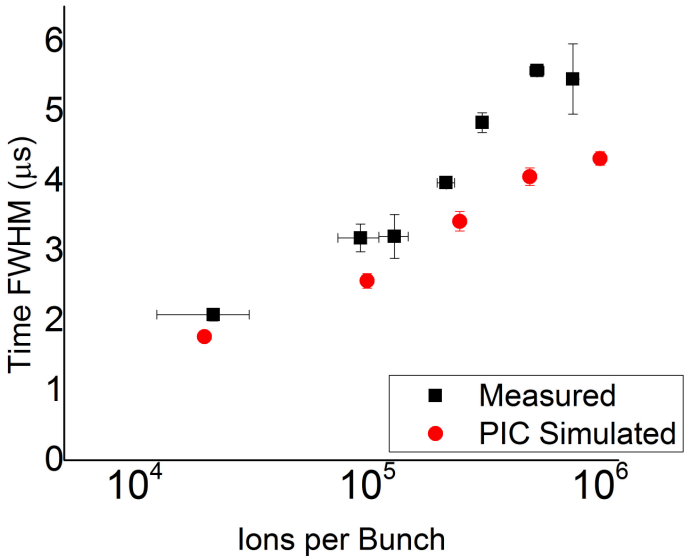

Figure 6.26: Measured time widths of bunched beams versus ion count per bunch.

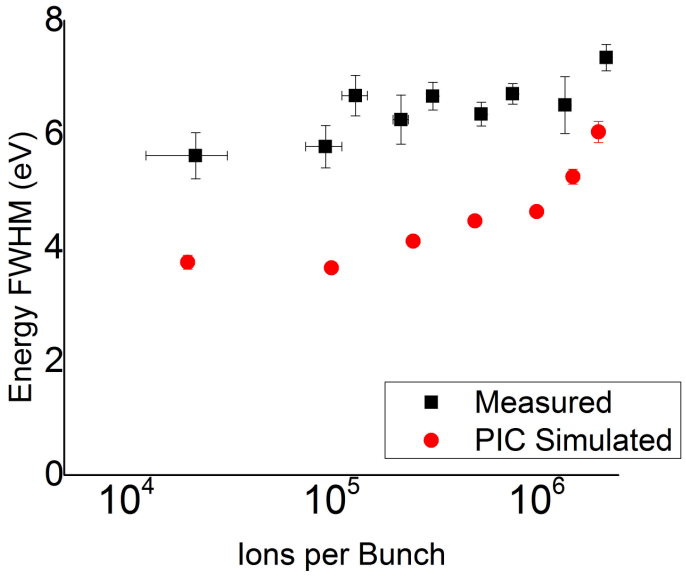

Figure 6.27: Measured energy widths of bunched beams versus ion count per bunch.

6.3.2.3 Measured Time and Energy Widths versus Extraction Field

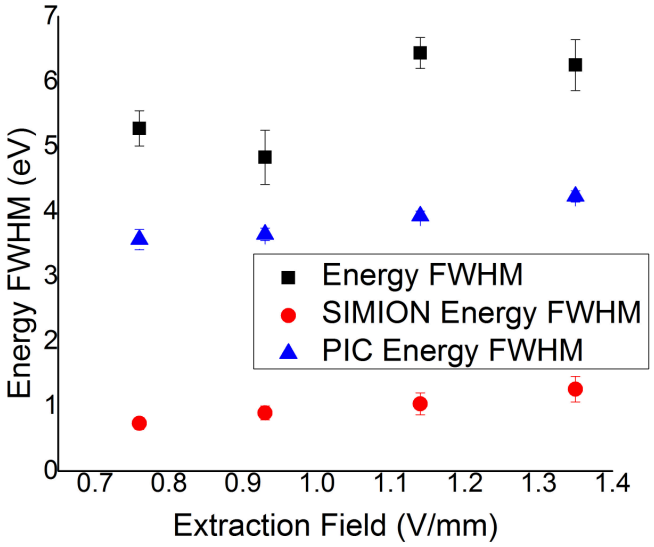

Figure 6.28: Measured time of flight spectra of bunched beams as a function of extraction field. As with the efficiency measurements, the extraction fields were calculated using experimental voltage inputs with a SIMION model.

The effect of extraction field strength on time and energy spread of bunched beams was also studied. The results are shown in Figures 6.28 and 6.29. Larger fields result in a slight increase in energy spread, though the shallowest fields result in a substantial increase in time spread. Two different sets of simulations are also shown. The particle in cell code was used to take space charge effects into account, while the SIMION simulations only consider fields due to applied static voltages and RF voltages. The measurements were performed with 10^5 ions per bunch, and comparison with the simulation results demonstrates that, at this level, space charge effects serve to increase the observed energy spread, and that for reliable predictions of time and energy spread of ion bunches with on order of 10^5 ions per bunch, simulation code that can represent the effects of space charge is necessary.

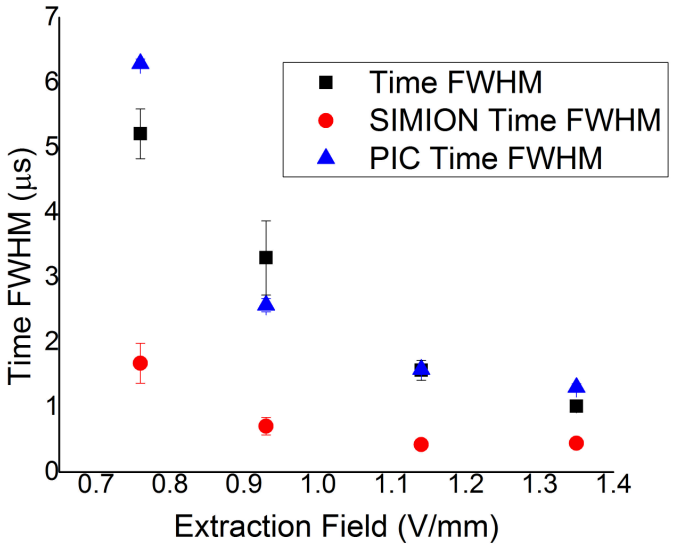

Figure 6.29: Measured energy spread versus extraction field, compared to PIC and SIMION simulation results.

6.3.2.4 Measured Time and Energy Widths versus Longitudinal Trap Depth

The effect of the static voltage longitudinal trap depth on bunched beam time and energy spread was also investigated. The results are portrayed in Figures 6.30 and 6.31. The trap depth appears to have little effect on either time or energy spread. While previous simulation results indicate that a shallower trap should result in a longer pulse, those simulations were performed over a much longer range of trap depths. Taking measurements over such a range is impractical due to the limitations of the efficiency of the system.

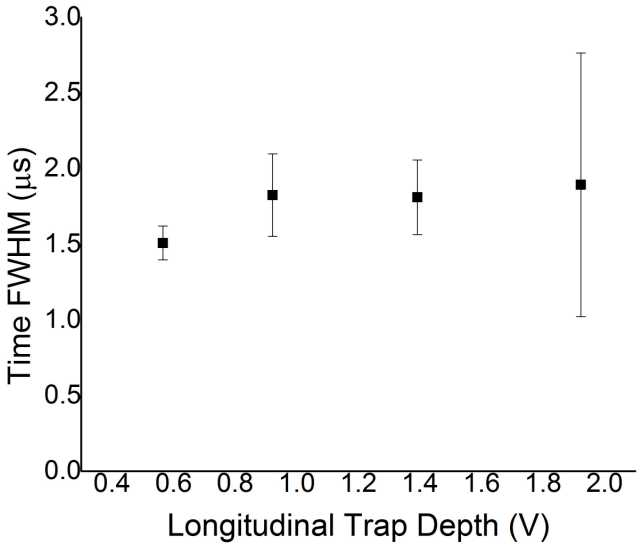

Figure 6.30: Measured time widths as a function of longitudinal trap depth.

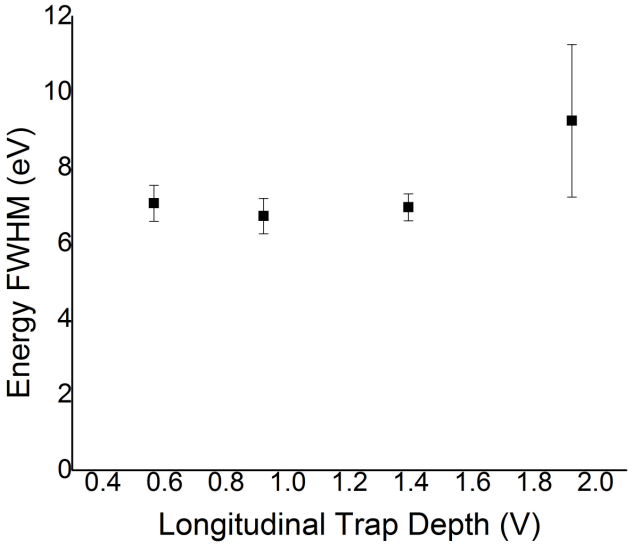

Figure 6.31: Measured energy widths as a function of longitudinal trap depth.

6.3.3 Transverse Emittance Measurements

In addition to efficiency, time width and energy spread measurements, transverse emittances were measured as well. The effects of variations in longitudinal trap depth, ions per bunch, cooling time, buffer gas pressure, stability parameter and pseudopotential depth were investigated. Measurements were made by scanning an electrostatic quadrupole lens to change the focus of the ejected beam, and imaging the beam on an MCP phosphor screen. The lens in question is the quadrupole singlet located at the entrance to the BECOLA switchyard (see Figure 6.1), and the MCP is located on the downstream 0° port of the switchyard. The basic procedure for determining the transverse emittance is outlined below, and a more detailed description is provided in the transverse emittance measurement appendix.

- Simulations were run to determine the elements of the beam transport matrix from the lens to the MCP as linear functions of lens voltage
- The beam is imaged with an MCP and phosphor screen.
- Beam images are recorded as a function of lens voltage.
- Horizontal and vertical projections of the beam image are fit to Gaussian functions, and the widths are extracted as fit parameters.
- The square of the beam width is plotted versus lens voltage, and fit to a parabola.
- The parabolic fit parameters and the coefficients from the transport matrix are used to calculate the position and momentum variances and covariance of the beam as it enters the lens.

- The emittance of the beam is calculated according to Equation 4.1. All calculated RMS emittances were multiplied by 6 to obtain the 95% confidence interval values.
- The emittance uncertainty is determined by propagating the calculated standard error of the fit parameter from the beam profile fit.

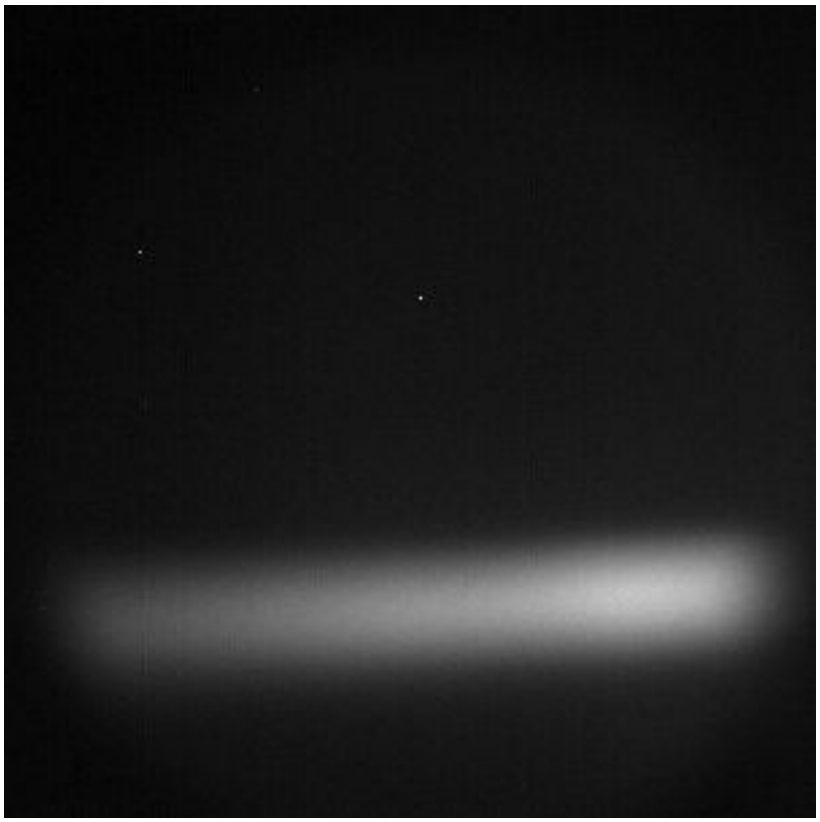

Figure 6.32: Example of a beam spot on MCP phosphor screen.

Unless otherwise specified, the transverse emittance measurements were carried out with 0.35 V/mm extraction field, 3 V longitudinal trap depth, 5.3 MHz RF frequency, 900 V_{pp} RF amplitude, a buffer gas pressure in the buncher of 0.3 mTorr, and about 5×10^4 ions per bunch. The quoted RF parameters yield a stability parameter value of about 0.33, and a pseudopotential depth of approximately 38 V. Unlike the longitudinal emittance measurements, the transverse emittance measurements were performed with comparatively

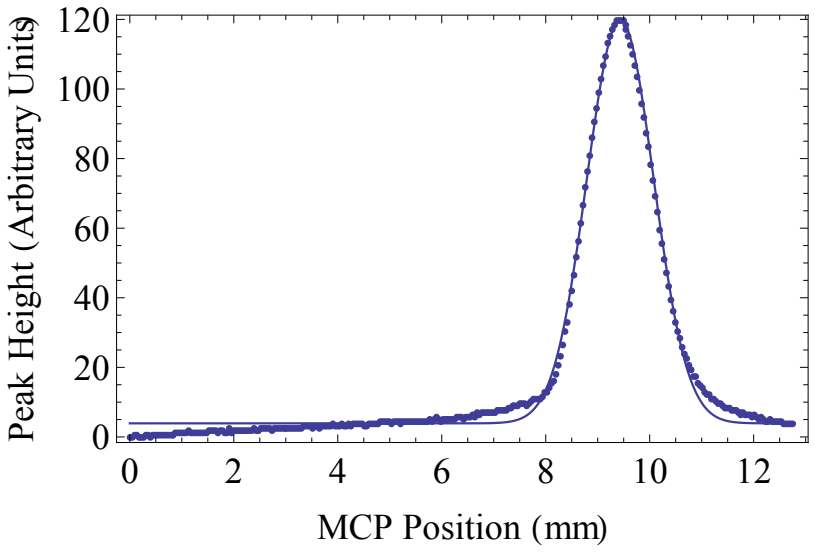

Figure 6.33: Example of beam profile projected onto one axis with a Gaussian fit.

high RF parameters due to the increased overall efficiency, as well as the observed relative insensitivity of the efficiency to other parameters, especially ion counts per bunch and cooling time, at high RF values.

6.3.3.1 Transverse Emittance versus Longitudinal Trap Depth

The results of beam emittance measurements versus static potential trap depth are shown in Figure 6.35. An increase in transverse emittance is apparent as the longitudinal trap depth is increased. This can be explained by referring to Equation 2.12, which shows that the transverse pseudopotential is weakened as the longitudinal trap depth is increased, leading to a larger transverse emittance (see Equation 2.22). The effect is likely magnified by space charge effects, which are not taken into account in the SIMION simulation results found in Figure 4.21.

Another result found in Figure 6.35 and in all transverse emittance studies shown here is that the emittance in the vertical direction is consistently larger than that of the horizontal. In principle the two quantities should be the same. One possible explanation for the discrepancy

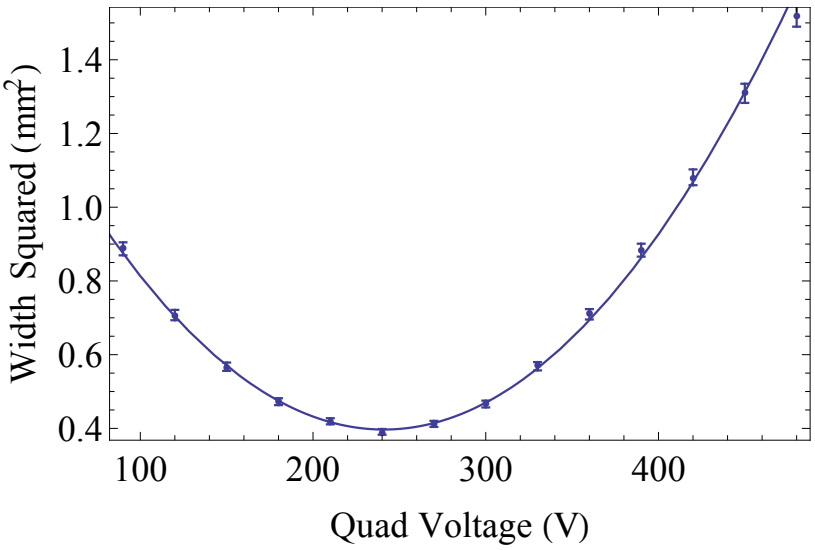

Figure 6.34: Example of beam profile widths (squared) plotted versus lens voltage with parabolic fit.

is related to beam steering. Experimentally it is known that significant steering is needed after the buncher to transport the beam to the switchyard, suggesting a misalignment in the ejection optics. One possible consequence of such a misalignment is that, if the beam passes near an electrode surface in the lens, nonlinear optical effects could serve to increase the emittance in one direction.

6.3.3.2 Transverse Emittance versus Ion Count per Bunch

Figures 6.36 and 6.37 depict the results of measurements of transverse emittances as a function of ion counts per bunch for two different sets of RF parameters. Figure 6.36 shows the results for the higher frequency and amplitude RF settings, while Figure 6.37 displays the results from using RF parameters more typically employed in collinear laser spectroscopy measurements. The higher RF frequency and amplitude produce a lower stability parameter (0.33 compared to 0.8) and larger pseudopotential depth value (38 V as opposed to 11 V) than the 1.2 MHz and 110 V_{pp} case, both of which will result in diminished transverse motion

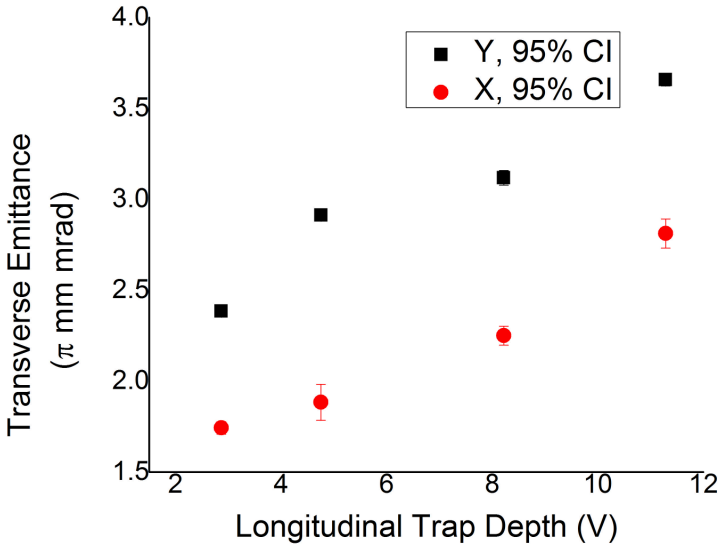

Figure 6.35: Measured transverse emittances versus static trap potential depth.

in the trap and therefore lower overall transverse emittance measurements. The deeper pseudopotential also serves to mitigate not only losses, but unwanted emittance growth in the instance of larger numbers of ions in the buncher. Note that, in this context, the ion per bunch number refers to the number of ions going into the buncher. A particle in cell calculation has been included in the figure depicting the results of the measurements using the lower RF frequency and amplitude in order to explore the effect of space charge. The underprediction of extracted emittances is, once more, likely due to a combination of mismatched RF phases and ion optical misalignment.

6.3.3.3 Transverse Emittance versus Cooling Time

The effect of cooling time on transverse emittance was also studied, and the results are shown in Figure 6.38. The results indicate that, for the cooler pressure and upstream drag field used, the ion motion in the transverse direction remains cold as the ions drop into the static potential trap. Since the trap is formed in the longitudinal direction, this is consistent with

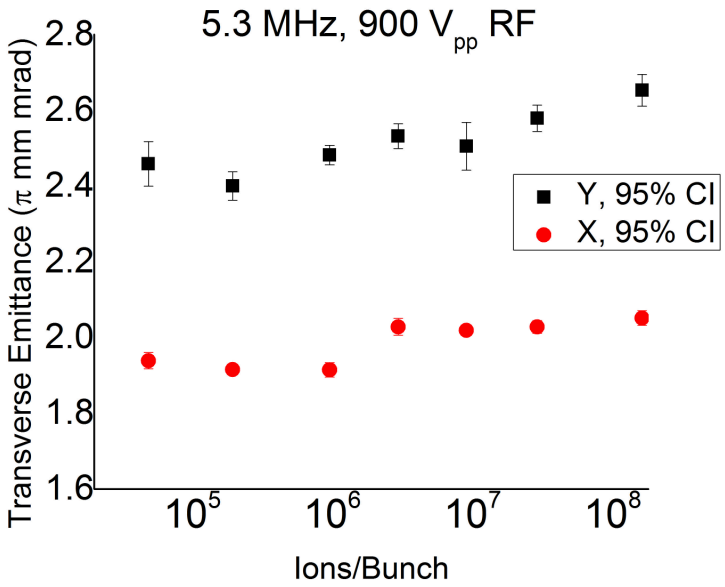

Figure 6.36: Measurement of extracted transverse emittance as a function of incident ions per bunch.

expectation. The cooling times required in the buncher, therefore, are dictated by the need to remove the excess energy gained by the ions falling into the static potential well, which does not affect transverse degrees of freedom.

6.3.3.4 Transverse Emittance versus Buncher Pressure

The results of transverse emittance measurements as a function of buncher pressure are presented in Figure 6.39. The data indicate that a buncher pressure of about 0.5 mTorr, which translates to a cooler pressure of about 50 mTorr, is necessary for complete cooling of transverse ion motion for an incident energy of about 150 eV and a very gentle drag field of about 0.8 V/cm.

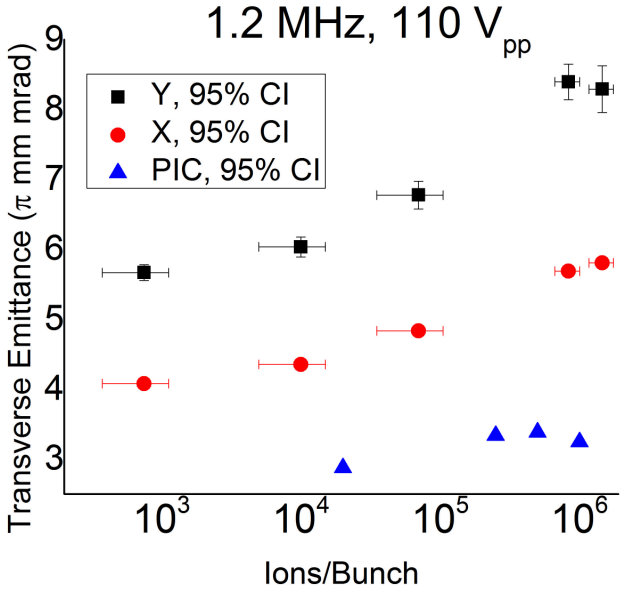

Figure 6.37: Measurement of extracted transverse emittance as a function of incident ions per bunch.

6.3.3.5 Transverse Emittance versus Pseudopotential Depth

Pseudopotential depths were also varied to study the impact on extracted transverse emittances. The results of this investigation and those of a particle in cell simulation using the same parameters are shown in Figure 6.40. As the pseudopotential was scanned, the RF voltage and frequency were varied in such a way as to maintain a constant stability parameter. The results show a decrease in extracted transverse emittance with increased pseudopotential depth, which is consistent with SIMION results (see Figure 4.12). Once again, however, although the overall trend agrees with measurement, the absolute value predicted in SIMION simulation is low due to the absence of space charge effects. The particle in cell results are much more successful in reproducing experimental results, while the remaining discrepancy is likely due to RF phase mismatch or electrode misalignment. Although the overall decrease with increasing pseudopotential is consistent with expectation, Equation 2.22 predicts that

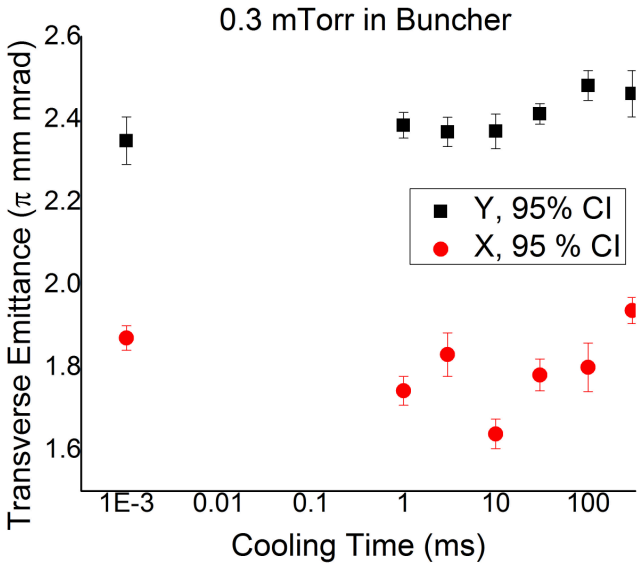

Figure 6.38: Measured transverse emittances as a function of cooling time in the buncher.

the emittance should scale as $\sim \frac{1}{\sqrt{V_{pseudo}}}$. This behavior is less apparent than it was in simulation. Further studies over a larger pseudopotential range may confirm the predicted behavior, but the frequency range over which the present RF circuit may be tuned limits the range of pseudopotentials available with a fixed stability parameter.

6.3.3.6 Transverse Emittance versus Stability Parameter

A complementary study was carried out where the stability parameter q was varied while the pseudopotential depth was held constant. The results are shown in Figure 6.41. Over the range measured, the results agree with the modest increase observed in in the SIMION simulation results (see Figure 4.15). As with the other studies presented, the mismatch between simulated values and measured quantities can most likely be ascribed to space charge effects.

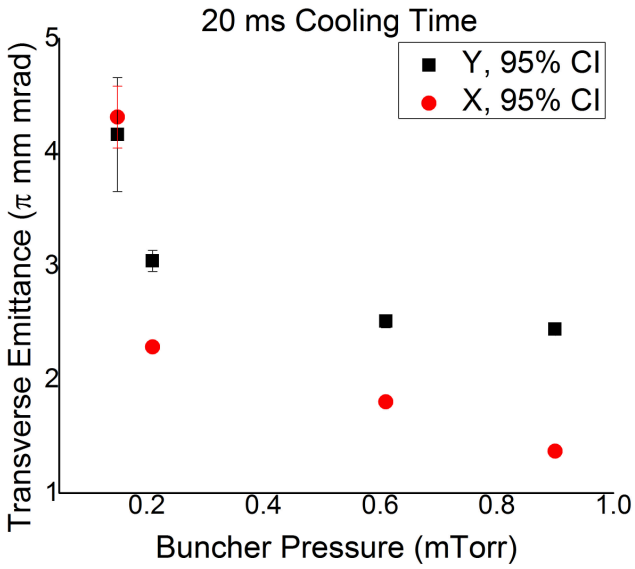

Figure 6.39: Transverse emittance measurements versus buncher pressure. The cooler pressure is about a factor of 100 higher than that in the buncher due to the differential pumping scheme.

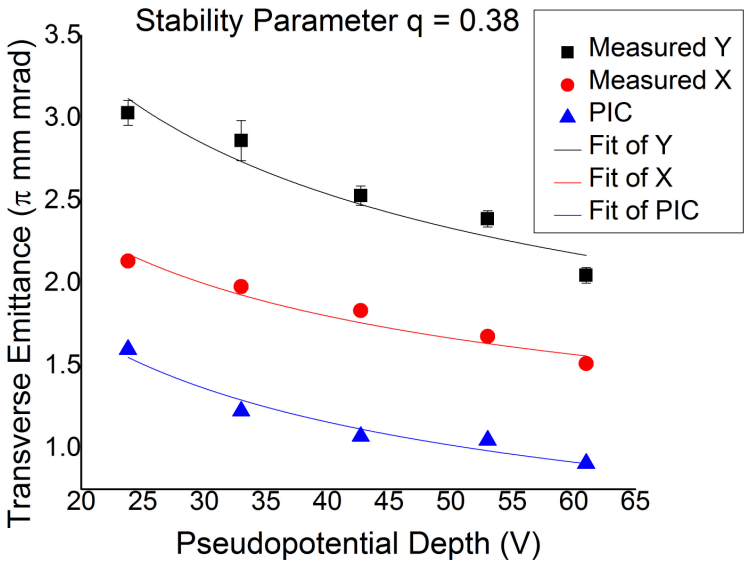

Figure 6.40: Measurements and PIC simulation of transverse emittances versus RF pseudopotential, and fit to $f(V) = a + \frac{b}{\sqrt{V}}$. stability parameter q was held at 0.38.

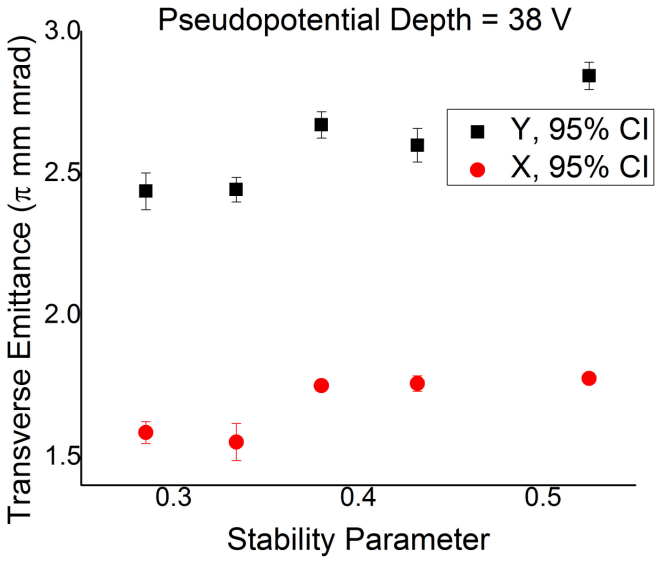

Figure 6.41: Measured transverse emittances versus stability parameter. The pseudopotential was kept constant.

Parameter	**Efficiency**	**Transverse Emittance**	**Energy FWHM**	**Time FWHM**
Buncher Pressure	Increases	Decreases	No Result	No Result
Cooling Time	Decreases	No Change	No Result	No Result
Ions/Bunch	Decreases	Slightly Increases	Slightly Increases	Increases
Longitudinal Trap Depth	Decreases	Increases	No Change	No Change
Extraction Field	Decreases	No Result	Slightly Increases	Decreases
Pseudopotential Depth	Increases	Decreases	No Result	No Result
Stability Parameter	No Result	Slightly Increases	No Result	No Result

Table 6.1: Response of buncher effficiency and extracted beam qualities to increases in buncher parameters.

6.3.4 Beam Cooler and Buncher Commissioning Measurement Summary

Table 6.1 lists the dependencies of buncher efficiency and extracted beam properties on increases in different cooler and buncher operational parameters. Increases in cooler pressure show improved efficiency as well as reduced transverse emittance. Since there is no further improvement in either quantity beyond 140 mTorr, it is recommended to run the cooler at this pressure.

There is an interdependence between the effects of cooling time and number of ions in the buncher on buncher efficiency. For larger numbers of ions in the buncher, the buncher efficiency is more sensitive to longer cooling times. For a buncher pressure of 1.4 mTorr, a cooling time of no more than 5 ms is necessary, and to mitigate the effects of overfilling the trap, it is recommended to operate the buncher with fewer ions per bunch at a higher repetition rate if possible for high incident beam rates.

Commissioning results indicate that a shallower trap depth is preferable to maximize efficiency and minimize transverse emittance. However, for high beam rates ($>10^6$ ions/bunch),

Parameter	**Value**
High Voltage	29.85 kV
Hyperboloid Voltage	-1 kV
Cone Voltage	-1 kV
Drag Electrode A Bias	10 V
Drag Electrode B Bias	1 V
Trap Electrode C Bias	0.015 V
Trap Electrode D Bias	0.015 V
Trap Electrode E Bias	-0.02 V
Trap Electrode F Bias	-4 V
Switching Electrode G Trapping Bias	20 V
Switching Electrode G Extraction Bias	-5 V
Slew Time	5 μs
RF Frequency	1.2 MHz
RF Amplitude	100 V_{pp}
Cooler Pressure	140 mTorr
Bunch Time	2-5 ms
Ions/Bunch	$<10^5$
Typical Emittance	3 π mm mrad
Typical Energy FWHM	5 eV
Typical Time FWHM	3 μs
Typical Efficiency	>50%

Table 6.2: Optimized parameters for BECOLA beam cooler and buncher operation with a singly charged, mass 39 beam. All biases are with respect to the high voltage bias. Electrode labels refer to those found in Figure 4.11.

one observes a second peak in the time of flight spectrum which has a different energy than the main peak (see Figure 6.25). The emergence of the second peak can be mitigated by operating with a deeper longitudinal trap. While deeper traps have been shown to reduce buncher efficiency, for beam rates sufficient for an additional peak to appear efficiency is a secondary concern.

Operating with a larger extraction field presents a tradeoff between a shorter bunch width, but with lower efficiency and slightly larger energy spread. In general it is suggested to operate with a gentle extraction field to minimize energy broadening.

As illustrated by Figure 6.20, the downstream half of the beam cooler and buncher must be operated with a relatively low RF amplitude for collinear laser spectroscopy measurements. The choice of 100 V_{pp} and 1.2 MHz is the result of a compromise between operating such that a reasonable energy spread is still achievable, yet still maintaining a sufficiently deep pseudopotential to operate efficiently. At such low amplitudes, the efficiency becomes much more sensitive to other operational parameters, especially pressure, cooling time and ion number in the buncher. Therefore determining the effect of these parameters on energy and time spread at a fixed efficiency becomes challenging. RF parameters will require adjustment for ions of different mass.

6.3.5 Online Commissioning Measurement: Hyperfine Spectrum of Rare Isotope ^{37}K

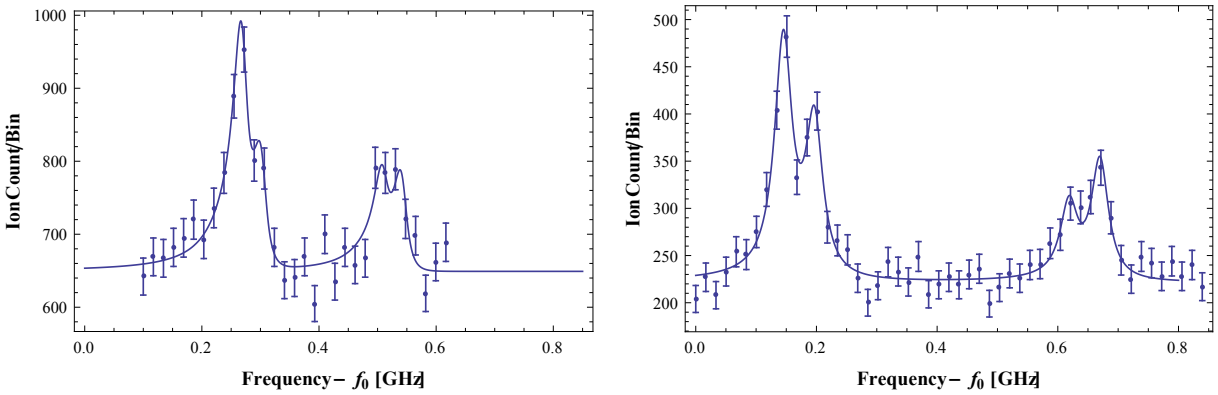

(a) (b)

Figure 6.42: Left (a): Hyperfine spectrum of D1 transition of ^{37}K and Voigt fit. Right (b): Hyperfine spectrum of D1 transition of ^{39}K and Voigt fit. Due to hyperfine isotope shift, the f_0 values in the two plots are not the same.

In addition to the commissioning studies performed using an offline ^{39}K source, an online measurement using a ^{37}K beam from the NSCL coupled cyclotrons was carried out in order to commission the BECOLA facility, including the beam cooler and buncher, and demonstrate the capability to perform collinear laser spectroscopy measurements with unstable beams. The secondary ^{37}K beam was thermalized in the gas stopping facility, reaccelerated to 30 keV through the ion guide discussed in Chapter 5, and transported to the BECOLA beam cooler and buncher. The beam was cooled and bunched using the 1.2 MHz, 110 V_{pp} RF settings on the downstream rods in order to minimize energy spread. The bunched beam was reaccelerated towards the collinear beamline, where fluorescence spectra were taken in a similar fashion to the offline energy and time width diagnostics. The ion beam was sent through the charge exchange cell loaded with Na vapor for neutralization, and the atom beam drifted collinearly with the laser light through the photon counting region as the charge

exchange cell bias was scanned. The buncher parameters used are the same as those listed in Table 6.2, except that a longer cooling time of 100 ms was used. Sample fluorescence spectra of the online ^{37}K beam and offline ^{39}K reference beam are shown in Figure 6.42. Note that, since the two nuclei are isotopes of the same element, the fine structure of the electron configuration is the same in both cases. Further, since both isotopes have the same spin $I = \frac{3}{2}$, the hyperfine spectra have similar structures, though with different spacing. The fits yield energy widths of about 4.5 eV and 4 eV respectively. The results indicate a successful commissioning of the BECOLA facility with rare isotope beams, and signal readiness for future rare isotope experiments.

Chapter 7

Conclusions

A beam cooler and buncher for collinear laser spectroscopy of rare isotopes with advanced features was developed and commissioned. A series of simulations was performed to refine the design characteristics of the beam cooler and buncher for optimal beam transport and cooling properties. A prototype electrode structure was built and used to perform RF and static voltage discharge studies to determine what operating voltages and buffer gas pressures were attainable. An ion guide was built as part of the NSCL gas stopping facility, and incorporates many of the same design principles intended for the BECOLA beam cooler and buncher. The performance of the ion guide was characterized, and the results lent additional insight into the design and construction of the BECOLA beam cooler and buncher. The characterization measurements of the BECOLA beam cooler and buncher using the offline stable potassium ion source and the commissioning experiment with a rare isotope beam of ^{37}K were completed successfully.

RF frequencies and amplitudes of order 5 MHz and 900 Vpp provide efficient injection into the cooler, while the capability to employ lower frequencies and amplitudes enables low ion bunch energy spread while still maintaining efficient operation, provided the trap is not overfilled. A cooler pressure of 140 mTorr allows the ions to be cooled sufficiently to remain confined in the weaker pseudopotential in the downstream region, and is possible despite large RF fields in the upstream half due to the geometry of the coldhead. For rates

of available rare isotope beams of interest, the buncher can operate with high efficiency to deliver low energy spread beams for collinear laser spectroscopy. For higher rates, the time structure can be managed by using a deeper longitudinal trap.

The BECOLA beam cooler and buncher has been demonstrated to efficiently deliver cooled, bunched beams with low energy spread and emittance for collinear laser spectroscopy. Efficiencies of 80% are typically achieved, and a 2 π mm mrad emittance, 5 eV energy spread and 5 μs time width are well suited for collinear laser spectroscopy measurements. Performance broadly agrees with expectations based on particle in cell simulation results, though there is still minor disagreement between measurement and simulation. In addition, a significant increase in the sensitivity of collinear laser spectroscopy measurements by the use of bunched beams has been demonstrated. Such a sensitivity enhancement enables the measurement of ever more exotic nuclei where production rates would otherwise pose a challenge to collinear laser spectroscopy experiments.

APPENDICES

Appendix A

Radiofrequency Circuit and Bias Channels

A.1 Circuit Layout

The RF system (see Figure A.1) consists of an RF amplifier, an impedance matching transmission line transformer [44], two inductors as close in inductance as can be managed, a tuning capacitor in parallel with the RFQ system, and the RFQ electrode structure itself. The parallel capacitors form the capacitive load of a resonant LC circuit, while the two inductors form the inductive portion. The placement of one inductor each on a branch of the circuit, corresponding to opposite pairs of RFQ electrodes, results in amplitudes equal and opposite at complementary RFQ electrode surfaces, providing the desired oscillating quadrupole field.

The RF amplifier outputs the RF signal with a characteristic impedance of 50 Ω. In order to avoid reflection and deliver the maximum power to the load (the RFQ electrodes, in this case), the impedance of the load must be matched to the output impedance of the amplifier. On resonance, the LC circuit has an impedance of order 1 Ω, far from the 50 Ω output impedance of the amplifier. In order to match the output impedance of the amplifier while still taking advantage of the large voltages resulting from a resonantly driven load, an

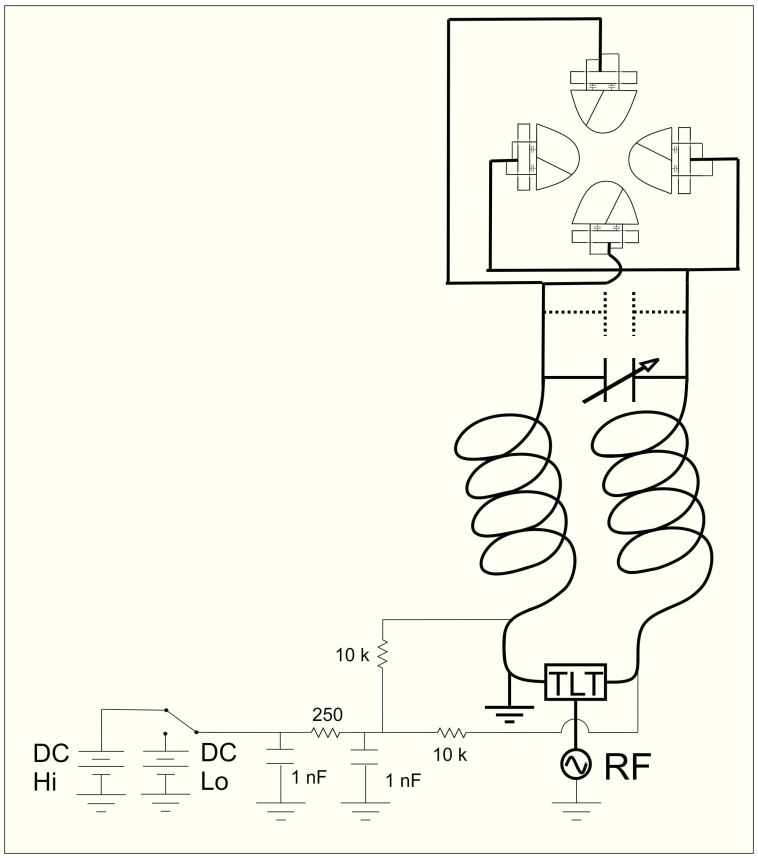

Figure A.1: Sketch of RF and bias voltage circuit, with switch and low pass filter. Only one bias channel is shown in this example. Typical resistance and capacitance values are listed. Thick lines indicate RF circuit components; thin lines represent static voltage circuitry. At points of intersection, bias leads are threaded through the center of hollow RF conductor, e.g. through the inductors.

additional impedance matching stage is necessary. In other systems, a traditional magnetic coupling transformer with a primary to secondary winding ratio of 7:1 ($\sim \sqrt{\frac{50\Omega}{1\Omega}}$) about a ferrite core is used. While this approach is successful for systems with lower RF frequencies and amplitudes, it was found that for the frequencies and amplitudes desired for the cooler and buncher system the thermal losses in the ferrite near the secondary winding are significant, in some cases even causing sufficient thermal stress in the ferrite as to cause it to crack. This destructive obstacle was circumvented by the use of a series of transmission line transformers. The basic idea is that pairs of wires are wound around the ferrite core such that the current

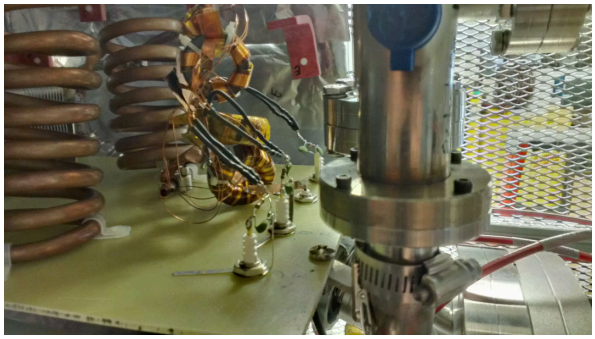

(a)

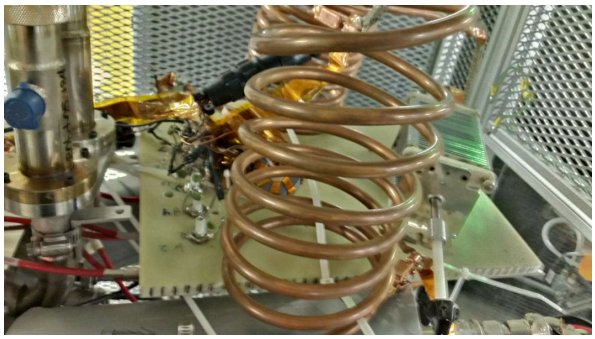

(b)

Figure A.2: Left (a): Photo of the upstream RF circuit. Right (b): Photograph of the downstream RF circuit.

flowing through each wire is in the opposite direction from that of the paired wire. The net magnetic flux through the ferrite core is therefore zero, thus eliminating the dissipation effects due to the rapid change in alignment of magnetic domains in the ferrite. Sevick [44] describes such a transformer designed to match an output to a load impedance which is larger than the output by a factor of 4. For the purpose of matching the RF amplifier to a resonant load, two such transformers were connected in series and inverted to attain an approximate output to load transformation ratio of $\sim$ 16:1.

The two inductors in the circuit were made to give a resonant frequency near approximately 6 MHz. With a native RFQ capacitance of approximately 200 pF, along with stray inductances in the circuit, coil inductances of about 0.5 μH were required for high frequency operation. Larger inductors were used for the low frequency case. An online inductance calculator [47] was used to estimate the dimensions required for the inductors. Wires for the bias leads were threaded through a length of copper tube, which was then wound into the correct shape for the inductor. To tune the circuit, a variable capacitor was installed, giving a circuit bandwidth of about 3.5 to about 6.2 MHz. For low frequency operation, larger inductors were used, and additional parallel capacitance was added.

The RF and bias were connected to the flange via a plug in such a way that the bias voltages are carried on the pins, while the RF is on the outer conductor of the plug (see Figure A.4). After the inductor, the bias leads were fed through additional tubular mesh to the plug, while the RF is fed from the inductor end through the tubular mesh to the plug. Note that, in this configuration, the RF is connected to the internal structure through the flange itself.

The bias leads were fed through the center of the tubes used to make the inductor in order to inductively decouple the RF from the output of the bias power supply. Additional RF attenuation at the bias input was accomplished through RC low pass filters. Since bias signals were sent to RFQ segments with the same bias offset but opposite RF phases, additional resistance on each branch going to either phase was necessary to further decouple RF from the power supply. In the case of the last segment, the bias value was connected to a switch [48] to open and close the buncher. The values from the low pass filter (see Figure A.1) resulted in a characteristic switch time of about 5 μs.

Photographs of the upstream (a) and downstream (b) RF circuits are shown in Figure A.2. The circuits are mounted to a G-10 base. The feedthroughs on the upstream side correspond to electrodes UC, UB, RF and UA from foreground to background (see section on bias channels). In the downstream circuit, substantially larger inductors than those of the upstream circuit are used to attain lower resonant frequencies. The feedthrough order on the downstream side runs from DA to DG from foreground to background, opposite of the upstream side. The tuning capacitor can be seen to the right of the foreground inductor.

A.2 Bias Channels

Bias channel names are labeled in Table A.1, and electrode positions are sketched in Figure A.3. The upstream hyperboloid and cone determine the injection optics. UA determines the injeciton energy. UB, UC, DA and DB determine the drag field. Note that, for a smooth drag field, UB and DA should share the same value, as should UC and DB. DC through DF determine the trapping potential. DG determines the trapping barrier and extraction field. Dhyp and Dcone, currently tied together, dictate the ejection optics.

At the plug/flange interface, the pin assignments are illustrated in the right portion of Figure A.4. Each channel is labeled with a letter on the face of the plug, which has been matched to the corresponding second letter of the electrode. For instance, on the downstream side, electrode DA is connected to pin A, DB to pin B, and so on. On the upstream side, UA goes to A, etc. The gap on the left represents the notch on the physical plug that matches the correct pin to the correct hole.

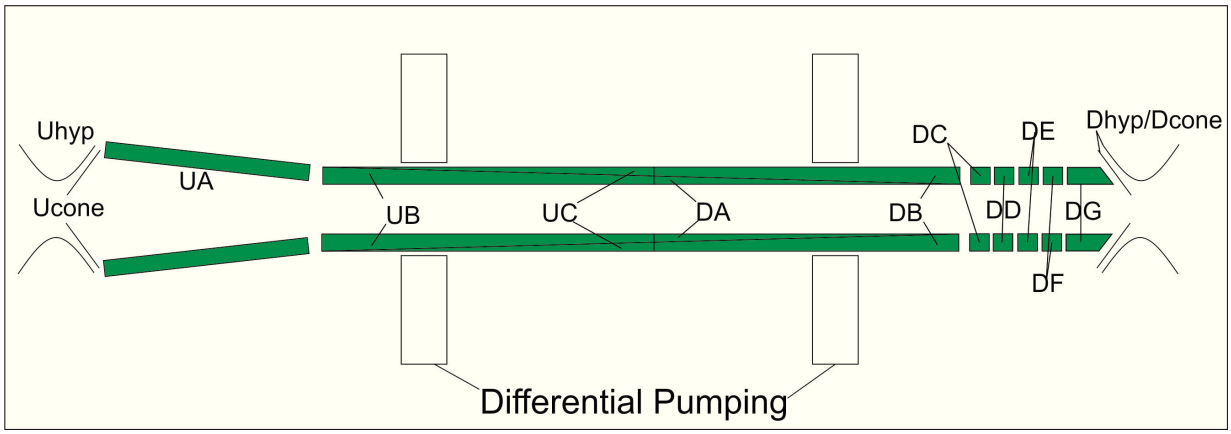

Figure A.3: Sketch of electrode layout, with each electrode labeled. Beam travels left to right.

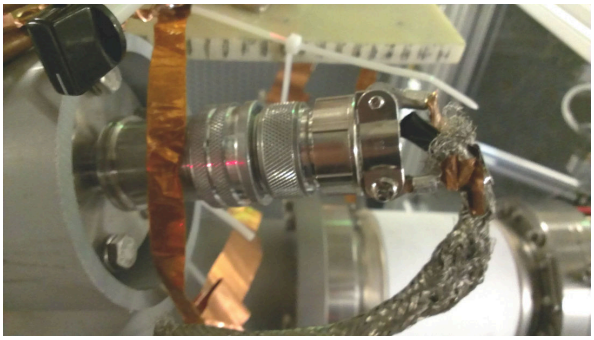

(a)

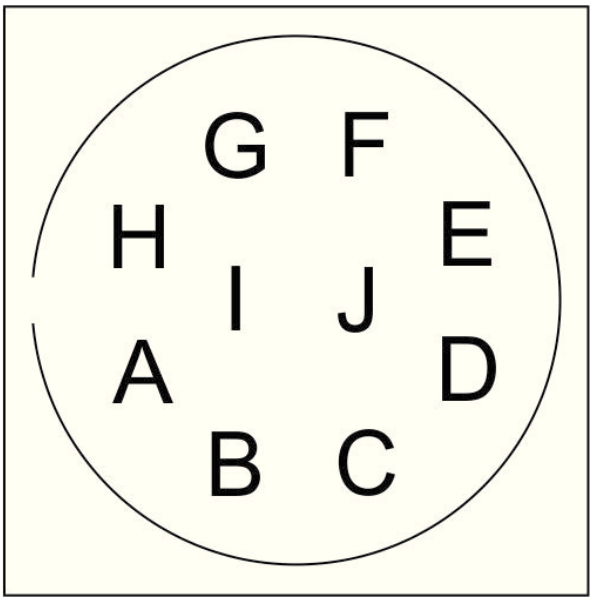

(b)

Figure A.4: Left (a): Photograph of flange/plug interface (see also Figure 6.12). Right (b): Diagram of the pin assignment as viewed from the face of the plug.

A.3 Circuit Tuning

There are two different modes in which to run the RF circuit. In general, for collinear laser spectroscopy studies, the upstream and downstream circuits are driven at different frequencies, and are therefore tuned independently. In this case, one simply attaches scope probes as close to the flange interface as possible, and tunes the variable capacitor until the maximum amplitude is reached. The case where the upstream and downstream are run at the same frequency is slightly more complicated. It turns out to be easier to drive the upstream and downstream circuits in parallel in this case. The steps to tune the combined circuit are listed below.

- First off, only tune the circuit with low RF amplitudes, under 100 Vpp or so, or ~ 1 W out of the amplifier.
- Use a scope probe (100x) to measure the RF amplitude.

Electrode	Cable	Control Channel	Typical Value (V)
Uhyp	5	PSB5_D1221	1350
Ucone	6	PSB6_D1221	-2900
UA	1	PSB1_D1221	10
UB	13	PSB5_D1232	10
UC	3	PSB3_D1221	1
DA	2	PSB2_D1221	10
DB	4	PSB4_D1221	1
DC	10	PSB2_D1232	0.2
DD	11	PSB3_D1232	0.2
DE	16	PSB8_D1232	0
DF	7	PSB7_D1221	-4
DGaccu	12	PSB4_D1232	20
DGextr	8	PSB8_D1221	-10
Dhyp	15	PSB7_D1232	-1000
Dcone	15	PSB7_D1232	-1000

Table A.1: Electrode, cable number, and control system channel names. The two values for DG refer to the trapping and ejecting voltages. The physical locations inside the cooler and buncher are given in Figure A.3. All control channel names are preceded by DBEC_BCB.

- Dial the amplifier or function generator to the desired frequency.
- Detune both circuits off resonance.
- Tune one of the circuits to the resonant frequency (I like to start with the upstream circuit).
- Tune the other circuit so that the upstream and downstream amplitudes are the same.
- The amplifier or AFG frequency may need a final adjustment by about 50 kHz or so to get the compound circuit on resonance.
- Increase RF amplitude to desired value. The circuit is now tuned.

Appendix B

Transverse Emittance Analysis Technique

In order to characterize the outgoing beam from the BECOLA cooler and buncher, the quadrupole scan was employed to measure the transverse emittance. This technique takes advantage of basic ion optics and diagnostic hardware already in place, and requires no additional components such as an Allison scanner or pepper pot mask. To perform this measurement, an electrostatic lens, such as an electric quadrupole, and a beam imaging device, such as a microchannel plate (MCP) with a phosphor screen are required. The lens voltage is varied, and the beam width is recorded as a function of lens voltage. Note that, for best results, it is necessary to scan through the focus or waist of the beam.

One can parametrize the beam in terms of the variances of ion position σ_x^2 and transverse momentum $\sigma_{x'}^2$, and the covariance $\sigma_{xx'}$. This can be written in terms of a so-called Σ matrix:

$$\Sigma = \begin{pmatrix} \sigma_x^2 & \sigma_{xx'} \\ \sigma_{xx'} & \sigma_{x'}^2 \end{pmatrix} \tag{B.1}$$

One can also define an R matrix

$$R = \begin{pmatrix} R_{11} & R_{12} \\ R_{21} & R_{22} \end{pmatrix} \tag{B.2}$$

to propagate the beam properties from one longitudinal position z_0 to another z_1. In this case the propagation of the sigma matrix follows

$$\Sigma_1 = R\Sigma_0 R^T \tag{B.3}$$

where R^T is the transpose of R. For the purpose of a quadrupole scan, R describes the propagation of a beam through the lens followed by a drift whose length is equal to the distance between the lens and the MCP. The elements of R are linear functions of the lens voltage, and can be calculated analytically using the thin lens approximation or simulated using an ion optics software package such as SIMION. For a particle that starts with a known off axis displacement but has no transverse deflection, the effect of the transport looks like

$$x_1 = R_{11}x_0 + R_{21}x'_0 \tag{B.4}$$

Similarly, the effect on an incident ion on axis with a known transverse velocity angle is

$$x'_1 = R_{12}x_0 + R_{22}x'_0 \tag{B.5}$$

Thus by simulating two hypothetical particles for different lens voltages the transport matrix elements can be determined.

The width of the beam as measured by the MCP can be expressed as a function of the R matrix elements and the initial conditions of the beam at the entrance to the lens, according to

$$\sigma_x^2(V) = R_{11}(V)(R_{11}(V)\sigma_{x_0}^2 + R_{12}(V)\sigma_{xx'_0}) + R_{12}(V)(R_{11}(V)\sigma_{xx'_0} + R_{12}(V)\sigma_{x'_0}^2) \tag{B.6}$$

The beam widths, or more precisely the square of the beam width measured at the MCP can be fit to a quadratic function of the lens voltage $f(V) = aV^2 + bV + c$. If Equation B.6 is separated by orders of the lens voltage, bearing in mind that the elements of R are linear functions of voltage, the coefficients can be equated to the fit parameters, yielding three equations in three unknowns relating the known fit parameters and simulated transport matrix elements to the (unknown) elements of Σ_0. Once that system of equations is solved, the RMS emittance of the beam can be calculated as the square root of the determinant of Σ_0.

$$\epsilon_{RMS} = \sqrt{|\Sigma_0|} \tag{B.7}$$

Appendix C

Beam Cooler and Buncher Design and Maintenance

C.1 Design

An exploded design view of the BECOLA beam cooler and buncher is shown in Figure C.1. In the drift regions immediately upstream of the deceleration gap and downstream of the ejection gap, the perforated tube maintains the external potential seen by the ions at ground, even while the outer vacuum chamber is on high voltage. The perforation permits pumping of the central region through which the beam traverses, while the tube maintains the potential experienced by the incident beam until it passes through a hole in the center of the endcap. The endcap is held in place by a vented insulator, which centers the endcap with respect to the beam axis while allowing a voltage difference between the grounded endcap and the outer flange on high voltage. This region of beamline is pumped by a 250 L/s turbomolecular pump to minimize buffer gas flow upstream. As of the time of the writing of this document, the downstream perforated tube is being replaced with an immersion lens with steering electrodes in order to improve downstream beam optics.

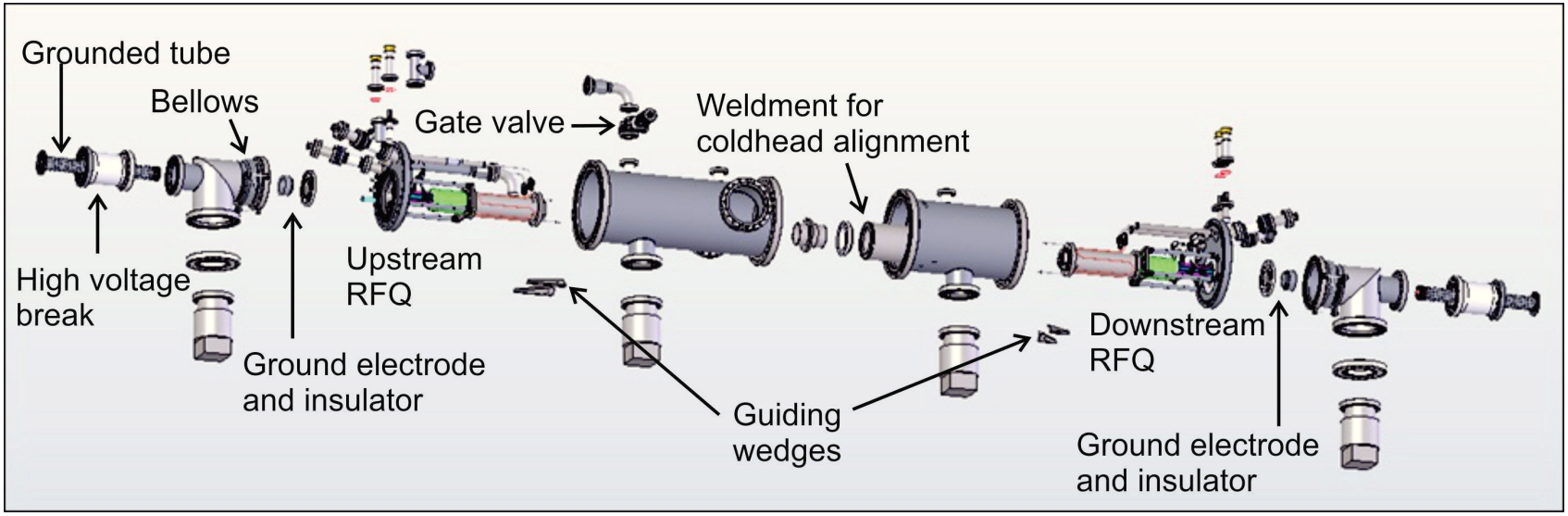

Figure C.1: Exploded design view of BECOLA beam cooler and buncher. For ease of machining and assembly, the RFQ structure is split into upstream and downstream subassemblies, each of which are mounted to flanges at either end of the vacuum chamber.

Due to the overall ∼120 cm length of the RFQ rods, the design is such that the RFQ rods are split into two separate sub-assemblies, an upstream half and a downstream portion (see Figure C.1). Each half is aligned to a weldment in the vacuum chamber which, along with alignment pins affixed to the coldhead pieces, guarantees that the ends of the two RFQ sections meet properly in the middle of the cooling region. An additional Macor piece in the alignment structure thermally insulates the liquid nitrogen cooled coldhead from the room temperature weldment. The two coldheads come into contact with the central Macor piece, forming an enclosed volume apart from the buffer gas inlet and differential pumping channels. Helium is fed into the central region, and when liquid nitrogen flows through the copper tubes, the buffer gas is cooled through contact with the coldhead. Gas flow out of the central volume is restricted by the differential pumping channels, while the larger external chamber is pumped by a pair of 250 L/s turbomolecular pumps. The differential pumping geometry maintains the pressure in the central cooling region about a factor of 100 higher than the pressure in the upstream or bunching region, which is consistent with simulation results. Keeping the coldhead close to the RFQ electrodes also limits the distance over which a discharge can occur, which permits running the RF at higher amplitudes at a given buffer gas pressure than was possible in the prototype studies discussed in Chapter 5, or alternatively, to run the same amplitude at higher buffer gas pressures. Whereas, according to Figure 5.3 discharges occurred at 900 Vpp at pressures less than 60 mTorr, similar amplitudes were attained at pressures above 140 mTorr.

On either side of the cooling region, the stack of Macor discs forms a differential pumping channel 14 cm long to achieve an estimated conductance of about 1.5 L/s. The differential pumping channel sits inside a metal collar, which, along with the upstream half of the coldhead (hollow cylinder with copper tube braised to the outside), is mounted to the vacuum

flange by four standoff rods for structural support. The buffer gas inlet runs from the flange to the coldhead through a 90° elbow and bellows, and the liquid nitrogen supply and return are visible on either side of the buffer gas inlet. The gas inlet is also equipped with a gate valve which is closed under normal operation, but which can be opened for rapid pumping of the central cooling region. Note also that the pressure gauge for the cooling region is located on the tee of the helium inlet, not on the cooling region itself. A rough calculation treating the helium inlet as a straight tube (despite the two 90° turns) 1 m in length and about 3 cm in diameter shows that the pressure in the cooler is about 10% lower than the readout value.

NSCL or FRIB affiliated readers interested in additional design details are referred to the mechanical design drawings for 20bcb05. Of particular interest are the drawings 20bcb05_001 and 20bcb05_069, which detail the composition of the upstream and downstream electrode assemblies respectively.

C.2 Maintenance

In terms of regular maintenance, the important things are to make sure that the buffer gas supply is adequate, and that the water circulator used to water cool the turbopumps is kept filled with water. The water circulator requires additional water about every month or so, and it is advised to use pure water in the cooling loop. A full sized helium bottle should last multiple years, so only infrequent exchanges are necessary.

The custom tees upstream and downstream of the main chamber are equipped with bellows which, when disassembly is necessary, can be retracted to allow the main vacuum chamber to slide laterally on the stand rails to the maintenance cart (NSCL users are referred to mechanical design drawings for 20bcb06 for details). To vent the chamber, simply turn

off the four turbopumps, close the upstream and downstream gate valves, and brake the turbos either via the valves on the turbos, or the valve on the southeast flange (facing the electronics racks). Once the chamber is vented and transferred to the secondary stand, the 13.25" flanges can be removed using the maintenance cart originally designed for use with the LEBIT buncher. Interested parties should contact the LEBIT group for access to the cart. A photograph of the flange mounted to the cart is shown in Figure C.2. Use the inner flange which otherwise attaches to the bellows.

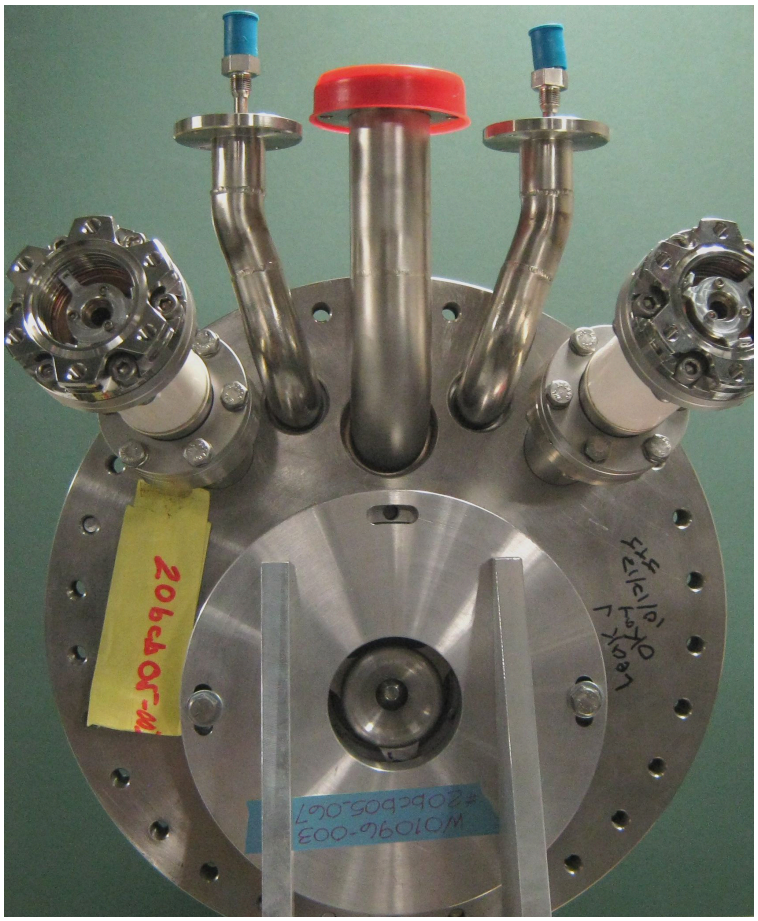

Figure C.2: 13.25" flange mounted to maintenance cart. RFQ electrodes are mounted to the far side.

If the RFQ electrode assemblies need to be removed, the upstream assembly needs to be removed first. The reason is that there is a minor alignment issue with the downstream

electrodes. For both the upstream and downstream assemblies, The Macor disc at the end of the electrode assembly centers the electrodes with respect to the weldment, but for the downstream electrodes the assembly needs to be guided in place from the upstream side. A plastic dowel inserted in the central region of the RFQ is useful to push the electrode assembly towards the center of the alignment piece. Two people are recommended for the installation of the downstream electrodes; one to push the electrodes into the chamber, and another to center the electrodes with the dowel. The upstream electrodes can be installed without this additional process. In both cases, however, while the cart facilitates the installation, it may be necessary to lift the electrode assembly slightly as it is being guided into or out of the vacuum chamber. Parts of the mounting assembly are partially occluded by the weldment and guiding wedges (see Figure C.1) used to guide the structure in place. Once the electrode assembly is in place, however, the guiding structure poses no obstacle.

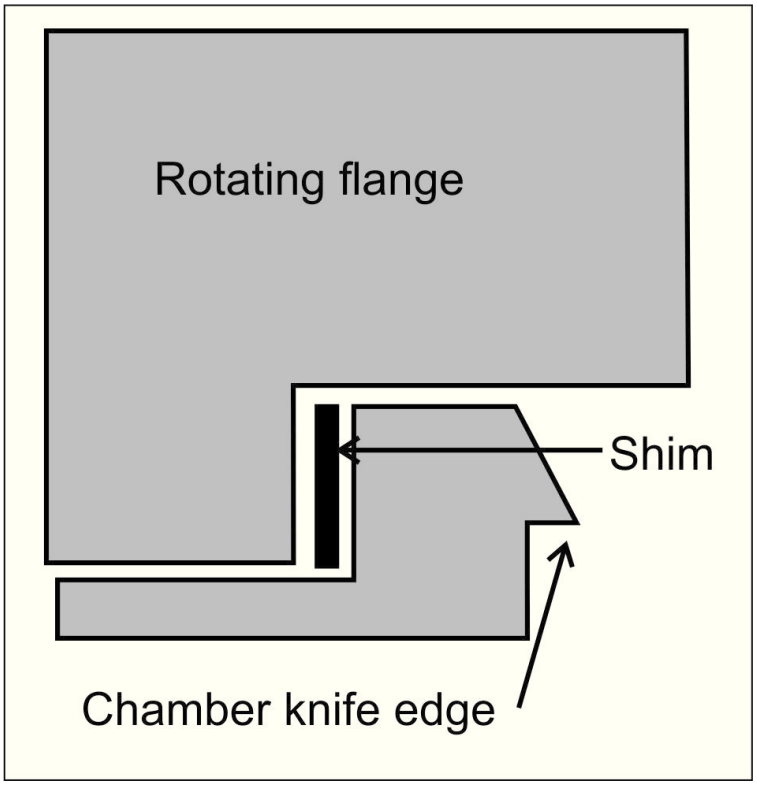

Figure C.3: Sketch of the shim under the rotating flange on the vacuum chamber.

When the vacuum chamber is being sealed up, it is crucial to make sure that the shims are in place between the protruding lip that holds the knife edge, and the rotating flange (see Figure C.3). Otherwise, the rotating flange will move too far forward with respect to the knife edge when the flanges are tightened together, and the knife edge will not form a proper seal with the gasket. 0.015" shims have been installed around the protrusion on the downstream side, and 0.005" are in place on the upstream side. The presence of these shims is indicated on labels on the vacuum chamber. There is no such issue on the flanges where the two halves of the vacuum chamber meet.

If it is necessary to remove the 2.75" feedthrough flange used to supply the RF and a majority of the bias voltages to the RFQ electrodes, one must take care to support the flange. The electrode connections are held in place by friction, and if the flange is not properly supported, the flange could fall, possibly damaging the feedthrough and disconnecting the leads from the feedthroughs. The leads are not labeled, and reconnecting the leads to the correct feedthrough could require removal of the entire electrode structure in order to identify which lead is associated with which electrode.

BIBLIOGRAPHY

BIBLIOGRAPHY

[1] R. Casten. *Nuclear Structure from a Simple Perspective*. Oxford science publications. Oxford University Press, 2000.

[2] E. M. Burbidge, G. R. Burbidge, W. A. Fowler, and F. Hoyle. Synthesis of the elements in stars. *Rev. Mod. Phys.*, 29:547, 1957.

[3] N. Severijns and O. Naviliat-Cuncic. Symmetry tests in nuclear beta decay. *Annual Review of Nuclear and Particle Science*, 61(1):23–46, 2011.

[4] H.G. Dehmelt. Nobel lecture: Experiments with an isolated subatomic particle at rest. In *Nobel Lectures, Physics 1981-1990*, 1989.

[5] W. Paul. Nobel lecture: Electromagnetic traps for charged and neutral particles. In *Nobel Lectures, Physics 1981-1990*, 1989.

[6] L.S. Brown and G. Gabrielse. Geonium theory: Physics of a single electron or ion in a penning trap. *Rev. Mod. Phys.*, 58:233–311, Jan 1986.

[7] K. Blaum and F. Herfurth. *Trapped charged particles and fundamental interactions*, volume 749. Springer, 2008.

[8] M. Wada, Y. Ishida, T. Nakamura, Y. Yamazaki, T. Kambara, H. Ohyama, Y. Kanai, T. M. Kojima, Y. Nakai, N. Ohshima, A. Yoshida, T. Kubo, Y. Matsuo, Y. Fukuyama, K. Okada, T. Sonoda, S. Ohtani, K. Noda, H. Kawakami, and I. Katayama. Slow RI-beams from projectile fragment separators. *Nuclear Instruments and Methods in Physics Research Section B: Beam Interactions with Materials and Atoms*, 204(0):570 – 581, 2003. 14th International Conference on Electromagnetic Isotope Separators and Techniques Related to their Applications.

[9] K. Blaum, J. Dilling, and W. Nörtershäuser. Precision atomic physics techniques for nuclear physics with radioactive beams. *Physica Scripta*, 2013(T152):014017, 2013.

[10] H.-J. Kluge and W. Nörtershäuser. Lasers for nuclear physics. *Spectrochimica Acta Part B: Atomic Spectroscopy*, 58(6):1031 – 1045, 2003. LAP-2002 International Conference on Laser Probing.

[11] U. Köster. Intense radioactive-ion beams produced with the ISOL method. In J. Äystö, P. Dendooven, A. Jokinen, and M. Leino, editors, *Exotic Nuclei and Atomic Masses*, pages 437–445. Springer Berlin Heidelberg, 2003.

[12] I. Klaft, S. Borneis, T. Engel, B. Fricke, R. Grieser, G. Huber, T. Kühl, D. Marx, R. Neumann, S. Schröder, P. Seelig, and L. Völker. Precision laser spectroscopy of the ground state hyperfine splitting of hydrogenlike $^{209}Bi^{82+}$. *Phys. Rev. Lett.*, 73:2425–2427, Oct 1994.

[13] L. Weissman, P.A. Lofy, D.A. Davies, D.J. Morrissey, P. Schury, S. Schwarz, T. Sun, and G. Bollen. First extraction tests of the NSCL gas cell. *Nuclear Physics A*, 746(0):655 – 658, 2004. Proceedings of the Sixth International Conference on Radioactive Nuclear Beams (RNB6).

[14] G. Savard, J. Clark, C. Boudreau, F. Buchinger, J.E. Crawford, H. Geissel, J.P. Greene, S. Gulick, A. Heinz, J.K.P. Lee, A. Levand, M. Maier, G. Münzenberg, C. Scheidenberger, D. Seweryniak, K.S. Sharma, G. Sprouse, J. Vaz, J.C. Wang, B.J. Zabransky, and Z. Zhou. Development and operation of gas catchers to thermalize fusion–evaporation and fragmentation products. *Nuclear Instruments and Methods in Physics Research Section B: Beam Interactions with Materials and Atoms*, 204(0):582 – 586, 2003. 14th International Conference on Electromagnetic Isotope Separators and Techniques Related to their Applications.

[15] R. Ringle, G. Bollen, D. Lawton, P. Schury, S. Schwarz, and T. Sun. The LEBIT 9.4 T penning trap system. *The European Physical Journal A - Hadrons and Nuclei*, 25(1):59–60, 2005.

[16] K. Minamisono, P.F. Mantica, A. Klose, S. Vinnikova, A. Schneider, B. Johnson, and B.R. Barquest. Commissioning of the collinear laser spectroscopy system in the BECOLA facility at NSCL. *Nuclear Instruments and Methods in Physics Research Section A: Accelerators, Spectrometers, Detectors and Associated Equipment*, 709(0):85 – 94, 2013.

[17] A. Takamine, M. Wada, Y. Ishida, T. Nakamura, K. Okada, Y. Yamazaki, T. Kambara, Y. Kanai, T. M. Kojima, Y. Nakai, N. Oshima, A. Yoshida, T. Kubo, S. Ohtani, K. Noda, I. Katayama, P. Hostain, V. Varentsov, and H. Wollnik. Space-charge effects in the catcher gas cell of a rf ion guide. *Review of Scientific Instruments*, 76(10):–, 2005.

[18] J.F. Ziegler and J.P. Biersack. The stopping and range of ions in matter. In D.A. Bromley, editor, *Treatise on Heavy-Ion Science*, pages 93–129. Springer US, 1985.

[19] H.G. Dehmelt. Radiofrequency spectroscopy of stored ions I:storage. In D.R. Bates and I. Estermann, editors, *Adv in Atomic & Molecular Physics, Volume 3*, page 53. Academic Press, 1967.

[20] F. Herfurth, J. Dilling, A. Kellerbauer, G. Bollen, S. Henry, H.-J. Kluge, E. Lamour, D. Lunney, R.B. Moore, C. Scheidenberger, S. Schwarz, G. Sikler, and J. Szerypo. A linear radiofrequency ion trap for accumulation, bunching, and emittance improvement of radioactive ion beams. *Nuclear Instruments and Methods in Physics Research Section A: Accelerators, Spectrometers, Detectors and Associated Equipment*, 469(2):254 – 275, 2001.

[21] A. Nieminen, J. Huikari, A. Jokinen, J. Äystö, P. Campbell, and E.C.A. Cochrane. Beam cooler for low-energy radioactive ions. *Nuclear Instruments and Methods in Physics Research Section A: Accelerators, Spectrometers, Detectors and Associated Equipment*, 469(2):244 – 253, 2001.

[22] E. Mané, J. Billowes, K. Blaum, P. Campbell, B. Cheal, P. Delahaye, K.T. Flanagan, D.H. Forest, H. Franberg, C. Geppert, T. Giles, A. Jokinen, M. Kowalska, R. Neugart, G. Neyens, W. Nörtershäuser, I. Podadera, G. Tungate, P. Vingerhoets, and D.T. Yordanov. An ion cooler-buncher for high-sensitivity collinear laser spectroscopy at ISOLDE. *The European Physical Journal A*, 42(3):503–507, 2009.

[23] T. Beyer, K. Blaum, M. Block, Ch.E. Düllmann, K. Eberhardt, M. Eibach, N. Frömmgen, C. Geppert, C. Gorges, J. Grund, M. Hammen, S. Kaufmann, A. Krieger, Sz. Nagy, W. Nörterhäuser, D. Renisch, C. Smorra, and E. Will. An RFQ cooler and buncher for the TRIGA-SPEC experiment. *Applied Physics B*, pages 1–8, 2013.

[24] E. Mané, J.A. Behr, J. Billowes, T. Brunner, M. Brodeur, F. Buchinger, J.E. Crawford, J. Dilling, S. Ettenauer, C.D.P. Levy, A. Voss, and M.R. Pearson. Collinear laser spectroscopy with reverse-extracted bunched beams at TRIUMF. *Hyperfine Interactions*, 199(1-3):357–363, 2011.

[25] B.-M. Sherrill. Scientific Opportunities with the NSCL Coupled Cyclotron Facility. *Progress of Theoretical Physics Supplement*, 146:60–69, 2002.

[26] D.J. Manura and D.A. Dahl. SIMION 8.0. `http://simion.com/`, 2006.

[27] S. Earnshaw. On the nature of the molecular forces which regulate the constitution of the luminiferous ether. *Trans. Camb. Phil. Soc*, 7:97–112, 1842.

[28] G. Bollen. Traps for rare isotopes. In J. Al-Khalili and E. Roeckl, editors, *The Euroschool Lectures on Physics with Exotic Beams, Vol. I*, volume 651 of *Lecture Notes in Physics*, pages 169–210. Springer Berlin Heidelberg, 2004.

[29] J.W. Gibbs. *Elementary Principles in Statistical Mechanics: Developed with Especial Reference to the Rational Foundations of Thermodynamics*. Elementary Principles in Statistical Mechanics: Developed with Especial Reference to the Rational Foundation of Thermodynamics. C. Scribner's sons, 1902.

[30] H. Wiedemann. *Particle Accelerator Physics*. Springer, 2007.

[31] O. Gianfrancesco, F. Duval, G. Ban, R.B. Moore, and D. Lunney. A radiofrequency quadrupole cooler for high-intensity beams. *Nuclear Instruments and Methods in Physics Research Section B: Beam Interactions with Materials and Atoms*, 266(19–20):4483 – 4487, 2008. Proceedings of the XVth International Conference on Electromagnetic Isotope Separators and Techniques Related to their Applications.

[32] T. Sun, S. Schwarz, G. Bollen, D. Lawton, R. Ringle, and P. Schury. Commissioning of the ion beam buncher and cooler for lebit. *The European Physical Journal A - Hadrons and Nuclei*, 25(1):61–62, 2005.

[33] M. Smith, L. Blomeley, P. Delheij, and J. Dilling. First tests of the TITAN digital RFQ beam cooler and buncher. *Hyperfine Interactions*, 173(1-3):171–180, 2006.

[34] I. Podadera Aliseda, T. Fritioff, T. Giles, A. Jokinen, M. Lindroos, and F. Wenander. Design of a second generation RFQ ion cooler and buncher (RFQCB) for ISOLDE. *Nuclear Physics A*, 746(0):647 – 650, 2004. Proceedings of the Sixth International Conference on Radioactive Nuclear Beams (RNB6).

[35] D. Lunney, C. Bachelet, C. Guénaut, S. Henry, and M. Sewtz. COLETTE: A linear paul-trap beam cooler for the on-line mass spectrometer MISTRAL. *Nuclear Instruments and Methods in Physics Research Section A: Accelerators, Spectrometers, Detectors and Associated Equipment*, 598(2):379 – 387, 2009.

[36] G. Sikler, D. Ackermann, F. Attallah, D. Beck, J. Dilling, S.A. Elisseev, H. Geissel, D. Habs, S. Heinz, F. Herfurth, F. Heßberger, S. Hofmann, H.-J. Kluge, C. Kozhuharov, G. Marx, M. Mukherjee, J. Neumayr, W.R. Plaß, W. Quint, S. Rahaman, D. Rodríguez, C. Scheidenberger, M. Tarisien, P. Thirolf, V. Varentsov, C. Weber, and Z. Zhou. First on-line test of SHIPTRAP. *Nuclear Instruments and Methods in Physics Research Section B: Beam Interactions with Materials and Atoms*, 204(0):482 – 486, 2003. 14th International Conference on Electromagnetic Isotope Separators and Techniques Related to their Applications.

[37] G. Ban, G. Darius, D. Durand, P. Delahaye, E. Liénard, F. Mauger, O. Naviliat-Cuncic, and J. Szerypo. First tests of a linear radiofrequency quadrupole for the cooling and bunching of radioactive light ions. *Hyperfine Interactions*, 146-147(1-4):259–263, 2003.

[38] R.B. Moore, O. Gianfrancesco, R. Lumbo, and S. Schwarz. The use of high RFQ fields to manipulate ions. *International Journal of Mass Spectrometry*, 251(2–3):190 – 197, 2006.

[39] R.B. Moore. Buffer gas cooling of ion beams. `http://www.physics.mcgill.ca/~moore/Notes/BeamCooling.pdf`, 2002.

[40] M.D. Lunney and R.B. Moore. Cooling of mass-separated beams using a radiofrequency quadrupole ion guide. *International Journal of Mass Spectrometry*, 190–191(0):153 – 160, 1999.

[41] L.A. Viehland and E.A. Mason. Transport properties of gaseous ions over a wide energy range, {IV}. *Atomic Data and Nuclear Data Tables*, 60(1):37 – 95, 1995.

[42] J.F. O'Hanlon. *A User's Guide to Vacuum Technology*. Wiley, 2005.

[43] F. Paschen. Ueber die zum funkenübergang in luft, wasserstoff und kohlensäure bei verschiedenen drucken erforderliche potentialdifferenz. *Annalen der Physik*, 273(5):69–96, 1889.

[44] J. Sevick. *Transmission Line Transformers*. Classic (Noble Publishing Corporation). Noble, 2001.

[45] S. Falke, E. Tiemann, C. Lisdat, H. Schnatz, and G. Grosche. Transition frequencies of the D lines of ^{39}K, ^{40}K, and ^{41}K measured with a femtosecond laser frequency comb. *Phys. Rev. A*, 74:032503, Sep 2006.

[46] R. Ringle. 3DCylPIC—a 3D particle-in-cell code in cylindrical coordinates for space charge simulations of ion trap and ion transport devices. *International Journal of Mass Spectrometry*, 303(1):42 – 50, 2011.

[47] S. Stroobandt. Single-layer helical round wire coil inductor calculator. `http://hamwaves.com/antennas/inductance.html`, 2009.

[48] P. Schury. Private communication.